UNIVERSITÀ
DEGLI STUDI
FIRENZE

Scuola di
Scienze Matematiche
Fisiche e Naturali

Corso di Laurea in
Scienze Fisiche
e Astrofisiche

Realization of a large-spacing optical lattice for trapping fermionic lithium gases in two dimensions

Realizzazione di un reticolo ottico ad ampio passo per l'intrappolamento di gas fermionici di litio in due dimensioni

Candidata: **Eleonora Lippi**

Relatore: **Dr. Francesco Scazza**

Anno Accademico 2016/2017

Ai miei genitori
e a mio fratello

Contents

Introduction

Low-dimensional fermionic systems are of particular interest since they combine intriguing fundamental aspects with a large technological impact. Their peculiarities arise from the interplay between reduced dimensionality, many-body correlations and quantum statistics. Remarkably, the physics that takes place in the two-dimensional (2D) world is very different from that of three spatial dimensions (3D). The role of thermal phase fluctuations in lower dimensions is enhanced: true long-range order is strictly forbidden at finite temperature. Nevertheless, thermal fluctuations in 2D are not too strong to completely suppress phase coherence, leading to the existence of the Berezinskii-Kosterlitz-Thouless (BKT) phase transition and of quasi-long-range order at sufficiently low temperature. The BKT theory for 2D systems is universal and it describes therefore a wide variety of physical systems falling in the same universality class, ranging from 2D magnets to liquid helium films [1]. Understanding the fundamental properties of 2D systems is of particular relevance for the development of new quantum devices.

A notable class of essentially 2D materials are high-T_c superconductors, which possess a layered crystalline structure in which electrons are essentially confined in 2D. In the celebrated case of cuprate superconductors, that become superconducting at the highest critical temperatures observed so far, electrons move within weakly coupled copper-oxide layers. High-T_c superconductors are very complicated to model theoretically, posing a formidable challenge even for the most advanced computational techniques due to strong correlations between particles: in fact, high-T_c superconductivity still remains an open problem in contemporary physics. Since these systems are formed by many layers stacked and coupled with one another, one intriguing open question in condensed matter regards the role of layering on the genesis of superconductivity. In particular, there are two main aspects requiring investigation: the influence of the reduced layer dimensionality and the effect of inter-layering couplings. Different theories to describe layering effects are currently discussed, the most controversial being the so-called "Interlayer Tunneling Theory" (ITL), proposed by P.W. Anderson [2]. Such a theory proposes that if electrons in the cuprates cannot be described by the standard Fermi liquid theory, the hopping of single particles between the different layers could be strongly inhibited, leaving however the Josephson tunnelling of Cooper pairs unaffected. Anderson's idea is that this feature could lead to an increase of the critical temperature.

Quantum gases are ideal platforms to study strongly correlated systems and simulate layered electron materials, owing to their high degree of isolation from the environment and the well developed toolbox of atomic and optical physics. Layered fermionic superfluids of ultracold atoms can represent an efficient quantum simulator of layered materials where the system parameters including the interlayer tunnel coupling can be fully controlled, together with temperature and interaction strength. A key ingredient for realizing layered atomic superfluids is the development of tailored optical potentials to enable the confinement of atoms in two-dimensional tunable geometries.

In order to confine the atomic motion in the axial direction, i.e. to freeze out

one motional degree of freedom, spatially varying dipole potential are usually employed. The conceptually simplest configuration that provides the required confinement consists of a single strongly elliptic laser beam, i.e. a light sheet, red-detuned with respect to the dominant atomic transition, and shaped as a TEM_{00} Gaussian mode. This scheme suffers however of a lack of flexibility, because confinement in the axial and radial directions cannot be independently controlled. A more versatile set-up consists of a blue-detuned laser beam prepared in a TEM_{01} Hermite-Gauss mode, where the confinement in the radial direction is provided by additional potentials, either created by additional dipole trapping beams or by a magnetic trap. But these schemes allow only the realization of a single two-dimensional atomic system. An alternative approach is to use a standing-wave trap created by the interference of two laser beams, namely a 1D optical lattice, which offers the possibility to load simultaneously several parallel planes of atoms. Depending on the sign of the light detuning, the atoms accumulate in the nodes or in the antinodes of the standing-wave pattern of the optical lattice. In order to adjust the distance between different planes, one can create a standing wave using two beams that cross at an angle smaller than 180 degrees. Such lattice configuration also features an exceptional flexibility, due to the fact that tuning the crossing angle and the intensity of the beams directly allows for tuning the coupling between different atomic planes and permits to choose the number of populated planes from one to several. In this way, one can continuously explore the crossover from a configuration where neighboring layers are strongly coupled by quantum tunneling to the one where layers can be considered as independent systems over the timescales of the experiment.

This thesis work has been carried out in the context of an experiment on quantum gases of ^{6}Li, that aims at investigating the behavior of quantum degenerate fermions in two and three dimensions across the BEC-BCS crossover. Lithium is a prominent species for the study of different fermionic many-body regimes, thanks to the unprecedented controllability of the inter-atomic interactions enabled by a broad Fano-Feshbach resonance. This feature provides the possibility of exploring the transition from a Bose-Einstein condensate (BEC) of tightly bound dimers to a Bardeen-Cooper-Schrieffer (BCS) superfluid of Cooper pairs, also in two dimensions.

The main goal of this thesis is the realization of a suitable optical potential for confining ^{6}Li atoms in single or multilayer 2D geometries. This will allow, in the near future, to study two-dimensional fermionic superfluids, and layering effects in particular. It will be interesting to investigate the role of tunnelling on the superfluid critical temperature, and the superfluid behavior while the system is tuned from a set of several disconnected quasi-2D gases to a regime where the tunnelling restores a three-dimensional geometry via coherent inter-layer Josephson coupling. For this reason, our choice has been to implement a one-dimensional large-spacing optical lattice. The lattice standing-wave pattern is created by crossing two interfering blue-detuned elliptical laser beams at 532 nm under a small angle, using a novel optical scheme that maximizes the passive phase stability of the interference pattern. The atoms will be loaded in one or few intensity minima of the interference pattern, associated with the minima of the optical potential. They will be trapped in-plane by additional magnetic and optical potentials, possibly tailored to produce a flat-bottom two-dimensional trap using a digital micro-mirror device (DMD).

My thesis includes both a computational part, related to the design of the optical lattice potential and to the numerical simulation of the adiabatic loading procedure, and an experimental part, related to the implementation and the characterization of the optical lattice set-up. In more detail, my work has been focused in the following main topics:

- numerical simulation for the optimization of the lattice requirements and design;
- design, development and construction of an optical system for the realization of the large-spacing optical lattice;
- characterization and optimization of the lattice positioning and amplitude stability.

The thesis is organized as follows:

Chapter 1 - I introduce the conditions characterizing a harmonically trapped quasi-2D quantum system, that can be realized in quantum gas experiments. After a brief overview of the thermodynamics quantities at zero and finite temperature for three- and two-dimensional Fermi gases, I explain the procedure of adiabatic compression of the fermionic atomic sample from 3D to a quasi-2D harmonic confinement, with the support of numerical simulations. Subsequently, I shortly discuss how the atomic collisional properties are modified from a 3D to a quasi-2D configuration, and I describe prospects for the exploration of the BEC-BCS crossover in 2D via Fano-Feshbach resonances. Finally, I briefly describe the experimental apparatus for the production of ultracold lithium gases, that will host in the future the setup realized in this thesis work.

Chapter 2 - I introduce the main features of optical dipole potentials, and in particular of optical lattices, with emphasis on the desired properties of the lattice in order to realize a satisfactory quasi-2D confinement. I then describe the experimental optical set-up, focusing on some crucial elements such as lenses and prisms, fundamental to optimize the passive phase stability of the lattice interference pattern. I also give same overview on future upgrades of the imaging system.

Chapter 3 - I discuss the testing of the optical performance of the set-up, presenting the alignment procedure and studying the optical aberrations of the system with a wavefront sensor. I present a static characterization of the produced optical lattice, carried out by imaging both the individual elliptical beams and the interference pattern, allowing the extraction of the lattice spacing and the beam waist to estimate the resulting trapping frequencies.

Chapter 4 - I present the experimental characterization of the dynamical stability of the optical lattice, monitoring the interference pattern on different timescales and performing amplitude and positioning noise measurements. In this framework, I extract the expected noise-induced heating rates for both intensity and fringe position fluctuations.

Chapter 1

Two-dimensional fermionic systems

Systems with reduced dimensionality exhibit very peculiar and rich behavior, consequence of the interplay between statistics, dimensionality and strong interactions. Paradigmatic examples are layered high-T_C superconductors and graphene. Ultracold gases are very suitable to study the physics of lower-dimensional systems thanks to the unprecedented possibility of tailoring two-dimensional geometries made by laser light. But which are the criteria for considering a system two dimensional? In this Chapter, I will discuss the conditions that need to be fulfilled to attain an effectively two-dimensional ultracold Fermi gas trapped in a harmonic potential. I will also discuss how the thermodynamics of the system is affected by changing its dimensionality from 3D to 2D. Moreover, I will present simulations that I have performed to characterize the loading of the gas in a quasi-2D geometry. This will allow to obtain a criterion for realizing quasi-2D gases at finite temperature. Towards the end of this Chapter I present a short overview of the basic scattering theory to show how the reduced dimensionality affects the interactions properties of ultracold atoms. In particular, I will point out the main aspects of the famous BEC-BCS crossover both in the 3D and 2D cases. Finally, I briefly describe the ultracold lithium experiment which is used to produce our Fermi degenerate atomic samples.

1.1 Quantum statistics

One of the striking achievements of cold atom physics is the observation of quantum degeneracy in atomic gases. Indeed, lowering the temperature T of an atomic cloud of density n leads to an increase of the De Broglie wavelength

$$\lambda_{dB} = \sqrt{\frac{2\pi\hbar^2}{mk_BT}} \tag{1.1}$$

of the individual atoms, where m is the atomic mass. When this wavelength becomes comparable to the mean inter-particle spacing $n^{1/3}$, the individual atom wave functions start to overlap. The phase-space density $\rho = n\lambda_{dB}^3$ at this point is on the order of unity, a condition that marks the onset of a quantum degeneracy. Two types of degenerate behavior are possible depending on whether the wave function of the many-particle state is symmetric or antisymmetric under permutation of the particles, i.e. bosonic or fermionic respectively. Furthermore, the behavior of fermionic or bosonic gases at ultra-low temperature is totally different. For a Fermi gas, the atom cloud becomes degenerate at the characteristic temperature T_F and the fermions fill

up all the available states starting from the lowest energy level up to the Fermi energy E_F, as a consequence of the exclusion Pauli principle, for which two identical fermions cannot occupy the same quantum state. On the other hand, in a Bose gas below the critical temperature T_C a macroscopic number of atoms occupy the ground state of the system, producing a macroscopic quantum object called a Bose-Einstein condensate (BEC). The distribution functions describing the two kinds of particle are given by

$$f(\epsilon) = \frac{1}{e^{\frac{\epsilon-\mu}{k_B T}} \pm 1}, \tag{1.2}$$

where k_B is the Boltzmann constant and μ is the chemical potential of the gas, fixed by the atom number N. The sign $+$ leads to the Fermi-Dirac statistics, whereas the sign $-$ leads to the Bose-Einstein one. These distributions give the mean occupation number of a non-interacting system of particles in the quantum state with energy ϵ in the limit $k_B T \gg \Delta\epsilon$ [3], so that the sum over discrete energy states can be written as an integral. The density of states $g(\epsilon)$ for free particles in a d-dimensional box-confinement with energy ϵ is [4]

$$g(\epsilon) = g_s \left(\frac{L}{2\pi}\right)^d \frac{\Omega_d}{2\left(\frac{\hbar^2}{2m}\right)^{d/2}} \tag{1.3}$$

where $g_s = 2s + 1$ is the degree of degeneracy of the levels given by the spin s of the particles, L is the dimension of the box and Ω is the unity of the solid state angle in d-dimensions. Thus, the total number of atoms is given by integration,

$$N = \int_0^\infty f(\epsilon) g(\epsilon) d\epsilon. \tag{1.4}$$

The energy of fermionic atoms, i.e. atoms with an uneven number of neutrons, in the absence of interactions, exhibits an ideal Fermi gas behavior. The Fermi energy, defined as the chemical potential at zero temperature, $E_F = \mu(T = 0)$, can be obtained by fixing the atom number N

$$N = \int_0^\infty g(\epsilon) f(\epsilon) d\epsilon \underset{T=0}{=} \int_0^\infty g(\epsilon) \Theta(\epsilon - E_F) d\epsilon. \tag{1.5}$$

From these, the Fermi temperature $T_F = E_F / k_B$ is given. The fugacity $z = e^{\mu/(k_B T)}$ is generally used to parametrize the degree of quantum degeneracy of the gas: for $T \gg T_F$, $z \simeq 0$ and the Fermi-Dirac distribution approaches the Boltzmann distribution, for $T \ll T_F$, $z \to +\infty$ and $f(\epsilon) = \Theta(\epsilon - E_F)$.

1.2 Fermions in harmonic traps

Experiments with atomic gases are generally performed in an optical potential which can be well approximated by a harmonic potential at ultralow temperatures. We can define our d-dimensional trapping potential as

$$V(x_i, .., x_d) = \frac{1}{2} m \sum_{i=1}^{d} \omega_i^2 x_i^2 \tag{1.6}$$

	2D	3D
g(ϵ)	$\frac{\epsilon}{\hbar^2\omega_r^2}$	$\frac{\epsilon^2}{2\hbar^3\bar{\omega}^3}$
E_F	$(2N)^{1/2}\hbar\omega_r$	$(6N)^{1/3}\hbar\bar{\omega}$
N	$-(\frac{k_BT}{\hbar\omega_r})^2 Li_2(Z)$	$-(\frac{k_BT}{\hbar\bar{\omega}})^3 Li_3(Z)$

TABLE 1.1: Overview of some thermodynamic quantities for harmonically trapped Fermi gases in 2D and 3D.

where m is the atomic mass and ω_i is the trapping frequency. The density of states in a d-dimensional harmonic trap is defined by

$$g(\epsilon) = \frac{\epsilon^{d-1}}{(d-1)!\prod_{i=1}^{d}\hbar\omega_i} \tag{1.7}$$

In the following, I will briefly summarize the principal thermodynamics quantities comparing a 3D gas with a 2D one. The density of states energy ϵ, calculated from (1.7), is respectively equals to

$$g_{3D}(\epsilon) = \frac{\epsilon^2}{2\hbar^3\bar{\omega}^3} \quad \text{and} \quad g_{2D}(\epsilon) = \frac{\epsilon}{\hbar^2\omega_r^2} \tag{1.8}$$

where $\bar{\omega} = (\omega_x\omega_y\omega_z)^{1/3}$ is the geometric mean trap frequency for 3D and $\omega_r = (\omega_y\omega_z)^{1/2}$. The Fermi energy in the harmonic trap is obtained by fixing the atom number N and setting $T = 0$ and the opportune $g(\epsilon)$ in Eq. (1.5) leading to:

$$\text{3D:} \quad E_F = (6N)^{1/3}\hbar\bar{\omega}, \qquad \text{2D:} \quad E_F = \sqrt{2N}\hbar\omega_r. \tag{1.9}$$

For zero temperature, the density distribution is calculated using the local density approximation (LDA), thanks to which the sample can be approximated by a uniform gas for every location $\mathbf{r}$

$$\text{3D:} \quad n_F(\mathbf{r}, T=0) = \frac{4}{3\pi^{1/2}}\left(\frac{m}{2\pi\hbar^2}(E_F - V(\mathbf{r})\right)^{3/2} \tag{1.10}$$

$$\text{2D:} \quad n_F(\mathbf{r}, T=0) = \frac{m}{2\pi\hbar^2}(E_F - V(\mathbf{r})) \tag{1.11}$$

From eq. (1.10) it is possible to extract the Fermi radius $R_{i,F} = \sqrt{2k_BT_F/(m\omega_i^2)}$, i.e. the maximum cloud size given at $V(r_{i,F}) = E_F$ substituting $k_BT_F = E_F$

$$\text{3D: } R_{i,F} = (48N)^{1/6}\sqrt{\frac{\hbar}{m\bar{\omega}}}\frac{\bar{\omega}}{\omega_i}, \qquad \text{2D: } R_{i,F} = (8N)^{1/4}\sqrt{\frac{\hbar}{m\omega_r}}\frac{\omega_r}{\omega_i}. \tag{1.12}$$

In the calculation of the atoms number of a non-interacting Fermi gas at $T > 0$ the impossibility to express explicitly the chemical potential μ might represent a problem. Nevertheless, using the Fermi-Dirac distribution $f(\epsilon)$ and the suitable density

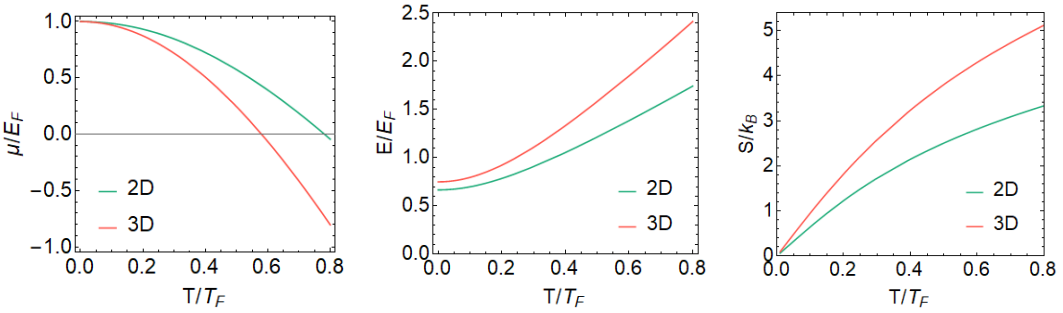

FIGURE 1.1: Thermodynamics quantities of a spin polarized (non-interacting) Fermi gas confined in a 2D or 3D harmonic trap as a function of temperature. On the left, the chemical potential; in the center, the mean energy per particle; on the right, the entropy per particle.

of states, several thermodynamics quantities $X(N,T)$ can be readily obtained analytically by performing integrals of the form:

$$X(N,T) = \int_0^\infty C\epsilon^\eta f(\epsilon)d\epsilon = -C(k_BT)^{1+\eta}\Gamma(1+\eta)Li_{1+\eta}(-z(N,T)) \tag{1.13}$$

where $Li_n(x)$ are the poly-logarithmic functions of order n and $\Gamma(n)$ is the Euler-Gamma function. In order to compute the quantities X, the fugacity $z(N,T)$ can be calculated by inverting the following relation numerically, obtained from Eq. (1.5) at finite temperature:

$$\text{3D:}\quad N = -\frac{k_B^3T^3Li_3(-z)}{\hbar^3\bar{\omega}^3}, \qquad \text{2D:}\quad N = -\frac{k_B^2T^2Li_2(-z)}{\hbar^2\omega_r^2} \tag{1.14}$$

The chemical potential is then:

$$\mu(N,T) = k_BT\log(z(N,T)) \tag{1.15}$$

The total energy E in a 3D harmonic trap can be obtained numerically by

$$\text{3D: } E(N,T) = -\frac{3k_B^4T^4Li_4(-z)}{\hbar^3\bar{\omega}^3}, \quad \text{2D: } E(N,T) = -\frac{2k_B^3T^3Li_3(-z)}{\hbar^2\omega_r^2} \tag{1.16}$$

Using the previous results, the total entropy can be obtained as well [5] [6]:

$$S(N,T) = \frac{E-\mu N}{k_BT} + \int_0^\infty g(\epsilon)\log(1+ze^{-\frac{\epsilon}{k_BT}})d\epsilon. \tag{1.17}$$

Such a quantity can be also computed both for 2D and 3D trap potentials replacing the relative total energy E, the total number of atoms N and density of states. In Fig. 1.1, such thermodynamics quantities are shown, calculated both in the 3D and 2D harmonic potentials.

1.2.1 Quasi-2D confinement

Quasi-two-dimensional (quasi-2D) quantum gases are typically realized by confining the atomic cloud in an optical three-dimensional harmonic potential, in which the confinement along the axial direction is much stronger than the radial one. Due to the high anisotropy of the trap, at sufficiently low temperature, the quantum gas

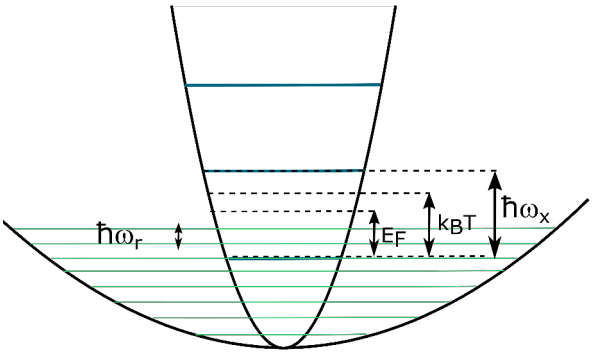

FIGURE 1.2: Sketch of the quasi-two dimensional harmonic confinement. The spacing between energy levels of the harmonic oscillator in the axial direction $\hbar\omega_z$ has to be larger than the Fermi energy and the k_BT of the cloud. The radial harmonic oscillator levels, defined by $\hbar\omega_r$, have to be populated, whereas the only populated state along the axial dimensions has to be the ground state.

can populate the trap levels in two dimensions only, and thermally excited particles cannot move along the third dimension. The general criterion that a fermionic system must satisfy to be considered quasi-2D is given by

$$k_BT, \mu, E_F \ll \hbar\omega_x \tag{1.18}$$

where E_F is the Fermi energy and μ is the chemical potential. This means that the motion of the atoms in the axial direction is frozen out and the atoms occupy only the lowest-energy harmonic oscillator state in the axial direction x with energy $1/2\,\hbar\omega_x$. The different energy scales are sketched in Fig. 1.2.

The maximum number of atoms to fulfill the 2D condition $E_F < \hbar\omega_x$ is estimated for a non-interacting Fermi gas by counting the number of states in a harmonic oscillator with energy lower than that of the first transverse excited state. The energy spectrum of the lowest states that can be occupied is given by setting the number of excitation in the x direction to 0, $n_x = 0$, and it is written as

$$E_{gs\ 2D} = \frac{1}{2}\hbar\omega_x + \hbar\omega_y\left(n_y + \frac{1}{2}\right) + \hbar\omega_z\left(n_z + \frac{1}{2}\right). \tag{1.19}$$

This energy level has to be always smaller than that of the first excited state in the x direction, which is given by setting $n_x = 1$ and $n_y, n_z = 0$

$$E_{fe\ 2D} = \frac{3}{2}\hbar\omega_x + \frac{1}{2}\hbar\omega_y + \frac{1}{2}\hbar\omega_z. \tag{1.20}$$

Imposing $E_{fe\ 2D} > E_{gs\ 2D}$, we can then relate the frequencies to one another:

$$\omega_x > n_y\omega_y + n_z\omega_z. \tag{1.21}$$

Introducing the trap aspect ratio $\lambda = \omega_x/\omega_r$ in the limit in which $\omega_y = \omega_z \equiv \omega_r$ with $n_r = n_y + n_z$, on the basis of Eq. (1.21) and including degeneracy, it is possible

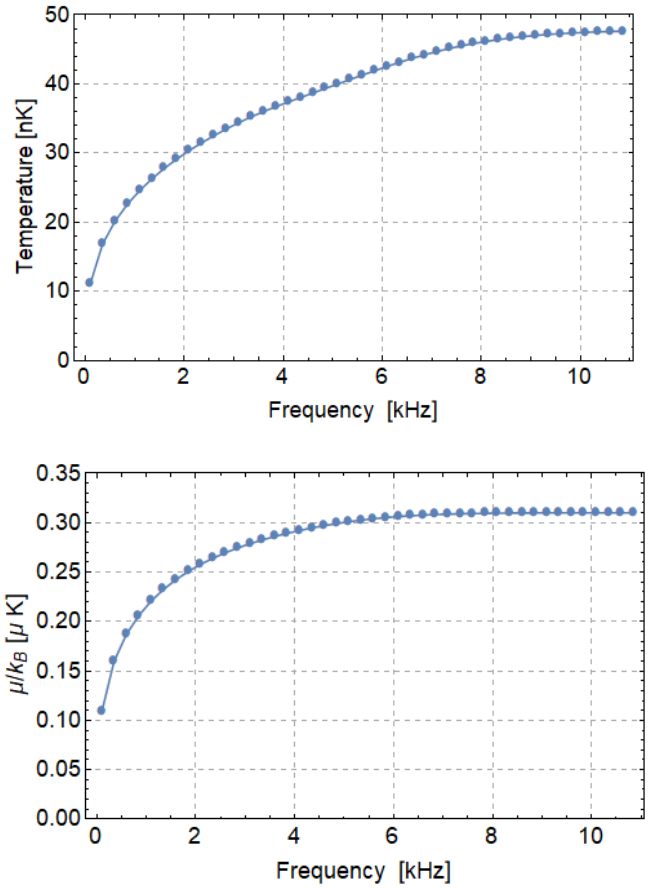

FIGURE 1.3: Temperature (on the left) and chemical potential (on the right) after an adiabatic compression of a cloud of $N = 2.5 \cdot 10^4$ ^6Li atoms at an initial T/T_F=0.1, for different final vertical frequencies of confinement. The loading is from a dipole 3D harmonic trap with frequencies 21 Hz, 245 Hz, 215 Hz, to an highly anisotropic 2D one with in-plane frequencies of 20 Hz and 20 Hz.

to count the critical number of atoms by [7]

$$N_{crit,2D} = \sum_{n_r=0}^{\lambda-1} (n_r + 1) = \frac{\lambda^2 + \lambda}{2}. \tag{1.22}$$

This result shows that the dimensionality of the trap does not depend on the absolute values of the trapping frequencies but only on their ratio. For example, providing an aspect ratio of 1:1:500 with trap frequencies of e.g. $\omega_x = 2\pi \cdot 10$ kHz and $\omega_r = 2\pi \cdot$ 20 Hz, the maximum number that we can load into our optical potential to fulfill the 2D condition is about $N_{crit,2D} \cong 10^5$ per spin state.

1.2.2 Adiabatic compression from 3D to quasi-2D

Cold atoms are typically produced in 3D harmonic traps. In the procedure of compression of the atomic sample from the 3D dipole trap to a quasi 2D-confinement, and assuming the process adiabatic, it is possible to give an upper limit value for the temperature and the chemical potential of the sample at its final stage.

I performed some numerical simulations to characterize the loading of the gas in a quasi-2D geometry. This will allow to obtain a criterion for realizing quasi-2D gases at finite temperature. We consider a gas of fermions of mass $m = m_{Li}$

confined in a quasi-2D harmonic potential as defined previously. We set $g_{2D}(\epsilon) = \epsilon/(\hbar\omega_r)^2$ for the in-plane density of state and $\mu_j = \mu_0 - \hbar\omega_x j$ for the chemical potential, where j is the integer labeling the jth state of the axial harmonic oscillator. The average occupation number for jth state is given by the Fermi-distribution $f_j(\epsilon) = 1/(e^{\beta(\epsilon-\mu_j)}+1)$ with $\beta = 1/(k_B T)$. Using the poly-logarithm function Li_n, we can compute N_j, E_j and S_j which are respectively the atom number, the total energy and the entropy in jth state. We want to estimate the temperature of the 2D gases trapped in potentials with different axial frequency. To do this, we compute the temperature evolution for an adiabatic compression by evaluating, for each value of a final compression frequency ω_x, the temperature and the chemical potential of the cloud assuming the conservation of total entropy and of the number of atoms during the transfer. The sum of the entropies and atom number on each level of the harmonic oscillator in the axial confinement is fitted to give the total energy S_0 and atom number N_0 in the dipole trap with the chemical potential μ_0 and the temperature T as free parameters:

$$\begin{cases} S_0 = \sum_j S_j^{2D}(\mu_j, T) \\ N_0 = \sum_j N_j^{2D}(\mu_j, T). \end{cases} \tag{1.23}$$

By inserting parameters easily achievable in the laboratory, i.e. number of atoms $N = 2.5 \cdot 10^4$ and T/T$_F$=0.1, the adiabatic transfer from a dipole trap with trapping frequency of $\omega_z \sim 2\pi\cdot$20 Hz, $\omega_x = \omega_y \sim 2\pi\cdot$200 Hz, is shown in Fig. 1.3, for different values of the frequency ω_x in the quasi 2D-potential. Such a values of temperature and chemical potential, allow to calculate the numbers of atoms in each level of the harmonic oscillator Fig. 1.4. The 2D condition is reached for the critical frequency ω_C at which the population for j=1 approaches to zero. This criteria is more general than that in Eq. (1.22), because it is defined also for finite temperatures.

From Fig. 1.4 is clear that the 2D condition is reached for frequencies above 8 kHz. Furthermore, looking to the temperature trend above 8 kHz in Fig. 1.3, we can notice that a compression of the gas above these frequency values produce an heating of the cloud, evidenced by the fact that starting from 20 nK, the final temperature is about 40% higher.

Eventually, we are interested to know which is the number of atoms that can be loaded for a certain critical frequency ω_C, or viceversa. This is shown in Fig. 1.4. We observe that at a fixed trap frequency, the number of atoms adiabatically loaded, depends drastically on the temperature of the sample. For example, just going from $T/T_F = 0.1$ to $T/T_F = 0.2$, the critical atom number is halved. Reasonably, the upper limit for the critical number of atom loaded in the trap is given by the zero temperature limit (blue curves), that is calculated by Eq. (1.22).

1.3 Ultracold interactions

In the previous Section, I have discussed the conditions to realize the 2D regime. Looking now at the interactions between fermions, the reduced dimensionality affects the scattering properties of the system and the interactions differ from those in a three dimensional system.

Scattering in three-dimensions The length scale on which interactions between neutral atoms take place is given by the short-ranged van der Waals potential, which scales as r^{-6} and has a finite range known as the van der Waals radius r_{vdW}. Taking

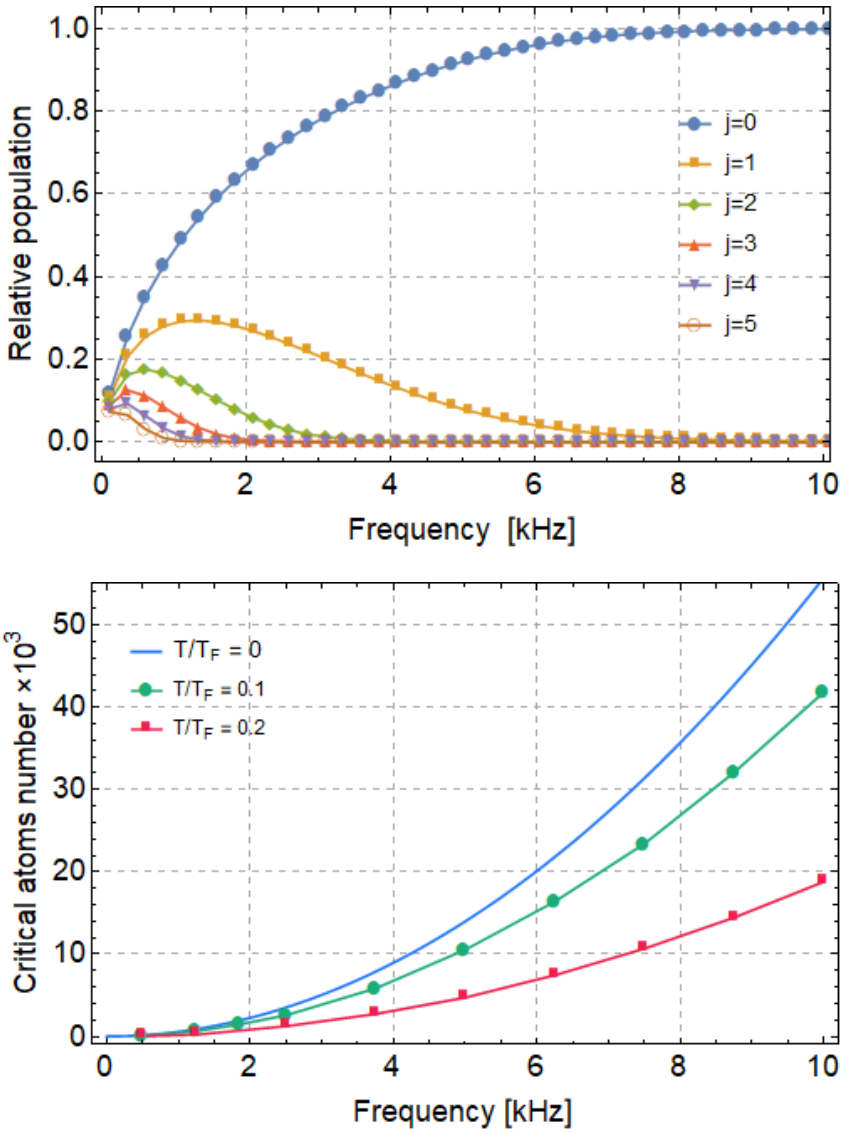

FIGURE 1.4: (Top) The population of non-interacting fermions at T/T_F=0.1 in the j-th state of the harmonic oscillator is computed for different trapping frequency along the direction of tight confinement. The 2D condition is reached for $\omega > \omega_C$, where the population for $j = 1$ approaches zero. (Bottom) The maximum number of atoms N_0 is calculated for a given critical trap frequency ω_C. In these plots, the adiabatic compression of a cloud has been computed for $N = 2.5 \cdot 10^4$ ^6Li atoms for initial T/T_F=0.1 (green) and T/T_F=0.2 (red). These are compared with the $T = 0$ criterion (blue). All curves are calculated considering an adiabatic transfer from a dipole trap with frequencies (21 Hz, 245 Hz, 215 Hz) to a highly anisotropic 2D trap with in-plane frequencies of 20 Hz and 20 Hz.

into account that the temperature at which quantum degeneracy is achieved is between 100 nK $\div$ 50 μK, λ_{dB} is about 1 μm. The range of interaction is given by the van der Waals radius $r_{vdW,Li} = 0.2$ nm and thus satisfy the inequality $\lambda_{dB}, n^{1/3} \ll r_{vdW}$ meaning that particles interact via two-body collisions. We consider a 3D quantum gas characterized by a two-body interacting potential $V(\mathbf{r})$ that is radially symmetric short range and decreases as $1/r^i$, $i > 1$. In the long distance term, the wave function, $\psi(\mathbf{r})$, that satisfies the Schrödinger equation

$$\left[-\frac{\hbar^2}{2m}\nabla^2 + V(\mathbf{r})\right]\psi(\mathbf{r}) = E\psi(\mathbf{r}), \tag{1.24}$$

where $\mathbf{r}$ is the relative coordinate and m is the reduced mass of the particle, can be written as a sum of an incoming plane-waves plus an outgoing spherical wave with a k momentum along the axis of its initial motion

$$\psi_k(\mathbf{r}) \propto e^{ikz} + f(k,\theta)\frac{e^{ikr}}{r}. \tag{1.25}$$

The scattering amplitude $f(k,\theta)$ doesn't depend by ϕ for symmetry reasons. Since the relative distance between two particles $|r|$, given by $n^{1/3}$, is larger than r_{vdW}, the long range limit reflects the condition in ultracold gases quite well. All the relevant information are contained in the scattering amplitude which can be calculated expanding the wave-function $\psi(\mathbf{r})$ into the spherical-waves basis with angular momentum l. This expansion, inserted in the Schrödinger equation, leads to a radial equation that depends on l and that can be related to the centrifugal barrier inhibiting the scattering for $l > 0$ in the regime of small scattering energies. The centrifugal barrier for ^{6}Li is on the order of 7 mK and thus collisions for lower temperature could only occur due to isotropic s-wave scattering. The only effect of an elastic collision is a phase shift of δ_l for each spherical wave. In the ultracold regime the particles become indistinguishable and to determine the scattering amplitude we need to take into account that we cannot distinguish between two scattering properties, whose the only difference is the permutation of the particles position. Thus, the differential cross-section is given by

$$\frac{d\sigma_{indist}}{d\Omega} = |f(k,\theta) \pm f(k,\pi-\theta)|^2, \tag{1.26}$$

and the total cross-section is obtained by integrating it over the full solid angle

$$\sigma_{tot}(k) = \frac{4\pi}{k^2}\sum_{l=0}^{\infty}(2l+1)[1 \pm (-1)^l]\sin^2(\delta_l(k)). \tag{1.27}$$

The total cross-section is different from zero only for odd l, whereas it is even for fermions. A Fermi gas interacting via s-wave scattering can hence only be realized with at least two different kinds of fermions which are then distinguishable and can interact, otherwise $\sigma(k) = 0$. For distinguishable particles at $l = 0$ and $k \to 0$, $\sigma(k) = 4\pi a^2$. The universal parameter for scattering at low temperature is

$$a = -\lim_{k\to 0}\frac{\tan\delta_0(k)}{k}. \tag{1.28}$$

At ultra-low temperatures, the thermal wavelength of De Broglie, associated

with the relative momentum k, by far exceeds the van der Waals range of the interatomic potential. As such, similarly to a light wave imprinting on a scatterer much smaller than its wavelength, the resulting collision process is predominantly isotropic, i.e. s-wave. As a consequence, owing the anti-symmetry against particle permutation of the scattering wave function set by the Pauli principal for two identical fermions, ultracold collision are suppressed in spin-polarized fermionic samples. Moreover in the ultracold regime the scattering properties are fully encoded in the s-wave scattering amplitude, which in turn can be expanded as

$$f(k) = -\frac{1}{ik + \frac{1}{a} - R^* k^2} \tag{1.29}$$

The ultracold collisions are therefore characterized by two only parameters which are the scattering length a and the the effective range potential $R*$. While a sensitively depends on the presence of weakly bound (or virtual) molecular states near the energy threshold of the colliding atoms, R* is essentially set by high-energy, microscopic properties of van der Waals interatomic potential [8]. In particular, when the molecular state lays above the scattering threshold, a is negative, corresponding to a net atom-atom attraction. On the other hand, the net interaction is repulsive if the molecular state lays below the scattering threshold an thus a is positive.

The scattering processes are universal and can be described as a contact interaction [9] with a pseudo-potential

$$V(\mathbf{r}) = g\delta(\mathbf{r}) \tag{1.30}$$

where $\delta\mathbf{r}$ is the delta function and $g = 4\pi\hbar^2 a/m$ is the so-called interaction strength. The mean interaction energy in a sample with homogeneous density $n = N/V$ is given by

$$E_{int}(a) = gn = \frac{4\pi\hbar^2 n}{m} a \tag{1.31}$$

where the sign of the scattering length a leads to a different kind of the mean-field interaction, i.e. attractive if a is positive, repulsive if a is negative.

Scattering in two-dimensions The reduced dimensionality affects the scattering properties of the system and the interactions differ from those in a three dimensional system. Due to the changed dimensionality, the scattering between two identical particles is described by [10]

$$\psi_k(\mathbf{r}) \propto e^{i\mathbf{kr}} - \sqrt{\frac{i}{8\pi}} f(k) \frac{e^{ikr}}{\sqrt{kr}} \tag{1.32}$$

and for a pure 2D system at low energy one thus obtain for the scattering amplitude

$$f(k) = \frac{4\pi}{2\ln\frac{1}{ka_{2D}} + i\pi} \tag{1.33}$$

where a_{2D} is the 2D scattering length. This formula shows that the 2D scattering amplitude, in contrast with the 3D one, exhibits always a logarithmic dependence.

Collisional properties in quasi-two dimensions Nevertheless, in the quasi 2D-regime the range of interaction, characterized by $r_{vdW,Li} \sim 0.2$ nm, is much smaller

than the length scale of the axial confinement given by $l_x = \sqrt{\hbar/m\omega_x}$ and on about 410 nm for unbound atoms and 290 nm for molecules, for an axial frequency of about 10 kHz. Being the range of interaction $r_{vdW,Li} \ll l_x$, the relative motion of the particle is not influenced by the axial confinement and the scattering process can be derived 3D scattering amplitude. The scattering amplitude of this so-called quasi-2D system has been calculated in and in the low energy limit $E \ll \hbar\omega_x$ is given by

$$f(k) = \frac{4\pi}{\sqrt{2\pi}\frac{l_x}{a} + \ln(\frac{\alpha}{\pi(kl_x)^2}) + i\pi} \tag{1.34}$$

with $\alpha \approx 0.915$. From this formula we observe that the maximum scattering amplitude depends on the energy of the system k and on the ratio between l_x and a, in spite of the divergence of a in the 3D case. In this regime, i.e. when the scattering energy is negligible as compared to the strength of the tight confinement, the 3D scattering length can be defined in terms of the approximated binding energy

$$a_{2D} = l_x\sqrt{\frac{\pi}{A}}e^{-\sqrt{\frac{\pi}{2}}\frac{l_x}{a}} \tag{1.35}$$

where $A \approx 0.905$ In analogy to the 3D case, the 2D interaction strength is then [11]

$$g_{2D} = \frac{\sqrt{8\pi}\hbar^2(a/l_x)}{m} = \frac{\hbar^2}{m}\tilde{g}_{2D} \tag{1.36}$$

with the dimensionless 2D coupling constant $\tilde{g}_{2D} = \sqrt{8\pi}(a/l_x)$.

1.4 Feshbach resonances

Tuning the scattering length allow to resonantly control of the scattering properties of atoms pair. This is precisely what happens at a magnetic Feshbach resonance, where the open scattering channel is brought via the Zeeman effect to energy degeneracy with a bound molecular state supported by another closed channel with a different magnetic moment. Since the two interaction potentials depend on the hyperfine states of our interacting participating particles, their magnetic momenta differ and, thus, the difference in their continuum energy is given by $\Delta E = \mu\Delta B$. Close to the resonance center B_0 the scattering length deviates from its background value a_{bg}, exhibiting a sharp dependence on the external magnetic field B given by

$$a(B) = a_{bg}\left(1 - \frac{\Delta}{B - B_0}\right) \tag{1.37}$$

where Δ is the resonance width. In particular, the value and the sign of $a(B)$ directly determine both the scattering cross-section of the atom pair and the strength of the inter-particle interaction, i.e. attractive if $a(B) > 0$, repulsive otherwise.

Feshbach resonances are a gift of nature offered to the experimentalist in the field of the ultracold atoms, because through the simple application of an external magnetic field on can make the strength of two-body interaction either attractive or repulsive, arbitrarily large or small. Changing the interactions has allowed to explore different regime of interactions between fermions, and brought to the first observation of a "fermionic condensate". Even if the fermions, also at low temperature, have not coherent wave-functions due to the Pauli exclusion-principle, pairing between fermions in different regime of interactions can lead to forms of matter, that

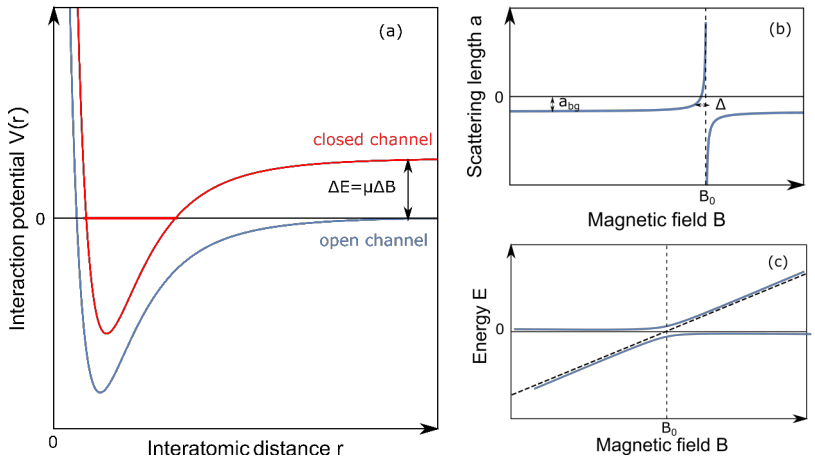

FIGURE 1.5: Two-channel model of a Feshbach resonance. (a) Interaction potential as a function of the interatomic distance between two particles. (b) Scattering length as a function of the magnetic field B. (c) Energy of a bound molecular state as a function of the magnetic field B.

"is not a BEC neither a superconductor but something that may link between this two behaviors[1]".

1.5 BEC-BCS crossover

The BEC-BCS crossover, which connects bosonic and fermionic superfluidity, in three dimensions, has been subject to intense studies. In contrast, its 2D counterpart is not well understood yet. The experiments that will be performed in our apparatus after the quasi 2D-confinement regime will be achieved, should contribute to understanding these many-body phenomena. In this Section I will discuss BEC-BCS crossover in 3D, giving an very brief overview on the changing expected in 2D.

Three-dimensions In these regime is possible to achieve the so-called fermionic superfluidity. The strength of interaction is quantified by the dimensionless interaction parameter $1/k_F a$ which relate the inter-particle spacing $\sim 1/k_F$ to the scattering length a. By tuning the scattering length we are able to access three different regimes as shown in Fig. 1.6.

BEC regime For $1/(k_F a) \to +\infty$ we reach the so-called BEC regime in which there formation of molecules. Tuning the interaction close to the Feshbach resonance on the repulsive side with $a > 0$ leads to the formation of weakly bound molecules by three-body recombination where the excess momentum is carried away by a third particle. To this molecular bound state, if $a >> R^*$ is possible to associate an universal binding energy

$$E_B = \frac{\hbar^2}{ma^2}. \tag{1.38}$$

When the temperature of the gas is smaller than E_B, two fermions with different spin can occupy this bound state and create a composite bosonic molecule. The trap depth is increased by a factor two for molecules because two times

[1] Debbie Jin

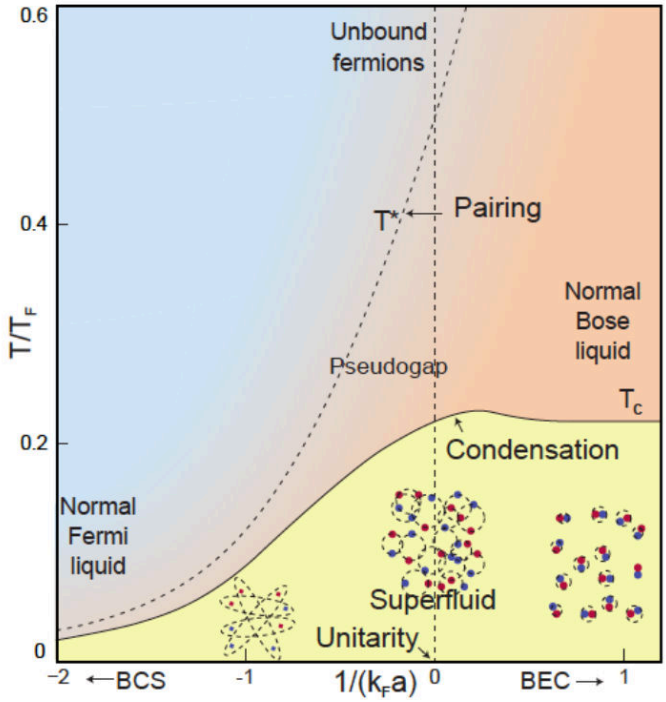

FIGURE 1.6: Phase diagram of the crossover region. The pair creation temperature T^* is given by the dashed line, whereas the superfluid transition temperature T_C is given by the solid line. The picture is taken from [12].

larger polarizability which suppresses the loss of molecules in contrast of the loss of atoms.

BCS regime : For $1/(k_F a) \to -\infty$ we reach the weakly attractive interaction regime known as BCS-regime, where correlation in momentum space takes place and the so-called Cooper pairs can be formed. Since in the BEC limit pairing is only a two body phenomenon, Cooper pairs are called many-body pairs because the filled Fermi sea up to the Fermi surfaces necessary to the formation process and the pairing is generated by the collective interaction around the Fermi surface.The ground state of a balanced attractive, non interacting two-component Fermi gas at zero temperature with energy $E_0 = N(3/5)E_F$ is unstable against attractive interactions and that pairing momentum space reduces the energy of the system following [13]

$$E_{BCS} = E_0 - \frac{1}{2}\rho(E_F)\Delta_{GAP}^2 \tag{1.39}$$

where E_{BCS} describes the energy of the attractively interacting BCS state, $\rho(E_F)$ corresponds to the density of the states at the Fermi level and Δ_{GAP} is related to an energy gap in the excitation spectrum at the Fermi surface. The minimization of the energy of the system is thus given by the formation of the so-called Cooper pairs [14], which consist of two particle of opposite momentum and spin. The zero temperature paring gap depends exponentially on the absolute value of the scattering length a [15]

$$\Delta_{GAP} \sim \left(\frac{2}{e}\right)^{7/3} E_F e^{-\frac{\pi}{2k_F|a|}} \tag{1.40}$$

and it is related to break a pair. The temperature T_C for which the Cooper pair become superfluid in a finite temperature system is given by $k_B T_C = \frac{e^\gamma}{\pi}\Delta_{GAP}$, where $e^\gamma = 1.78$ [15]. In the limit of weakly attractive interaction, this temperature coincide with with the critical temperature to create Cooper pairs T^*. the transition temperature T_C is very low compared to the transition temperature at the BEC side making the transition from a weakly interacting Fermi gas to the superfluid phase rather hard to realized.

Unitary regime : The precedent two limiting cases are continuously connected by the Unitary regime characterized by $1/(k_F a) \to 0$. When the range of interaction between particle diverges, the character of the interaction is no more relevant, because the scattering amplitude does not depend on the scattering length a anymore.This regime is generally called universal. All the thermodynamic properties of the system can be described on the natural energy scale E_F and for this reason the physical properties of this kind of strongly interacting degenerate gas can be found in different systems ranging from atomic nuclei to neutron star. The parameter that discriminates between these systems is their density, which goes from approximately 10^{12} atoms/cm^3 in ultracold atomic samples until 10^{38} atoms/cm^3 in neutron stars. Despite the divergence of the scattering length the crossover from one side to another is smooth and the adiabatic switches of the magnetic field value may allow to explore the different regimes during the same experimental cycle.

Two-dimensions As discussed above, the reduced dimensionality affects the scattering properties of the system leading, for a 2D Fermi gas, to the existence of a confinement induced two-body bound state $E_{B,2D}$ for every magnetic field, which can be related to a 2D scattering length a 2D by the equation

$$E_{B,2D} = \frac{\hbar^2}{m a_{2D}^2}. \tag{1.41}$$

This quantity depends on the trap geometry and it is connected to the 3D scattering length a via the transcendental equation [11]

$$\frac{l_x}{a} = \int_0^\infty \frac{du}{\sqrt{4\pi u^3}}\left(1 - \frac{exp(-E_{B,2D}u/\hbar\omega_x)}{\sqrt{\frac{1}{2u}(1-exp(-2u))}}\right). \tag{1.42}$$

For weak attractive interaction and $|a| < l_x$, the molecular binding energy can be well approximated by [11]

$$E_{B,2D} = 0.905(\hbar\omega_x/\pi)exp(-\sqrt{2\pi}l_x/|a|). \tag{1.43}$$

Close to the 3D Feshbach resonance for diverging a, this equation no longer holds and it can be replaced by the universal constant $E_B(a=\infty) = 0.244\hbar\omega_x$. For a repulsive three dimensional scattering length $a > 0$ the two dimensional molecular state $E_{B,2D}$ approaches the three dimensional one E_B. Then the size of the molecule given by $a_{2D} = /\sqrt{mE_B}$ becomes smaller than the characteristic length of the confinement l_x and so the binding energy is not longer affected by the confinement. In 2D, the BEC and BCS limit are reached for $\ln(k_F a_{2D}) > -1$ and $\ln(k_F a2D)$ respectively. Similar to the 3D case, a 2D Fermi gas on the BEC side of the crossover consists of deeply bound bosonic molecules. However, there is no Bose- Einstein condensation but a

BKT transition into a superfluid state for T$>$ 0 in the homogeneous case, similar as in the 2D Bose gas. Although for $\ln(k_F a_{2D}) > 0$, the two-body bound state still exists, it is only loosely bound, and can be broken up when μ and $k_B T$ become on the order of its binding energy. Thus, the system becomes fermionic for sufficiently large $\ln(k_F a_{2D})$, in analogy to the 3D case. In the fermionic limit with weak attractive interaction, the system can be described by loosely bound Cooper pairs in the framework of BCS theory as in the 3D case. Similar to the 3D case, Cooper pairing occurs for sufficiently low temperatures.

1.6 Our experiment

This master thesis project has been carried out in the context of an ultracold atom experiment, aiming to study the behavior of quantum degenerate fermionic atoms in two and three dimensions across the BCS-BEC crossover. In this last Section, I will give a very brief overview of the experimental procedure for producing the cold fermionic gases. The atomic samples used for this study is chosen as ^{6}Li that is the only stable fermionic isotope of the alkali metals apart from ^{40}K. Lithium is one of the simpler atoms of the periodic table. First, as an alkali, it has only one valance electron and thus exhibits a simple, hydrogen-like electronic spectrum, making it suitable for laser cooling. Second, it is by far the lightest element and it is relevant in the realization of optical lattices because light atoms can tunnel very efficiently (see Subsection 2.3.2) since the recoil energy in a lattices scales as $E_R \propto 1/md^2$ where d is the lattice constant. Another advantage that has made ^{6}Li so widely used in ultracold atoms experiments is its extremely broad Feshbach resonances among the two lowest hyperfine levels at 832 Gauss that allow a unique control of the interaction between particles, permitting to explore extensively the physics at the BEC-BCS crossover and to realize toy-models of condensed matter systems.

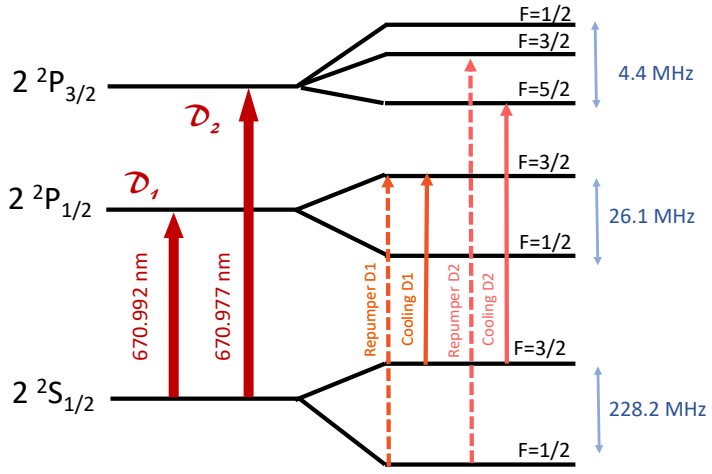

FIGURE 1.7: Hyperfine structure of ^6Li at zero magnetic field and scheme of the D1 and D2 transitions. In orange the transitions used for the grey molasses cooling [16].

In order to implement laser cooling and trapping for the realization of a quantum degenerate atomic samples, the optical spectrum of lithium (see Fig. **??**) offers a prominent spectroscopic feature called D-line that corresponds to the transition between the ground state 2S and the excited state 2P. For ^6Li the total electronic spin is $\mathbf{S} = \frac{1}{2}$ and the nuclear angular moment is $\mathbf{I} = 1$ and this leads to total angular

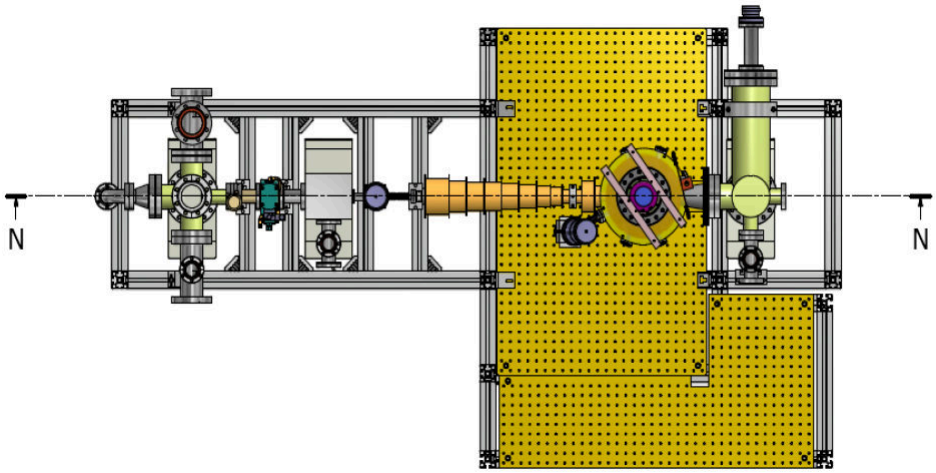

FIGURE 1.8: View of the overall UHV apparatus where ultracold lithium gases are produced. Atoms are initially held in the oven and then enter though a nozzle in the main UHV system. Deceleration by Zeeman slower allows atoms to be captured inside the science chamber, where magneto-optical trapping and evaporative cooling in a crossed optical dipole trap are performed.

momentum of the atoms $\mathbf{F} = \mathbf{S} + \mathbf{L} + \mathbf{I}$ to just have integer values, justifying the fermionic character of the isotope. The two fine structure lines D1 and D2, where the splitting is given by the spin-orbit interaction $\propto \mathbf{L} \cdot \mathbf{S}$. Considering also the coupling with the nuclear spin $\propto \mathbf{J} \cdot \mathbf{I}$, where $\mathbf{J} = \mathbf{L} + \mathbf{S}$ one find the hyperfine structure. During the experiment we introduce the Feshbach magnetic field, therefore we have to consider the Zeeman shift of the energy levels due to the interaction between this field and the total spin of the atoms. The typical used magnetic field $B \geq 500$ Gauss is high enough to completely decouple $\mathbf{I}$ and $\mathbf{J}$ inducing a shift with respect to the hyperfine line of $\Delta E \simeq \mu_B g_J m_J B/\hbar$, where g_J is the Landè factor and m_J is magnetic quantum number associated to the total electronic momentum.

The experimental sequence to produce a degenerate gas of ^{6}Li is the following. A sample of ^{6}Li is heated in an oven to about 400° to generate a collimated beam of atoms. The hot atoms are then slowed by a counter-propagating laser beam in a Zeeman slower while propagating to the science chamber where they are captured by a magneto-optical trap (MOT). In the MOT they are cooled down operating on the D2 optical transitions $2S_{1/2} \rightarrow 2P_{3/2}$. The advantage respect the D1 line is that D2 transition has a lower saturation intensity, i.e. 2.56 mW/cm^2 respect to those of D1 transition , requiring quite low laser power. Moreover, from a theoretical point of view, the only closed transition in this system is the $F = 3/2 \rightarrow F' = 5/2$ that is contained in the hyperfine structure of the D2 line. We typically collect about 10^9 atoms at about 500 μK. The temperature in this phase is limited by the absence of efficient sub-Doppler cooling due the unresolved hyperfine splitting of the excited states. In our experiment it been developed an efficient sub-Doppler scheme based on gray molasses which exploits D1 transitions $2S_{1/2} \rightarrow 2P_{1/2}$ as described in details in [16]. This mechanism relies the presence of dark states which are populated by choosing the opportune relative ratio and relative frequency between cooling and repumper lights. In this way we can cool the lithium sample to about 40 μK in about 10 ms. The fraction of cooled atoms is about 75% of the initial number. These are the ideal conditions to transfer the atoms in a conservative potential, i.e. an optical dipole trap (ODT), where we perform the evaporative cooling to quantum degenerate regimes. A detailed description of the fundamental parts of the apparatus (see

Fig. 1.8), can be found in the master thesis [17] [18] [19] and in the PhD thesis [20].

All cooling stages from the magneto-optical trap (MOT) to the evaporative cooling, and all of the physical experiments are performed in the same science chamber. It is a custom octagonal stainless-steal cell from Kimball Physics and its several windows allow a large optical access among several directions to perform high-resolution imaging of the atomic cloud and to imprint many optical potentials. On the vertical axis it is equipped with two large re-entrant view-ports with silica windows, made by Ukaea, with a 60 mm diameter and a thickness of 6 mm with a relative distance in vacuum of 25.4 mm. The diameter of the circumference inscribed into the octagon is of 177.3 mm and then the distance between the center of the chamber, i.e. the position of the atoms, and the window is about 9 cm; at this dimension has to be added the weight of the window that is about 1 cm. The size of the window in the horizontal plane is about 6 cm for the diameter.

Chapter 2

An optical lattice for quasi-2D confinement of lithium atoms

Laser light is a powerful tool that can be used to change the internal state of an atom but also to manipulate its external degrees of freedom, i.e. its velocity and its position. Radiative forces, associated with the absorptive and the dispersive properties of the interaction between light and atoms, permit cooling and trapping, respectively. Optical potentials are based on the conservative and almost purely dispersive interaction between atoms and light detuned from the frequency of the atomic transitions. They became a fundamental ingredient in the field of ultracold gases as they allow to confine atoms in tailored and tunable geometries. This tunability can be exploited to simulate a great variety of physical systems, ranging from homogeneous 3D, low dimensional systems and double or multi-well configurations, enabling single-atom addressability and arbitrary imprinting of potentials. In particular, optical lattices created by interference between laser beams are used to form potentials for atoms in which the atoms motion can be frozen along one, two or all the dimensions, adding up multiple tightly confining potentials. In this Chapter, after first introducing the essential properties of optical dipole potentials (see Section 2.1) and optical lattices (see Section 2.2), I will discuss the requirements for the quasi-2D confinement of lithium atoms. I will then present the optical lattice scheme that was designed in the context of this thesis (see Section 2.4) and I will outline its experimental implementation (see Section 2.5).

2.1 Optical dipole trapping

Optical dipole trapping of atoms relies on the dipole interaction between the spatially inhomogeneous electric field of the laser radiation, far-detuned from the relevant atomic transitions, and the induced atomic dipole moment. Optical potentials offer very small heating rates, a great choice of trap geometries and the possibility for trapping atoms independent of their specific substate. On the other hand, the dipole force is the weakest mechanism to confine atoms and it leads to trap depths that are typically below 1 mK, therefore much smaller than those based on radiation pressure or magnetic-dipole interaction. For this reason, atoms loaded in optical dipole traps need to be pre-cooled since the temperature has to be lower than the trap depth to avoid losses. Such traps, considered for the first time in the '60s in connection with plasmas as well as neutral atoms, are nowadays employed not only in ultracold atomic physics but are also used routinely in biophysics, where they are known as optical tweezers.

To discuss which are the principal features to take into account for realizing a dipole trap with laser beams, I am going to follow the review article by Grimm *et*

al. [21]. Qualitatively, when an atom, considered as a simple oscillator, is placed in an electromagnetic field, like that of a laser beam, the electric field $\mathbf{E}(\mathbf{r},t) = \hat{\mathbf{e}}\,\mathbf{E}(\mathbf{r})\exp(-i\omega t) + c.c.$ induces an atomic dipole moment $\mathbf{p}(\mathbf{r},t) = \alpha(\omega)\mathbf{E}(\mathbf{r},t)$ which starts to oscillate at the field frequency ω with a complex frequency-dependent polarizability $\alpha(\omega)$. The two main quantities of interest for dipole traps are the time-averaged interaction energy of the induced dipole with the generating electric field, and the photon scattering rate

$$U_{dip}(\mathbf{r}) = -\frac{1}{2}\langle \mathbf{p}(\mathbf{r},t)\mathbf{E}(\mathbf{r},t)\rangle = -\frac{1}{2\epsilon_0 c}\Re e\{\alpha(\omega)\}I(\mathbf{r}) \tag{2.1}$$

$$\Gamma_{sc}(\mathbf{r}) = \frac{P_{abs}}{\hbar\omega} = \frac{1}{\hbar\epsilon_0 c}\Im m\{\alpha(\omega)\}I(\mathbf{r}), \tag{2.2}$$

where $P_{abs} = \langle \dot{\mathbf{p}}(\mathbf{r},t)\mathbf{E}(\mathbf{r},t)\rangle$ is the power absorbed by atoms from a stream of photons with energy $\hbar\omega$, then re-emitted as dipole radiation, and $I(\mathbf{r}) = 2/(\epsilon_0 c)|E(\mathbf{r})|^2$ is the position-dependent intensity. The dipole potential, being related to the real part of the polarizability, depends on the part of the dipole that oscillates in phase with the external field. On the other hand, the photon scattering rate is related to the imaginary part of the polarizability and it thus describes the dissipative component, which is related to out-of-phase dipole oscillation.

In order to calculate the polarizability, while a purely classical model gives sometime reasonable results, generally, and also for lithium, a semi-classical approach is necessary. Here, the atom is approximated by a two-level quantum system with an energy separation of $\hbar\omega_A$ interacting with a classical radiation field. In this view, the atomic polarizability can be calculated using the spontaneous decay rate of the excited state $\Gamma = (\omega_A^3/3\pi\epsilon_0\hbar c^3)|\langle e|\,\hat{\mathbf{p}}\,|g\rangle|^2$, where $\langle e|\,\hat{\mathbf{p}}\,|g\rangle$ is the transition dipole matrix element for the electric dipole operator $\hat{\mathbf{p}} = -e\hat{\mathbf{r}}$. The dipole potential and the photon scattering rate are then given by

$$U_{dip}(\mathbf{r}) = -\frac{3\pi c^2}{2\omega_A^3}\left(\frac{\Gamma}{\omega_A-\omega} + \frac{\Gamma}{\omega_A+\omega}\right)I(\mathbf{r}) \tag{2.3}$$

$$\Gamma_{sc}(\mathbf{r}) = \frac{3\pi c^2}{2\hbar^2 w_A^3}\left(\frac{\omega}{\omega_A}\right)^3\left(\frac{\Gamma}{\omega_A-\omega} + \frac{\Gamma}{\omega_A+\omega}\right)^2 I(\mathbf{r}). \tag{2.4}$$

At too high intensities, the excited state becomes strongly populated and the above result is no longer valid. For dipole trapping, however, we are essentially interested in the far-detuned regime with very low saturation and scattering rates.

If the laser detuning $\Delta = \omega - \omega_A$ fulfills $|\Delta| \ll \omega_A$ we can use the so-called *Rotating Wave Approximation* (*RWA*) by neglecting the counter rotating term $\omega_A + \omega$ as

$$U_{dip}(\mathbf{r}) = -\frac{3\pi c^2}{2\omega_A^3}\frac{\Gamma}{\Delta}I(\mathbf{r}) \tag{2.5}$$

$$\Gamma_{sc}(\mathbf{r}) = \frac{3\pi c^2}{2\hbar^2\omega_A^3}\left(\frac{\Gamma}{\Delta}\right)^2 I(\mathbf{r}) \tag{2.6}$$

These expressions help to emphasize the two essential properties of dipole trapping. Firstly, the dipole potential and the scattering rate depend both on the intensity and the detuning of the laser, as I/Δ and I/Δ^2, respectively. In this way, the choice of large detunings and high intensities permits the creation of almost fully conservative potentials, limiting the scattering rate as much as possible for a given potential

depth. Secondly, the attractive or repulsive character of the potential experienced by the atoms depends on the sign of the detuning. Below the atomic resonance, where $\Delta < 0$, the potential is negative, and the dipole interaction attracts atoms into the light field realizing a red-detuned trap, whose potential minimum corresponds to positions in which the intensity is maximum. Above the resonance, instead, where $\Delta > 0$, the dipole interaction repels the atoms out of the beam giving rise to a blue-detuned trap, in which the potential minimum corresponds to the minimum of the intensity.

The same results can be obtained starting from a complete quantum mechanical treatment within the so-called *dressed-state* approach [22] [23], where also the electromagnetic field is quantized and the effects of the far-detuned laser light on the atomic levels are treated as second order perturbations of the electric field. In presence of a radiation the atomic spectrum is modified by the presence of the field, which induces an energy shift of the levels known as *ac Stark shift*. For low saturation, like those of interest for optical trapping, it is possible to interpret the *light-shifted ground state* $\Delta E = (3\pi c^2/2\omega_0^3)\,(\Gamma/\Delta)I$, as the relevant potential for the motion of the atoms, because the atoms reside most of the time in the ground state. In this view, the ground state level is lowered for red-detuned and raised for blue-detuned light.

However, in real multi-level atoms, the electronic levels have a complex substructure and we need to take into account contributions coming from every possible transition. For alkali atoms, first-order relativistic corrections, like the spin-orbit coupling, split the $ns \rightarrow np$ transition into the $D1$ ($nS_{1/2} \rightarrow nP_{1/2}$) and $D2$ ($nS_{1/2} \rightarrow nP_{3/2}$) line. Assuming that the detuning is large enough to allow to neglect the hyperfine splitting of the excited state, the total dipole potential is given by [21]

$$U_{dip}(\mathbf{r}) = \frac{1 - P g_F m_F}{3} U_{dip,\,D1}(\mathbf{r}) + \frac{2 + P g_F m_F}{3} U_{dip,\,D2}(\mathbf{r}) \tag{2.7}$$

where P describes the polarization of the light ($\pm 1 \rightarrow$ circular, $0 \rightarrow$ linear), g_F is the Landè g-factor, m_F is the magnetic quantum number of the hyperfine ground state. $U_{dip,\,D1}(\mathbf{r})$ and $U_{dip,\,D2}(\mathbf{r})$ depend on the respective detunings from the $D1$ and $D2$ transitions and their linewidths.

Polarizability of lithium atoms in a green laser beam

In this master thesis I will consider lithium atoms and a green trapping laser at $\lambda = 532$ nm, blue-detuned with respect to the main transitions of lithium. To realize an optical dipole trap with blue-detuned laserm, in order to anticonfine lithium atoms, we have to consider that: *i)* $D1 = 670.992$ nm and $D2 = 670.977$ nm are very close each other and thus we have to use both; *ii)*, the detuning is not much smaller than $D1$ and $D2$ lines and so we cannot use *RWA* neglecting $(\omega_A + \omega)^{-1}$ with respect to $(\omega_A - \omega)^{-1}$; *iii)*, the linewidth for the $D1$ and $D2$ lines is the same $\Gamma = 2\pi\ 5.87$ MHz; *iv)*, we consider linearly polarized light. With these assumptions, from Eq. (2.7), we obtain

$$U_{dip}(\mathbf{r}) = -\alpha_{dip}(\omega) I(\mathbf{r}) \tag{2.8}$$

where the real part of the polarizability is given in units [1] of $2\epsilon_0 c$ and it is written as

$$\alpha_{dip}(\omega) = \frac{\pi c^2 \Gamma}{2} \left[\frac{1}{w_{D1}^3} \left(\frac{1}{\omega_{D1} - \omega} + \frac{1}{\omega_{D1} + \omega} \right) + \frac{2}{w_{D2}^3} \left(\frac{1}{\omega_{D2} - \omega} + \frac{1}{\omega_{D2} + \omega} \right) \right]. \tag{2.9}$$

[1] According with Eq. (2.1) the relation is given by $\alpha_{dip}(\omega) = (2\epsilon_0 c)^{-1} Re(\alpha(\omega))$.

The value for $\omega \simeq 3.5$ THz, i.e. $\lambda = 532$ nm, is $\alpha_{dip} \simeq -8.518 \times 10^{-37}$ Jm^2/W.

2.1.1 Gaussian laser beam traps

The spatial intensity distribution of a circular laser beam with power P propagating along the z-axis can be approximated by an ideal Gaussian profile [24] described by

$$I_(\mathbf{r}) = I_0(z) \exp\left[-2\,\frac{r^2}{w^2(z)}\right] \tag{2.10}$$

with $I_0(z) = \frac{2P}{\pi w^2(z)}$ and $r^2 = x^2 + y^2$ where r denotes the radial coordinates. The waist of the beam $w(z)$ is defined as the width over which the intensity of the Gaussian beam decreases by a factor $1/e^2$ of its peak value and it depends on the axial coordinate z as

$$w(z) = w_0\sqrt{1 + \left(\frac{z}{z_R}\right)^2} \tag{2.11}$$

where the minimum radius w_0 is called the beam waist and $z_R = \pi w_0^2/\lambda$ denotes the Rayleigh range, i.e. the length below which the beam can be considered collimated: in particular at this distance the beam waist is $w(z_R) = \sqrt{2}w_0$. At $r = 0$ and $z = 0$, i.e. in the point in which the beam is focused, the intensity of the beam is given by $I_0 = 2P/\pi w_0^2$ and from this it is possible to derive the trap depth $U_0 = -\alpha_{dip}(\omega) I_0$.

If the thermal energy of an atomic ensemble $k_B T \ll U_0$, i.e. the sample size in the radial direction is small compared to w_0 and in the axial direction it is small compared to z_R, it is possible to use a harmonic approximation to extract the trap frequencies. This can be considered a reasonable assumption since the atoms are confined principally in the centre of the trap. The dipole potential in the harmonic approximation is

$$U_{dip}(\mathbf{r}) \simeq U_0\left(1 - 2\frac{r^2}{w_0^2} - \frac{z^2}{z_R^2}\right) \tag{2.12}$$

and from the comparison to a harmonic potential $U_{harm}(\mathbf{r}) = \frac{1}{2}m(\omega_r^2 r^2 + \omega_z^2 z^2)$, one can define the radial and axial trap frequencies

$$\omega_r = \sqrt{\frac{4U_0}{m w_0^2}}, \qquad \omega_z = \sqrt{\frac{2U_0}{m z_R^2}} \tag{2.13}$$

where we can observe that the axial confinement is typically much weaker than the radial one, because z_R is usually much larger than w_0, and therefore the trapping potential generated by a single focused beam is very anisotropic. As U_0 is proportional to P/w_0^2 and z_R to w_0^2, the dependence of the trap frequencies both on the power and on the beam waist is given by $\omega_r \propto \sqrt{P}/w_0^2$ and $\omega_z \propto \sqrt{P}/w_0^3$.

In the master thesis, in order to realize trapping potential with highly anisotropic trap frequencies (see Section 2.3 and 3.2.2), I will deal with elliptical Gaussian beams. All the considerations done for a circular beam can be easily extended for this more general case. The distribution intensity of such a laser beam can be written as

$$I_{ell}(\mathbf{r}) = I_{0\,ell}(z) \exp\left[-2\left(\frac{x^2}{w_x^2(z)} + \frac{y^2}{w_y^2(z)}\right)\right] \tag{2.14}$$

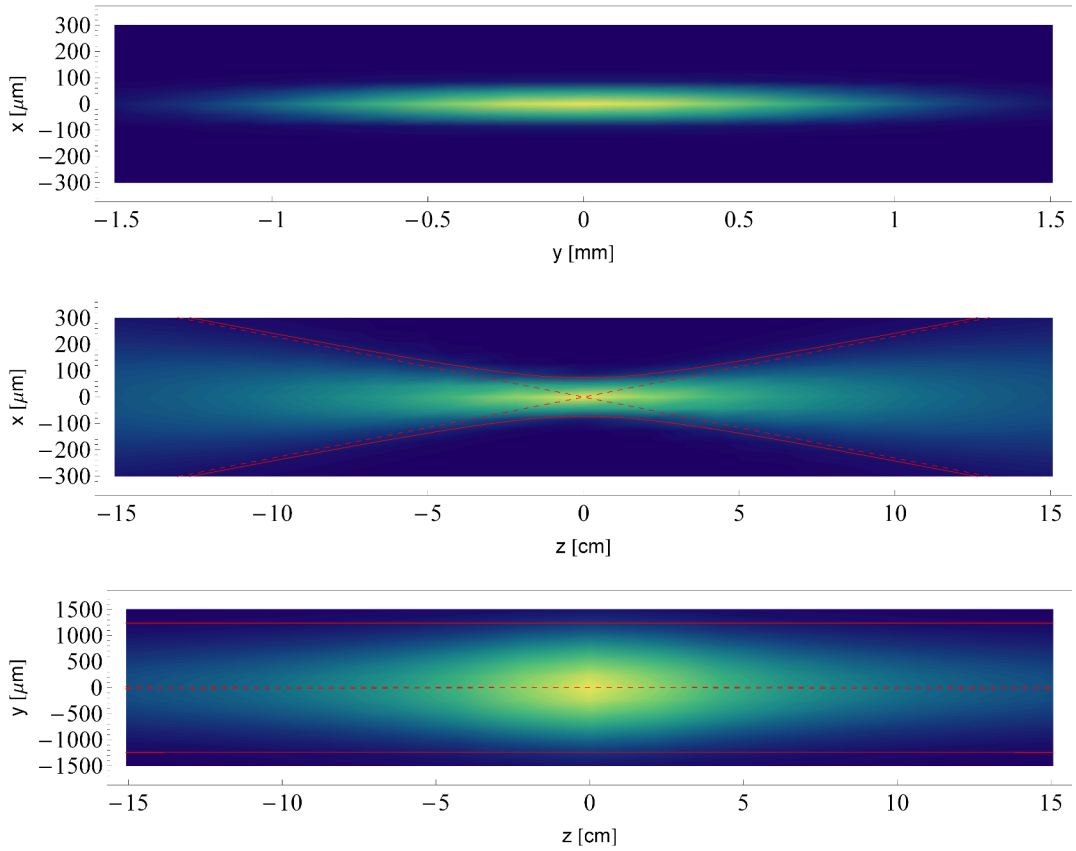

FIGURE 2.1: Spatial intensity profile of a highly elliptic focused Gaussian beam. As an example, the profile calculated for $w_{0x} = 70\,\mu$m and $w_{0y} = 1200\,\mu$m is shown.

with $I_{0\,ell}(z) = \frac{2P}{\pi w_x(z) w_y(z)}$, and new waists in the radial directions x and y, each of them characterized by its own beam waist w_{0i} and Rayleigh range z_{Ri}

$$w_i(z) = w_{0i}\sqrt{1 + \left(\frac{z}{z_{Ri}}\right)^2}, \qquad i = x, y \tag{2.15}$$

Within the harmonic approximation of the dipole trap, close to the focus, we have

$$U_{dip}(\mathbf{r}) \simeq U_{0ell}\left(1 - 2\frac{x^2}{w_{0x}^2} - 2\frac{y^2}{w_{0y}^2} - \frac{z^2}{z_{Rell}^2}\right) \tag{2.16}$$

where $U_{0\,ell}$ is calculated in the same way as for a circular beam, but taking into account that the effective beam waist $w_{0\,ell}$ is defined as the geometric mean of the beam waists in the radial directions, $w_{0\,ell} = \sqrt{w_{0x} w_{0y}}$, and the effective Rayleigh range is given by $z_{R\,ell} = \sqrt{\frac{2 z_{Rx}^2 z_{Ry}^2}{z_{Rx}^2 + z_{Ry}^2}}$, where z_{Rx} and z_{Ry} are the Rayleigh ranges along the z-direction associated with w_{0x} and w_{0y}, respectively. Using the same procedure as above, the trap frequencies for a single elliptic beam are the following:

$$\omega_x = \sqrt{\frac{4U_{0\,ell}}{m w_{0x}^2}}, \qquad \omega_y = \sqrt{\frac{4U_{0\,ell}}{m w_{0y}^2}}, \qquad \omega_z = \sqrt{\frac{2U_{0\,ell}}{m z_{R\,ell}^2}}. \tag{2.17}$$

2.2 Optical lattices

One of the most successful among optical potentials is the optical lattice, which exploits optical dipole force and light interference to create a very tight confinement, effectively changing the dimensionality of the space in which atoms can move. This offers the possibility to realize a great variety of trapping geometries, such as highly anisotropic or multi-well potentials. The lower the dimensionality that one wants to achieve, the higher is the number of laser beams that one has to use: in an optical lattice, the atomic motion can be indeed frozen along one, two, or three spatial dimensions. More generally, optical lattices can be used to emulate the crystalline structure of solids with ultracold atoms, enhancing the role of interactions and allowing to explore the strong correlation phenomena typical of condensed matter systems.

To realize a two-dimensional confinement, two laser beams interfering with equal polarization are necessary. In general, the intensity of two superimposed monochromatic plane waves with equal frequency and complex amplitude $E_1(\mathbf{r}) = E_0 \exp i(\mathbf{k}_1\mathbf{r}_1 + \delta_1)$ and $E_2(\mathbf{r}) = E_0 \exp i(\mathbf{k}_2\mathbf{r}_2 + \delta_2)$ is given by [25]

$$I_{latt}(\mathbf{r}) = I_1(\mathbf{r}) + I_2(\mathbf{r}) + 2\sqrt{I_1(\mathbf{r})I_2(\mathbf{r})}\cos\Delta\theta(\mathbf{r}), \tag{2.18}$$

where $\Delta\theta(\mathbf{r}) = \mathbf{kr} + \delta$ is the difference between the argument of the two waves[2], and $I_1(\mathbf{r}) = |E_1(\mathbf{r})|^2$ and $I_2(\mathbf{r}) = |E_2(\mathbf{r})|^2$ are the intensity profiles. If the intensity distribution of the two beams is the same, i.e. $I(\mathbf{r})$, then we obtain

$$I_{latt}(\mathbf{r}) = 4\, I(\mathbf{r})\, \cos^2\Big(\frac{\Delta\theta(\mathbf{r})}{2}\Big). \tag{2.19}$$

The most common way of creating an optical lattice is to retro-reflect a Gaussian laser beam off a mirror over itself, generating a standing wave by the interference between the two counter-propagating waves. This produces a 1D periodic potential of the form

$$U_{latt}(\mathbf{r}) = 4U_{dip}(\mathbf{r})\cos^2\Big(\frac{\Delta\theta(\mathbf{r})}{2}\Big), \tag{2.20}$$

where $U_{dip}(\mathbf{r})$ is the dipole potential of the single beam and $\Delta\theta(\mathbf{r})$ is the phase difference, which vanishes at the location of the retro-reflecting mirror. $\Delta\theta(\mathbf{r})$ is given by a more complicated expression than that for a plane wave[3], but in the waist of the beam the only important term is that of a plane wave. Therefore, considering a beam propagating in the z-direction and the focus position, we can write

$$U_{latt}(\mathbf{r}) = 4U_{dip}(\mathbf{r})\cos^2(k_L z) \tag{2.21}$$

where $k_L z = \Delta\theta(\mathbf{r})/2$ and $k_L = \pi/d$ is the lattice wave vector, which determines the spacing d.

In the case of a retro-reflected lattice, k_L is directly associated with the wave vector of the laser $k = 2\pi/\lambda$, resulting in a periodicity of $d = \lambda/2$. For example, for $\lambda = 532\,\text{nm}$ the lattice spacing would be just 266 nm. On the other hand, crossing two independent beams with parallel polarization at an angle between 0 and $\pi/2$ gives the possibility of creating lattices with larger spacing. If the two beams

[2] Namely, $\mathbf{k} = \mathbf{k}_1 - \mathbf{k}_2$, $\mathbf{r} = \mathbf{r}_1 - \mathbf{r}_2$ and $\delta = \delta_1 - \delta_2$.

[3] The position-dependent phase of the electric field of a Gaussian beam is given by $\theta(\mathbf{r}) = \mathbf{kr} + kr^2/2R(\mathbf{r}) - \zeta(\mathbf{r})$ (see [24]), whereas that of a plane wave is simply $\theta(\mathbf{r}) = \mathbf{kr}$. In both cases, a phase constant δ can be added from a reference point.

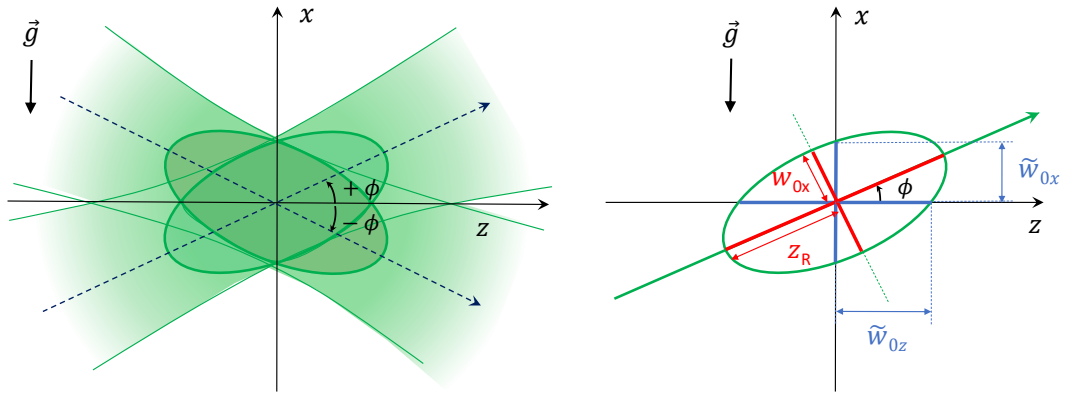

FIGURE 2.2: Definition of the potential radii in the $x-z$ plane. Left panel: Two beams propagating in the $x-z$ plane cross each other at an angle of $\pm\phi$, with respect to the z-axis. Right panel: The dimensions of the interference region are given by the intersection of the ellipses describing the foci of the two beam with the axes. Gravity is oriented the along x-axis.

propagate respectively at an angle of $\pm\phi$ from the z-axis in the $x-z$ plane, in the $z=0$ plane the lattice wave vector equals $k_L = \pi \sin\phi/\lambda$, and the lattice spacing is therefore given by:

$$d = \frac{\lambda}{2\sin\phi}. \tag{2.22}$$

By changing the angle between the two beams, it is possible to adjust the lattice spacing. Large spacings correspond to small crossing angles, whereas large angles produce denser interference patterns. If the two beams have the same intensity profile, tuning the mutual angle between them does not change the total trap depth, but it only influences the trapping frequencies and their dependence on the beam waists and powers. To investigate the dependence of trapping frequencies on the beam parameters, we can describe the geometry of the trap created by the beam propagating at $+\phi$ as an ellipse in the $x-z$ plane, $\frac{x^2}{a^2}+\frac{z^2}{b^2}=1$, where $a = w_{0x}$ and $b = z_R$, as shown in Fig. 2.2. When this ellipse is rotated into the used coordinate system at an angle ϕ, the potential radii are given by

$$\tilde{w}_{0x}(\phi) = \sqrt{\frac{1}{\frac{\cos^2(\phi)}{w_{0x}^2}+\frac{\sin^2(\phi)}{2z_R^2}}} \tag{2.23}$$

$$\tilde{w}_{0z}(\phi) = \sqrt{\frac{1}{\frac{\sin^2(\phi)}{w_{0x}^2}+\frac{\cos^2(\phi)}{2z_R^2}}}, \tag{2.24}$$

and for $\phi = 0$, the potential radii reduce to the waist and the Rayleigh range $\tilde{w}_{0x} = w_{0x}$ and $\tilde{w}_{0z} = z_R$. $\tilde{w}_{0x}$ and $\tilde{w}_{0z}$ give the dimensions of the intersection region between the two beams. In their definitions, the factor of 2 next to z_R takes into account that the confinement in the axial direction is weaker than the radial one. Considering

that the two beams intersect each other in their own foci, and with the same assumptions made before, we can then write the lattice trapping potential in the harmonic approximation as

$$U_{latt}(\mathbf{r}) \simeq 4U_0 \cos^2(k_L x)\left(1 - 2\frac{x^2}{\tilde{w}_{0x}^2(\phi)} - 2\frac{y^2}{w_{0y}^2} - \frac{z^2}{\tilde{w}_{0z}^2(\phi)}\right). \tag{2.25}$$

The x-dependence of the trap depth reflects the effect of the interference between the two waves, which lead to the lattice modulation. The relevant trapping frequencies in this case are given by:

$$\omega_{x\ lattice}(\phi) = \sqrt{\frac{8\pi^2 U_{0\ ell}}{md^2(\phi)}}, \qquad \omega_y(\phi) = \sqrt{\frac{16U_{0\ ell}}{mw_{0y}^2}}, \qquad \omega_z(\phi) = \sqrt{\frac{16U_{0\ ell}}{m\tilde{w}_{0z}^2(\phi)}}. \tag{2.26}$$

2.3 Desired lattice properties

The main goal of this thesis is the realization of a suitable optical potential for the confinement of ultracold fermionic atoms of lithium in two dimensions. The realization of this kind of potential will provide an essential step for the future investigation of 2D fermionic systems. In our ultracold lithium experiment, we load fermionic atoms from a magneto-optical trap into an optical dipole trap in which atoms are evaporatively cooled to quantum degeneracy. In order to transfer a large number of atoms in a 2D geometry, we will first transfer the sample from the three-dimensional dipole trap into a strongly-anisotropic single-beam trap. From such intermediate trap, the atoms will then be loaded into a large-spacing optical lattice. During this thesis, I have designed and built the optical lattice set-up which will be integrated into the experiment in the near future for this purpose. In the following Section, I present the main considerations which have determined the design of the realized trapping potential. The requirements are two-fold. First, the trapping frequencies $\omega_x, \omega_y, \omega_z$ need to be chosen to guarantee that the system is effectively 2D for the typical gas temperature and atom number in the experiment. This requirement guides the choice of the lattice beam waists, the angle 2ϕ between the lattice beams and their power P_0. Second, the tunneling properties in the lattice potential should be conveniently flexible, giving the possibility of coupling different gases trapped in different minima of the lattice potential while maintaing their quasi-2D character. The tunnelling in the lattice also depends on the lattice beam intensities and on the lattice spacing d. In order to correctly design the lattice set-up for achieving the desired properties, I have initially modelled the potential using a computer program to calculate all the relevant quantities and their dependence on the lattice beam parameters.

2.3.1 Trapping frequencies

Conditions for creating a quasi-2D system

As already explained in Chapter 1, to realize a quasi-2D system we need to confine the atoms in a harmonic trap that is much more tightly confining along the x-direction than along the other two, y and z. In particular, to achieve a quasi-2D Fermi gas, the thermal and the Fermi energy have to satisfy the criterion $k_B T, \epsilon_F \ll \hbar\omega_x$,

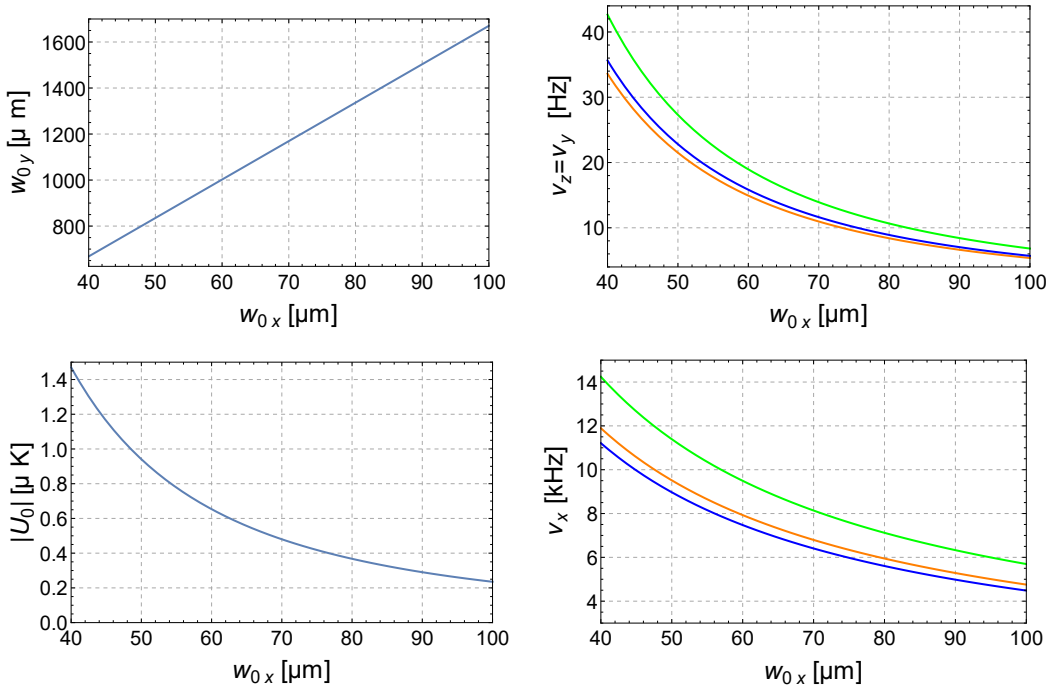

(A) *Single-beam features* (B) *Trap frequencies*

FIGURE 2.3: Trend of the relevant quantities for quasi-2D confinement as a function of the vertical waist size of the single lattice beams at 532 nm(which shall be equal for the two beams). All quantities have been obtained after imposing that the in-plane frequencies ν_y and ν_z are equal. *(A)* In the upper panel, the relation written down in Eq. (2.30) is shown between the beam waist along the y-direction (horizontal), w_{0y}, and the beam waist in the x-direction (vertical), w_{0x}, for a single beam propagating at an angle of 3° with respect to the yz-plane. In the lower panel, the single-beam potential strength U_0 is plotted as a function of w_{0x}. *(B)* In the upper panel, the in-plane trap frequencies ν_y and ν_z are plotted as a function of w_{0x}. In the lower panel, the axial trap frequency ν_x is plotted as a function of w_{0x}. In both panels, P_0 is taken equal to 1 W. In both panels, the colored curves correspond to different beam crossing angles ϕ: 2.70° (orange), 3.05° (blue) and 3.43° (green).

where ω_x is the axial trapping frequency. The gas is then confined to only the lowest transverse harmonic oscillator state in the axial direction. The critical number of atoms N_{crit} below which the quasi-2D condition is satisfied is discussed in detail in Section 1.2.2, and $N_{crit} \approx 2.5 \times 10^4$ with $\omega_x \simeq 2\pi\, 7.5\,\text{kHz}$ and $\omega_{y,z} \simeq 2\pi\, 30\,\text{Hz}$. Therefore, to ensure the quasi-2D trapping of large atomic samples $N_{crit} > 10^4$ with weak in-plane confinement, axial frequencies of at least several kHz are necessary.

Conditions for creating a circularly symmetric sample

To obtain a circular, horizontally isotropic sample in the quasi-2D regime, the in-plane frequencies must be approximately equal. For a blue-detuned lattice potential, the potential is anti-confining and the in-plane frequencies are therefore imaginary. As discussed at the end of this Chapter, additional potentials are thus needed to confine the atoms in plane. However, having equal in-plane imaginary frequencies from the lattice potential is still the most convenient starting point to create approximately circular samples. For a lattice created by the interference of two beams propagating at angles $\pm\phi$ from the z-axis in the $x-z$ plane, the condition $\omega_y = \omega_z$ imposes a precise relation between the dimensions of the beam waists. Using Eq. (2.26), we

find that the in-plane frequencies are related as follows

$$\omega_y = \omega_z \frac{w_{0y}}{\tilde{w}_{0z}(\phi)}, \tag{2.27}$$

and imposing that the two frequencies are equal, we have:

$$\frac{1}{w_{0y}^2} = \frac{\sin\phi^2}{w_{0x}^2} + \frac{\cos\phi^2}{z_R^2}. \tag{2.28}$$

From this, we can finally write:

$$\frac{1}{w_{0y}^2} = \frac{\sin\phi^2}{w_{0x}^2} + \cos\phi^2 \frac{\lambda^2}{4\pi^2}\left(\frac{1}{w_{0x}^4} + \frac{1}{w_{0y}^4}\right). \tag{2.29}$$

The explicit relation between the beam waists w_{0y} and w_{0x} to ensure that $\omega_y = \omega_z$ is therefore

$$w_{0y} = \pm\sqrt{\frac{w_{0x}^4}{2(Aw_{0x}^2 + B)} \pm \sqrt{\frac{w_{0x}^8}{4(Aw_{0x}^2 + B)^2} - \frac{Bw_{0x}^4}{(Aw_{0x}^2 + B)}}}, \tag{2.30}$$

where $A = \sin\phi^2$ and $B = \cos\phi^2 \frac{\lambda^2}{4\pi^2}$. The trend of the relevant trap parameters has been calculated when this relation is fulfilled. In Fig. 2.3, the trap depth and frequencies are plotted for blue-detuned lattice beams at 532 nm.

2.3.2 Tunneling properties

Single-layer configuration

For the study of a single two-dimensional system, it is mandatory to load a single minimum of the lattice potential. The efficiency of the atom transfer from the dipole trap into a single node of the lattice, i.e. an highly anisotropic trap, depends on the overlap and the position matching between the minimum of the optical dipole trap and that of the deepest minimum of the optical lattice. The main requirement for obtaining an efficient loading into a single lattice minimum is therefore to have a large number of atoms contained within the volume of a single pancake when the lattice is turned on. To this purpose, a large-spacing optical lattice represents the optimal choice, as it offers the optimal trade-off between tight axial confinement and large single-minimum width, rendering the loading process more practical and efficient.

To aid the loading of a single lattice plane, it is convenient to prepare a molecular BEC in the dipole trap, since its density is much higher than that of a degenerate Fermi gas. Another way to prepare a single two-dimensional trap would be to transfer atoms from a full dipole trap into a stack of pancakes, and subsequently empty all of them except the central one by a spatially-selective removal. This can be achieved for instance by driving internal state transitions [26] [27]. However, this procedure may lead to an important atom loss, that is detrimental for exploring large systems. A very clever way to load many atoms in the quasi-2D regime is to realize a dynamically tunable confinement using a so-called "optical accordion". This consists a large-spacing optical lattice where the angle between the two interfering lattice beams can be dynamically increased, making the confinement stronger only after the loading process of a single minimum has been completed (see Section 2.5.2).

Multi-layer configuration

The realization of a large-spacing optical lattice allows to realize a multi-layer gas of atoms, where several planes are populated and whose coupling can be varied by tuning the power of the lattice beams. Depending on the height of the potential barriers between the planes, the atomic wave function will be more or less delocalized over different potential wells. To create isolated quasi-2D atomic samples, the potential depth in each lattice minimum must be sufficiently high to separate the samples from one another, suppressing the tunneling of atoms between them. The tunneling is influenced by two lattice parameters: the intensity of the lattice beams I_0, and the spacing of the lattice d. The tunneling rate can be roughly estimated starting from the barrier parameters, considering single-particle eigenstates in an infinite periodic potential, as described in [28]. The potential has a tunable amplitude $4U_0$, where $U_0 = -\alpha_{dip}(\omega)I_0$ is the potential height for a single beam with intensity I_0, defined in Subsection 2.1.1. The lattice depth is typically given in units of the lattice recoil energy

$$E_R = \frac{\hbar^2 k_L^2}{2m} = \frac{h^2}{8md^2} = \frac{h^2}{2m\lambda^2}\sin^2\phi, \tag{2.31}$$

which is the kinetic energy of an atom with mass m and momentum $k_L = \pi/d$, where d is the spacing of the lattice. The tunneling energy $J > 0$ is the kinetic energy gain due to the tunneling from one potential well to the neighbouring one. In the limit $U_0 >> E_R$, the tunneling energy is obtained from the 1D Mathieu equation [28] and is given by

$$J \approx \frac{4}{\sqrt{\pi}} E_R \left(\frac{4U_0}{E_R}\right)^{3/4} \exp\left[-2\left(\frac{4U_0}{E_R}\right)^{1/2}\right]. \tag{2.32}$$

The light mass of ^{6}Li atoms yields an particularly large recoil energy, e.g. $E_R/k_B \simeq 16\,\mathrm{nK}$ with $d \simeq 5\,\mu\mathrm{m}$. This allows lithium atoms to tunnel very efficiently, so that atomic clouds trapped in different lattice minima can be coupled by inter-layer tunnelling. By estimating the tunneling energy as a function of the lattice spacing for a fixed beam power $P_0 = 1$ W, i.e. for a fixed depth of the potential $4U_0 = 1.5\,\mu$K, and fixed wavelength $\lambda = 532\,\mathrm{nm}$, we can choose the lattice spacing to give a low tunneling rate, negligible over the typical timescale of the experiment on the order of few seconds. Then, by fixing now the lattice spacing, we can determine how the tunneling rate changes from very low to considerable values by decreasing the power of the lattice beams, varying consequently the coupling between different sites of the lattice. For a large-spacing optical lattice, with $d \approx 5\,\mu$m, this crossover is achieved at a relative low laser power below 1 W. Conversely, lattices realized by retro-reflected beams are limited by the larger wave vector of the laser: as shown in Fig. 2.4 for $\lambda = 532\,\mathrm{nm}$, low tunneling rates are obtained only at very high laser power. Thus, the realization of a large-spacing lattice provides the possibility to control the coupling between different lattice planes only by the adjustment of the laser power. In this way, it is possible to explore the crossover from the 3D to the 2D regime, and to study the role played by layering on fermionic superfluids, mimicking the geometry of high-T_c layered superconductors.

Based on all considerations discussed above, we will present in the next Sections the implementation of a large-spacing optical lattice with blue-detuned laser beams (see Section 2.1).

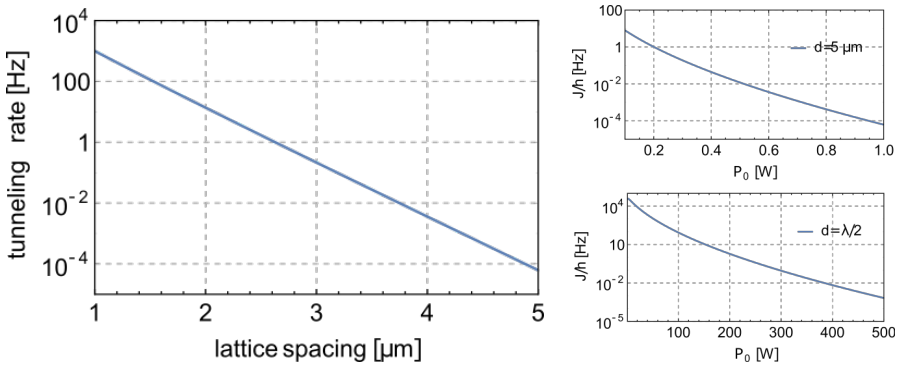

FIGURE 2.4: (Left) The tunneling rate J/h is plotted as a function of d for a lattice with a potential depth of approximately 1.5 μK, corresponding to a laser power of 1 W at a wavelength of 532 nm, and beam waists of about 60 μm and 1600 μm. (Right) The tunneling rate J/h is plotted as a function of the laser power for a large lattice spacing of 5 μm (up) and of 266 nm (down).

2.4 Optical lattice scheme

In the context of this thesis, we have chosen to produce a large-spacing optical lattice with blue-detuned laser beams (see Section 2.1).The particular scheme that was devised for creating the lattice interference pattern will be discussed here below. The scheme is based on two coherent laser beams with a fixed phase relation that initially run parallel to the optical axis, with a displacement of D from one another. These beams pass through a focalizing lens where they are refracted and intersect under an angle of 2ϕ at the focal point where they interfere to form the lattice (see Fig. 2.5). The pattern of interference is given by the formula in Eq. (2.21), whereas the lattice constant by Eq. (2.22). To relate the angle ϕ to the displacement D, and thus to the focal length f of the objective, which are the experimental parameters that can be chosen, one has to take into account that the thin lens approximation breaks down for high numerical aperture lenses. These are usually designed to fulfill the Abbe sine condition for imaging both on and off the optical axis with minimal optical aberrations [29] [30]. For incident beams parallel to the optical axis it reads

$$\sin\phi = \frac{D}{2f} \tag{2.33}$$

and using this it is possible to rewrite the lattice constant as

$$d = \frac{\lambda f}{D}. \tag{2.34}$$

So, the lattice spacing can be tuned to the desired value, for a given wavelength, by choosing an appropriate ratio of the lens focal length and the beam displacement. In spite of this, there is a lower bound that is determined by the maximum aperture of the objective. First, I have chosen a lens with a long focal length $f = 15$ cm, and then I have chosen a distance between the beams that produce a lattice spacing of about 5 μm. For this, the ideal distance between the beams would be $D = 1.53$ cm. The best optical elements that were available (see below) could produce a beam separation of either 14.14 mm or 17.96 mm, leading to a lattice spacing of 5.64μm and 4.44μm as shown in table 2.1.

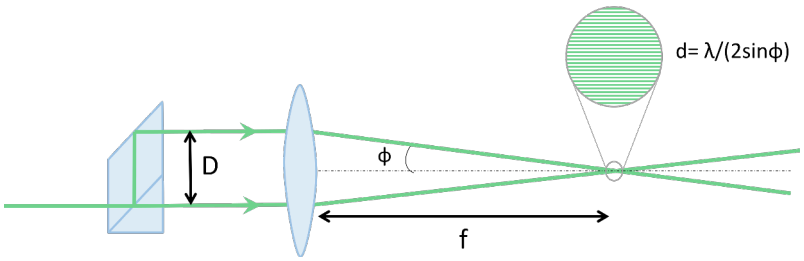

FIGURE 2.5: Sketch of the optical scheme for producing the lattice interference pattern. Two identical parallel beam are generated by a lateral displacement prism and propagate through a lens, that makes them interfere in their respective foci.

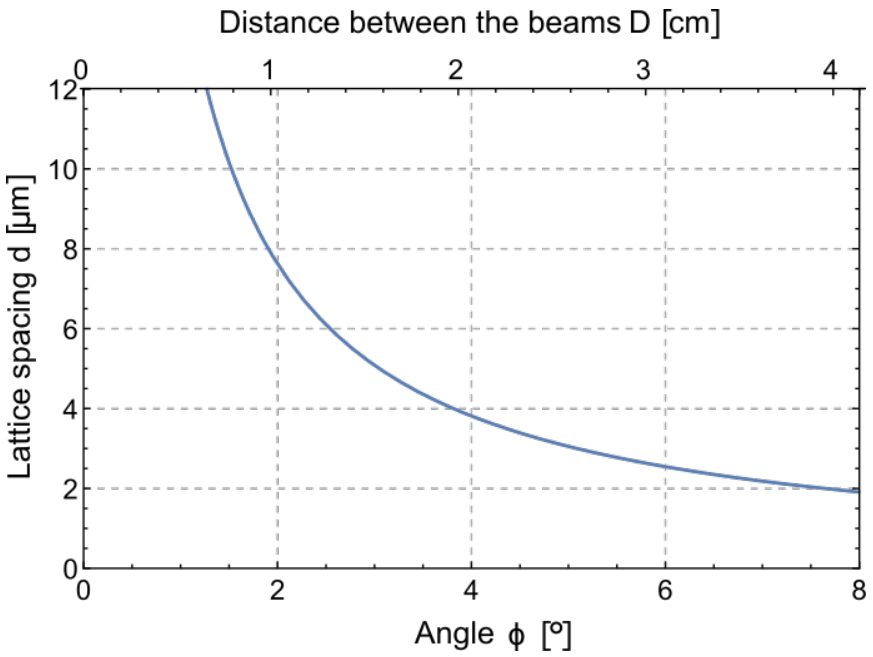

FIGURE 2.6: Lattice spacing in the focus of a $f = 150$ mm lens, i.e. the atom cloud position, as a function of the distance D between the parallel propagating beams (top axis) as well as of the semi-angle ϕ between them (bottom axis).

	$f[mm]$	$D\ [mm]$	$d\ [\mu m]$	$\phi[^\circ]$
desired	150	15.96	5.00	3.05
displacement prism 1 (used)		17.96	4.44	3.43
displacement prism 2		14.14	5.64	2.70

TABLE 2.1: For a focal length $f = 150$ mm, and for different values of the displacement between the two beams D, the expected values of the lattice spacing d are given, associated with the angles ϕ.

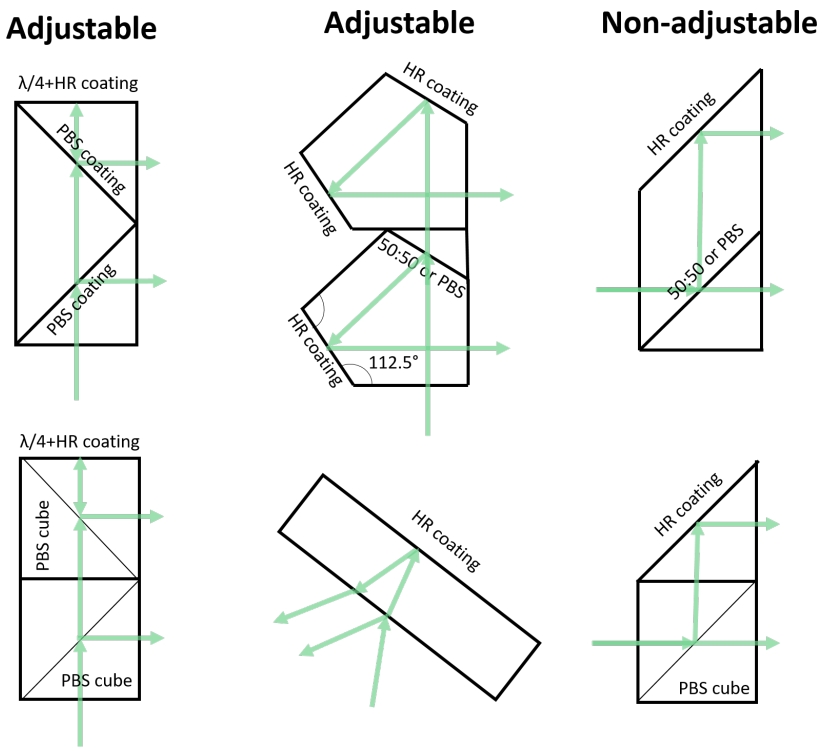

FIGURE 2.7: Sketch of some proposed configurations of prism ensambles for creating two parallel beams. "Adjustable" solutions allow for varying the distance between the outcoming beams by changing the point of entrance on the input surface. The plate beam-splitter is the most compact solution, but it depends on the refraction index of the glass and on the width of the plate. In this solution, the distance between the two outcoming beams varies changing the angle of incidence of the incoming. Our final choice has been the non-adjustable ensemble of prisms composed by right-angle and rhombic prisms (upper right sketch).

2.4.1 Lateral displacement prism

Our first challenge concerned the choice of the best optical element to separate a single laser beam into two parallel propagating beams with a stable phase relation. The beams have to be coherent and they have to propagate in the vertical plane with the same polarization. One can imagine two solutions: to realize an interferometer with active stabilization of the phase (see e.g. [31]) or with passive stabilization. Furthermore, the device could produce tunable (see e.g. [32]) or not tunable beam displacement (see e.g. [33] [26] [27]). Some of the different conceptual schemes that we have considered are shown in Fig. 2.7. In this thesis work, we have chosen to implement a passively stable scheme by using a lateral-displacement polarizing beam separator (PBS). After the separation, the beams traverse the same optical elements, minimizing therefore the disturbances of the relative phase between the beams.

Our lateral displacement PBS is composed by a right-angle prism that is optically contacted with a rhombic prism, and was manufactured by Lambda Research. The rhombic prism is used to displace a beam laterally without changing its direction. The contacting surface is coated to produce a polarizing beam separator: it transmits part of the incoming beam and gives rise to two parallel and displaced outgoing beams. Both prisms are manufactured from BK7A, and their most relevant specifications are shown in table 2.2. I have verified that the angular deviation for one of the prism ensembles is less then 3 arcmin: over a distance of $l = 3.10\,\mathrm{m}$, the displacement between the two beams remains within $\Delta = 0.10$ mm from the declared

	displacement prism 1 (used)	displacement prism 2
dimension A	12.7 mm	10.00 mm
dimension C	12.7 mm	10.00 mm
length B	17.96 mm	14.14 mm
surface flatness	$\lambda/8$ @633nm	$\lambda/8$ @633nm
surface quality	20/10	20/10
parallelism	< 3 arc-min	< 3 arc-min
beam deviation	< 3 arc-min	< 3 arc-min
Bevel	0.3mm@45deg	0.3mm@45deg
CAl	>85% of circular dimension	>85% of circular dimension

TABLE 2.2: Specification of the lateral displacement PBSs.

value; this leads to a deviation angle of $\theta_{err} = \arctan(\Delta/l) = 0.1$ arcmin. Moreover to test the surface flatness, I have performed wavefront analysis measurements using a wavefront sensor (see Section 3.1.2). The surfaces at the interface between the right-angle and the rhombic prism are optically contacted and the PBS coating is specified up to very large light intensities, reflecting the s-wave component of the light with a $R_s > 99.5\%$ and transmitting the p-wave component with a $T_p > 95\%$ at 532 nm and 45°. The input and output surfaces of the prisms have an antireflection coating with $R < 0.25\%$ at 532 nm and 0°. The ratio between $T_p/T_s > 200:1$. This is verified measuring the power of the lower beam reflected and transmitted by the 2" PBS (it transmits s-polarization and reflects p-polarization) with a power-meter: the ratio between the power reflected and transmitted is found to be larger than 50:1.

2.5 Optical lattice setup

Based on the design scheme described in the previous Section, the one-dimensional lattice set-up has been implemented experimentally. This Section will focus on the description of the lattice setup which was designed and built in the course of this master thesis. Since the scheme presented above is able to tightly confine the atoms only along one direction (x), an supplementary optical potential is necessary to confine the atoms in the $y-z$ plane, in order to prevent them to escape. Possible choices for the additional potentials for the radial confinement will be suggested briefly in Section 2.5.1.

The optical system required to obtain the beam waist dimensions corresponding to the desired trap frequencies have been computed by implementing the ABCD matrix method [24]. This method allows to calculate the propagation of Gaussian beams through various optical structures. To produce the desired waists, we have chosen to implement a spherical telescope that suitably resizes the beam before it is split and a cylindrical lens, that is used together with the last $f = 150$ mm focalizing lens to collimate the beams along the horizontal direction (see Fig. 2.8).

To generate the lattice beams, we use a diode-pumped solid-state laser (Verdi V-8 Coherent Laser Division) with a total available power output of 8 W. The laser wavelength of 532 nm is blue-detuned with respect to the D1 and D2 lithium transitions (see Section 1.6). The laser output passes through an acousto-optic modulator (AOM), which operates at 80 MHz and is used to regulate and actively stabilize the

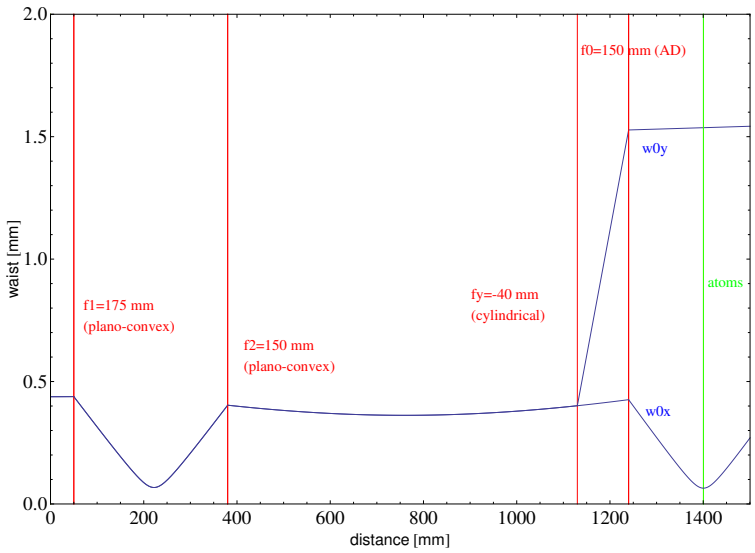

FIGURE 2.8: Computed beam profiles, showing the propagation of the waist sizes along the two driections x and$y$, requiring that trap frequencies in the plane are approximately equal while the axial confinement frequency is as high as 10 kHz with a power of 1 W per lattice beam.

power of the beam used for generating the lattice. After the AOM, the beam is coupled into a high-power polarization-maintaining optical fiber (NKT Photonics). The laser beam travels in the fiber to the optical bank where I have constructed the set-up for the lattice. The entire lattice set-up was built on a transportable bread-board already, which was cut to fit into the tight setup on the main optical table where the lithium experiment is placed.

The beam exiting the fiber is collimated by a fiber collimator (Shaefter+Kirchhoff 60FC-4-A7.5-01), and it passes firstly through a waveplate $\lambda/2$ and a 1/2" polarizing beam splitter (PBS) to adjust and clean its polarization. The power reflected by the PBS is sent to a photodiode (PD) (Thorlabs DET36A/M) to monitor possible undesired variations in the beam polarization. The transmitted beam propagates into a telescope composed by two lenses, in order to reduce the waist dimensions of the beam by about 3/4. The telescope consists of two 1" plano-convex lenses L1 and L2: the first (Thorlabs LA4924-YAG) has a focal of $f_1 = 175.0$ mm, whereas the second (Thorlabs LA1433-YAG) has a focal of $f_2 = 150.0$ mm. The choice of the telescope magnification factor is based on the ratio between the real dimensions of the waist at the output of the collimator and the waist necessary to have the desired trap frequency at the atoms position. On this path the 1" mirrors M1, M2 and M3 with a HR coating at $\lambda = 532$ nm are placed in a 30 mm cage system, on right-angle kinematic mirror mounts (Thorlabs KCB1C/M), to be rigidly muonted with the two lenses, which are inserted in the cage system too, using standard cage plates (Thorlabs CP02/M). The mirror M2 has a high reflectivity for 532 nm but a tiny transmitted fraction is used for monitoring purposes, focused by a plano-convex lens of focal $f = 50$ mm on a photodiode (PD) (Thorlabs PDA 36A-EC) used for the stabilization procedure of the intensity laser noise. In the cage system between the mirrors M2 and M3, a pinhole can be placed if required to filter the beam profile in the focus of the telescope (for the moment that was not necessary). After the M3 mirror the beam passes through a second $\lambda/2$ waveplate (Lambda WP0-12.7CQ-0-2-532) used to change the orientation of the polarization of the beam, and which controls the relative power of the two parallel beams. It is then reflected by the mirror M4 mounted

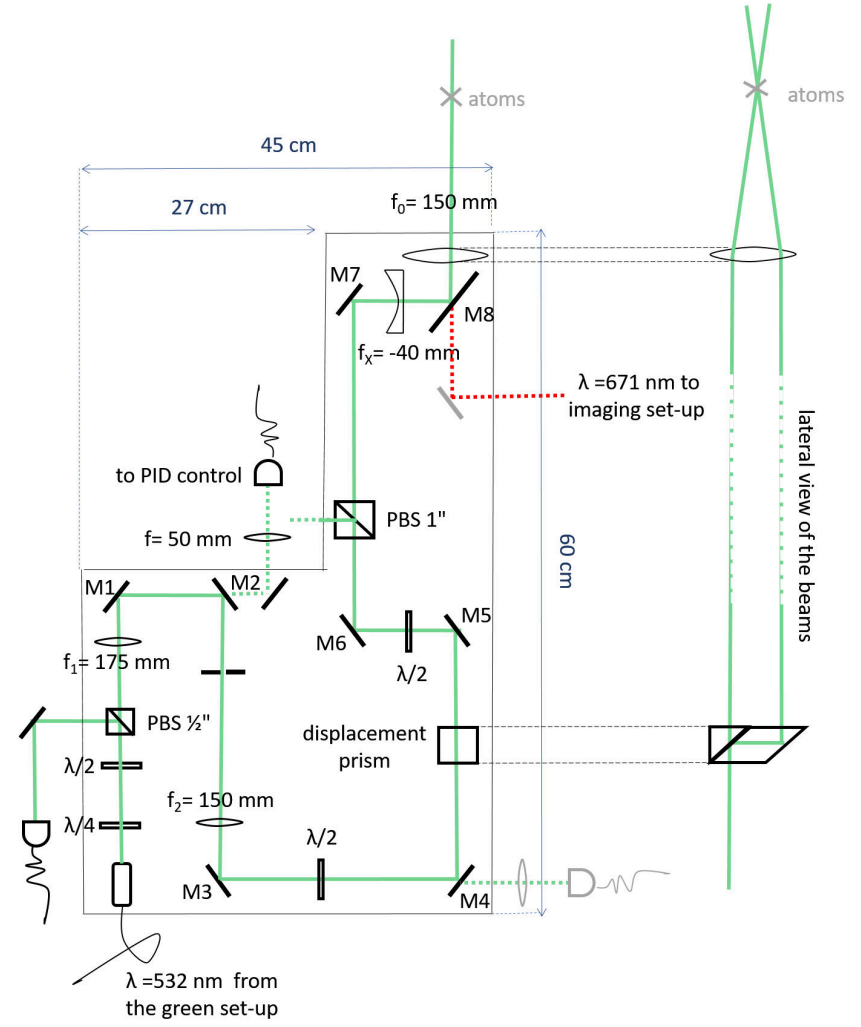

FIGURE 2.9: Sketch of the optical lattice set-up. All the elements are introduced and discussed in the text.

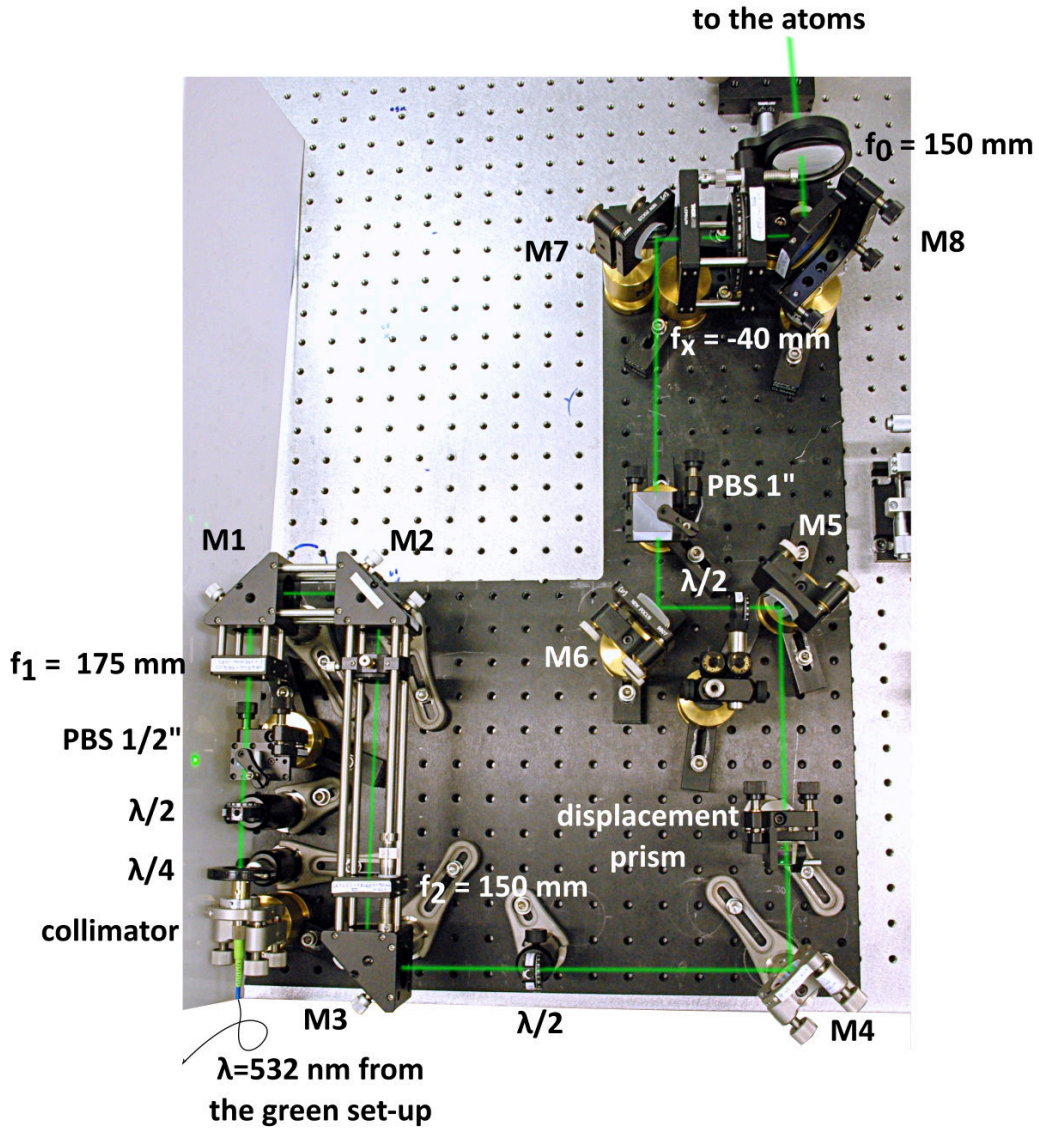

FIGURE 2.10: A photo of the optical lattice set-up after it has been assembled.

on a low drift mirror-mount (Polaris-K2S1) to the lateral polarizing displacement prism (LDP) (Lambda Research Optics, see Section 2.4.1), which splits the single incoming beam into two coherent parallel beams with orthogonal polarization: it reflects the s-wave polarization and transmits the p-wave one[4]. The distance between the two parallel beams is imposed by the dimensions of the prism. In order to have an interference when the beams intersect one another, after the LDP and on the path of the lower one, a $\lambda/2$ waveplate is placed to rotate the polarization of the p-wave prism output to the s-wave. The mirrors M5 and M6 are with the long axis vertically oriented in order to reflect both parallel beams at the same time. A high-power 1" polarizing beam splitter (PBS) (Thorlabs PBS25-532-HP) is necessary to clean the beams polarization after the LDP: it reflects s-wave and transmits p-wave polarization. Later on, the beams are reflected by the elliptical mirror M8 and enter into a plano-concave cylindrical lens (Optosigma CLB-2040-40NM) with a focal $f_y = -40$ mm and dimensions of 20×40 mm, which squeezes the light in the vertical direction producing two light blades, i.e two very anisotropic elliptic beams. (see Fig. 2.8) This lens is in telescope configuration with a 2" achromatic doublet (Optosigma DLB-50-150PM) with $f_0 = 150.7$ mm, which has a damage threshold of 35 W/mm. Between the cylindrical and the achromatic doublet, a dichroic mirror is placed, used in reflection for the green lattice and in transmission to transfer the light for the imaging that will be implemented once the set-up is added to the experimental apparatus. The cylindrical lens is glued on a cage plate and inserted in a support by which it can be precisely rotated. With a micrometer screw, it is possible to change the distance between the cylindrical lens and the achromatic doublet. We are able to control the rotational and translational degrees of freedom of the cylindrical lens, whereas the integrated tilting of the two beams is committed to the dichromatic mirror. To adjust the length of the telescope, the achromatic doublet is placed on a translational stage with standard micrometer (Thorlabs MT1/M). Furthermore, it is mounted in a Newport support (9852) to allow possible adjustments of the position of the intersection between the two beams. The support is sufficiently thin to be fixed in the small available space, though respecting the telescope configuration and the necessity to have the dichroic placed before the last lens, in order to let the light go through for the imaging.

2.5.1 Vertical set-up and imaging objective

We want to underline that the calculated in-plane frequencies are anti-confining (and therefore imaginary) because the green laser beam is blue-detuned with respect to the atomic transitions. To have an in-plane confinement, we have to compensate $\omega_{y,z}$ with additional fields ω_{add} that can be given by a magnetic field curvature or by red-detuned laser beams. The real radial frequencies will be given by $\omega_{R\,y,z} = \sqrt{\omega_{y,z}^2 + \omega_{add}^2}$. Using red-detuned beams, we can easily obtain $\omega_{y,z} \sim 20 \div 30$ Hz. An example of in-plane confinement with red-detuned beams can be found in the Ref. [34]. On the other hand, to realize uniform 2D gases we can use a homogenous blue-detuned potential tailored with a Digital Micromirror Device (DMD). In this case the compensation in the plane will be provided by a magnetic field curvature from the Feshbach coils, yielding a symmetric harmonic confinement with a frequency of about 8 Hz.

[4]The nomenclature s-wave and p-wave is referred to the incident surface of the prism face orthogonal to the beam direction.

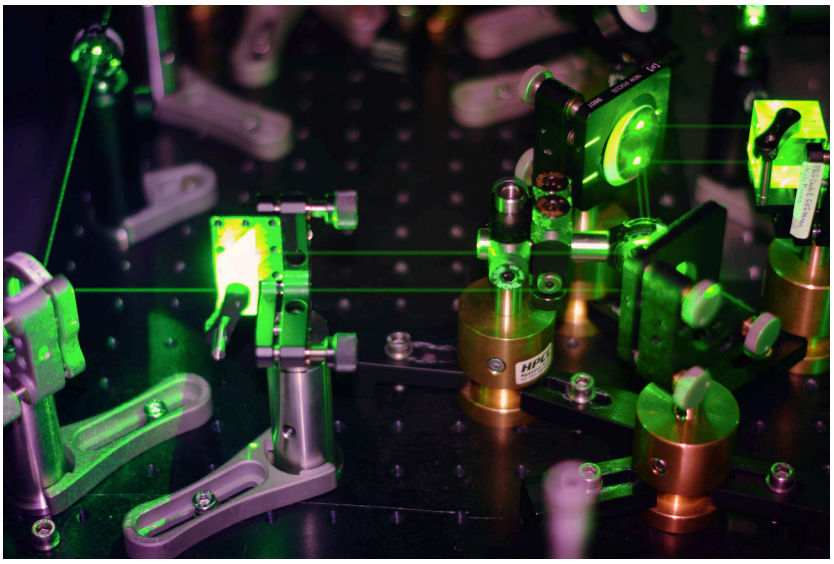

FIGURE 2.11: Photo of the lateral displacement PBS in the built lattice set-up. The incoming beam with a power of about 90 mW is splitted in two parallel beams with halved power, displaced from one another by 17.96 mm. In the photo, the parallelism of the split beams and the decrease of the light intensity are visible.

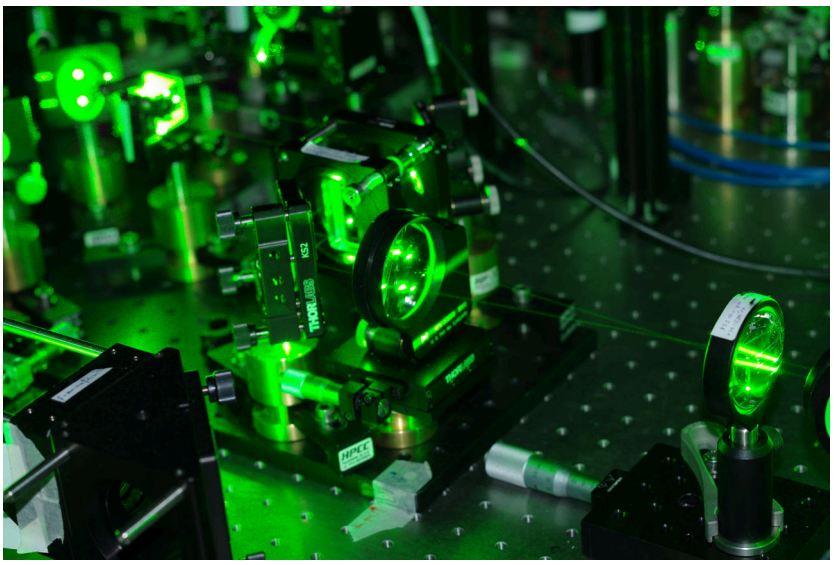

FIGURE 2.12: Photo of the focalization of the two beams after the achromatic doublet on a distance of 150 mm in the built lattice set-up. The point in which the beams intersect reciprocally is where the lattice interference pattern is formed.

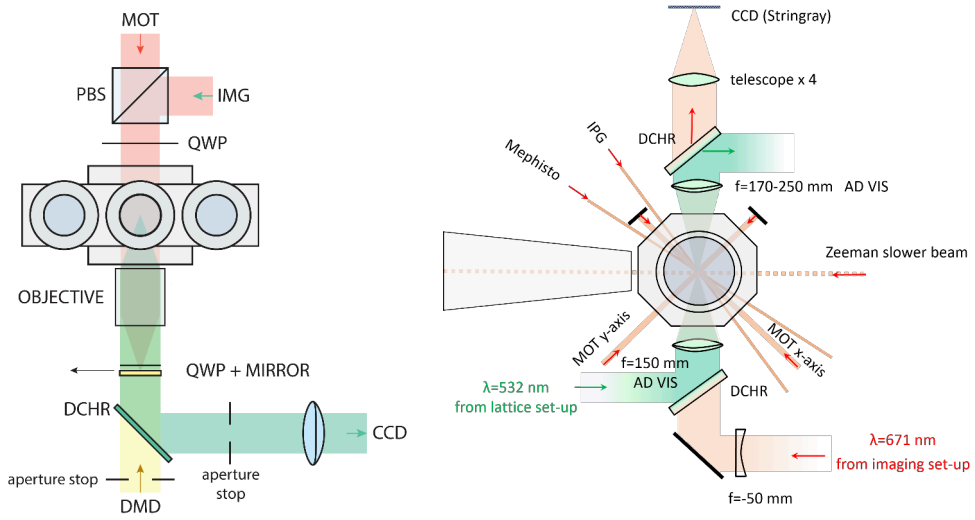

FIGURE 2.13: Vertical imaging set-up (on the left) and horizontal set-up for lateral imaging (on the right).

The scheme for the imaging of the quasi-2D atomic cloud in given in Fig. 2.13. It includes both horizontal and vertical imaging directions. To image the in-plane gas, a raw estimation of the resolution of the custom objective (Special Optics) that will be added to the setup can be done. By considering the diffraction limit of the objective, the dimension of the smallest observable spot is given by the Rayleigh formula of optical resolution [29]

$$R \simeq \frac{0.61\lambda}{NA} \tag{2.35}$$

where R is the radius of the Airy disc [29], λ is the wavelength of the imaging light and NA is the objective numerical aperture. The objective has a maximum a numerical aperture of $NA = 0.45$. The theoretical resolution at the imaging wavelength of $\lambda_{D2} = 671$ nm is then about $R \simeq 1.36 \cdot \lambda_{D2} \simeq 910$ nm. On the other hand, for the green beam with $\lambda = 532$ nm coming from the DMD, the objective yields a resolution of $R \simeq 1.36 \cdot \lambda = 724$ nm. In practice, one should consider also the finite size of the imaging beam and the imperfections of the optical elements in the path, and therefore testing the real achievable resolution is mandatory and will be done in the near future.

2.5.2 Towards an "optical accordion"

Between the 2" PBS and the mirror M7 there we have left some room to insert a supplementary optical device, in order to realize a so-called "optical-accordion". This is an experimental method to create optical lattices with real-time control of their periodicity. It provides a powerful tool for controlling ultracold atoms in optical lattices, where generally, small spacing is essential for quantum tunneling and large spacing enables convenient loading, single-site manipulation and spatially resolved detection. For our purposes, large-spacing lattice allows the loading into a single node and small spacing compresses the gas along the vertical direction making the quasi-2D confinement stronger.

This technique has been demonstrated optically in Ref. [30] and it was recently implemented on ultracold ^{87}Rb atoms in the experiment described in [32] by Ville

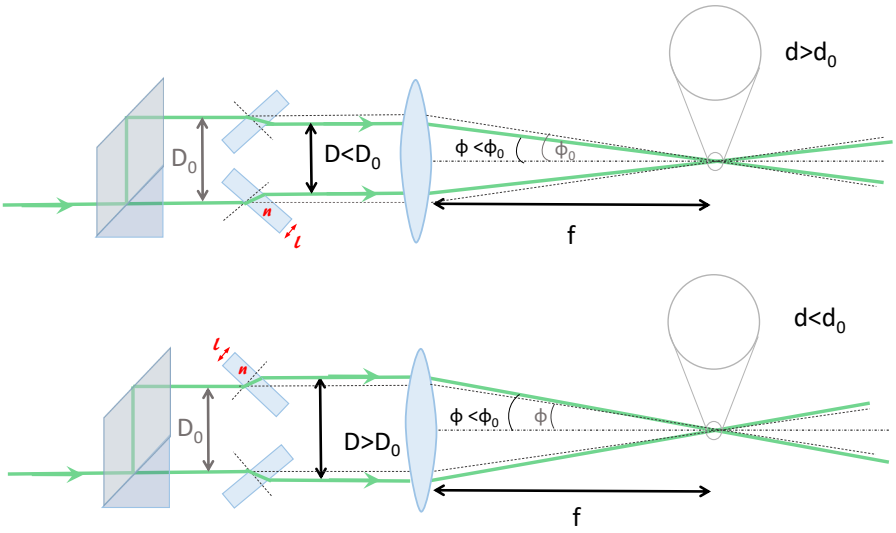

FIGURE 2.14: Sketch of the optical design allowing to change the angle between the two interfering beams.

et al. The article explains how the main challenge for realizing an accordion lattice is to avoid the displacements of the beams in the focal plane changing their angle. Indeed, a large displacement of the two beams decreases their overlap and leads to a lower lattice depth, and hence to a reduction of the trap frequency or even to atoms losses. The main limitations can be given by spherical aberrations or surface irregularities, and by the mechanical instability of the system. These limitations, important already for a static lattice, are much more severe for a dynamical tuning of the lattice spacing, and thus the realization of a stable static optical lattice with low aberrations is an optimal starting point for the further implementation into the system of an optical accordion. This will be implemented only if the loading in a single node will result too difficult.

Our idea for an accordion implementation is different from that proposed in [30] and used in [32], because our set-up is based on the idea of realizing a lattice with sufficient passive phase stability. By placing two pieces of glass with the same angle but opposite orientation from the optical axis, with care in the choice of the refraction index and the width of the substrate, the refracted beam will propagate with a certain displacement with respect to the incoming beam, as shown in Fig. 2.14. A motorized mount could be implemented to rotate these optical elements with continuity, achieving the dynamical adjustment of the lattice constant.

Chapter 3

Characterization of the crossed-beam 1D optical lattice

Realizing an optical lattice with precise and stable fringe positioning is a challenging task, as the interference pattern is very sensitive to individual beam pointing and to the relative phase between the two beams, requiring a careful alignment of the optical setup (see Section 3.1.1). After the realization of the optical lattice set-up, its optical performance has been tested (see Section 3.1) and the properties of the interference pattern have been measured (see Section 3.2). Moreover, optical aberrations caused by optical elements in the beam path may affect the smoothness of the potential. With a Shack-Hartmann wavefront sensor it has been possible to measure the aberrations of the overall system and test the transmission performance of the optical elements with respect the manufacturer specifications (see Section 3.1.2). To present the characterization of the realized optical lattice, after explaining the imaging method (see Section 3.2.1), I will first discuss the characterization of the single beam parameters (see Section 3.2.2) and then the measured lattice fringe spacing and contrast (see Section 3.2.3). From this measurements, I will give estimates of the expected trapping parameters (see Section 3.2.4).

3.1 Testing the optical lattice set-up

Before presenting the analysis of the lattice properties, we will discuss the procedure for the alignment of the optical setup and the characterization of optical aberrations.

3.1.1 Alignment procedure

For the alignment of the lattice set-up, all the optical elements are first adjusted at the same height in order to let the beams propagate parallel to the optical axis. The height of the optical axis has been chosen to create the lattice pattern at the correct height once the optical breadboard will be integrated into the main experimental apparatus, i.e. at the height of the atomic cloud over the mounting surface. Later on, small adjustments of the absolute and relative positions of the lattice beams are performed while imaging the magnified interference pattern via an imaging telescope (see Section 3.2.1).

In order to first collimate the beam propagating out of the fiber outcoupler, its waist is measured at different distances using a compact CMOS camera (Thorlabs DCC1545M), and the outcoupler lens position is adjusted to minimize the waist variation over a long distance (see Fig. 3.1). Subsequently, the telescope comprised of L1 and L2 is adjusted to re-collimate the beam while reducing its waist to $w \simeq 425\,\mu$m,

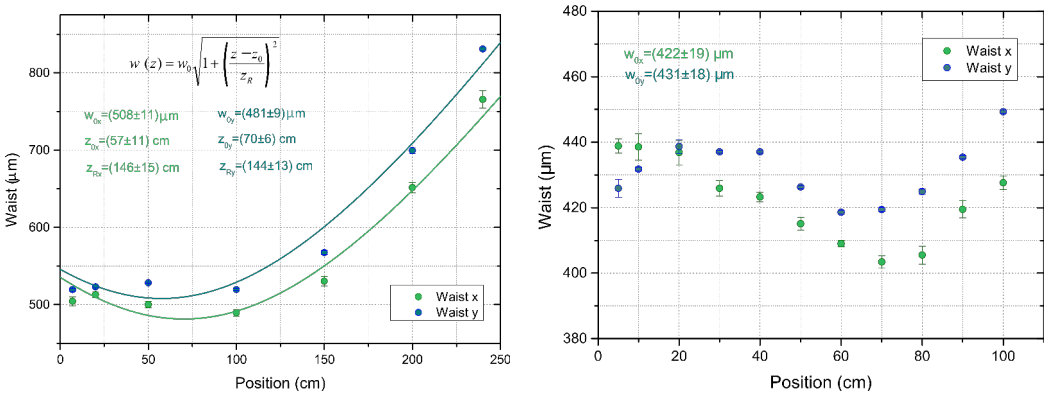

FIGURE 3.1: Measured beam waists along the horizontal y-direction and the vertical x-direction, during the construction of the set-up. On the left, the measured beam waists after the fiber outcoupler are shown over a distance of 2.5 m. The data are fitted using the Eq. (2.11). On the right, the beam waists measured after the lens L2 are shown over a distance of 1 m, after re-collimation by the telescope composed by L1 and L2.

corresponding to 3/4 of the original value (see Fig. 3.1). After this the beam propagates through the displacement prism where it is split in the two parallel beams (see Fig. 2.9). After traversing all elements, it reaches the last achromatic doublet lens.

To assure that the two beams have the same distance from the centre of the lens, such that they cross on the optical axis at the position of their respective foci, one can place a mirror in the intersection point of the two beams and align the beams so that each of them is reflected off the mirror and overlaps with their incoming counterpart. The mirror must be previously aligned to be orthogonal to the surface of the mounting breadboard. In order to carry out the alignment procedure, the beams are first set to propagate at constant height before inserting the cylindrical lens. The cylindrical lens is then placed, paying attention that its orientation matches that of the displacement prism: one must optimize the vertical alignment of the two outcoming elliptic beams and their shape, i.e. the orientation of each single ellipse.

Before placing the doublet lens, the retro-reflecting mirror is added and adjusted to reflect the two parallel elliptic beams over themselves, assuring therefore that its surface is oriented perpendicular to the optical axis. At this stage, the achromatic doublet lens is added in telescope configuration with the cylindrical lens at about 11 cm. The beams reflected off the additional mirror are aligned, through vertical translation and tilt of the doublet lens, to overlap with the incoming beams over a distance of more than 30 cm, by checking their spots on different surfaces, e.g. M6 and M7. The retro-reflecting mirror position along the optical axis can be precisely set by checking that the reflected beams propagate at the same mutual distance than that of the incoming ones. Finally, the collimation of the beams in the horizontal direction after the doublet lens is checked and adjusted by precisely varying the position of the cylindrical lens.

3.1.2 Study of the aberrations with a wavefront-sensor

The wavefront of a laser beam is nothing else that the the surface of points in space which have equal phase. Often, to aid in the interpretation of optical test results, the wavefront is expressed in polynomial form. The decomposition in Zernike polynomials allow for a quantitative representation of each kind of aberrations of an optical system, since each Zernike coefficient is directly related to a particular type of aberration observed in optical tests [35]. The coefficients of the Zernike polynomials are

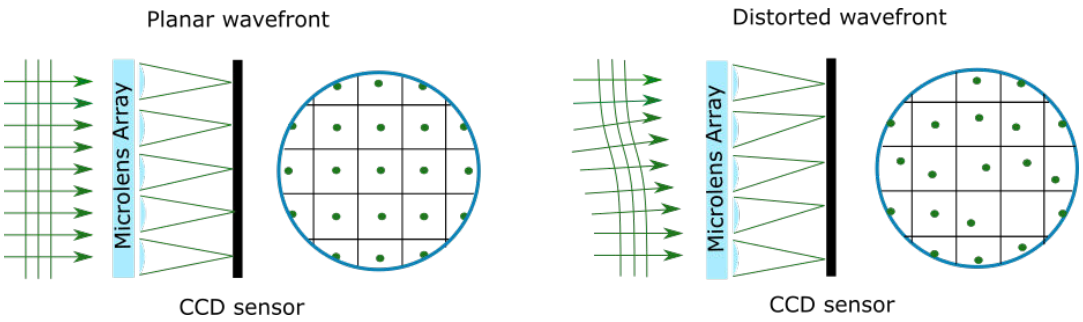

FIGURE 3.2: Outline of the working principle of a Shack-Hartmann wavefront sensor.

determined by a least square fit of the measured wavefront, and the Zernike modes are normalized to have unit variance.. An optical system is considered to have acceptable aberrations if the Zernike coefficients are sufficiently small for the mean root square of the errors to be less then $\lambda/4$. This means that in our set-up the RMS value should to be less than 133 nm.

To measure the wavefront aberrations of the lattice optical system, I used a Shack-Hartmann wavefront sensor (Thorlabs WFS150-5C) [36]. This device is composed by a microlens array and a CCD sensor, as shown in Fig. 3.2. The working principle of this device is is the following. Each microlens of the lenslet array collects the light incident on its aperture and generates a single spot on the detector plane, that is located at a distance of one focal length behind the lenslet. Each spot is centered behind the corresponding lenslet only if the incident wavefront is planar and parallel to the plane of the lenslet. Depending on the distortion of the wavefront incident on the sensor, the spot position will be shifted along x and y directions away from the z axis of its associated microlens.

Typical measurements of the aberrations of a single laser beam propagating through the set-up, acquired with the wavefront sensor placed after the achromatic doublet, are shown in Fig. 3.4. The interest of this test is to assess the quality of the optical elements discussed in the previous Chapter, and in particular that the cylindrical lens does not excessively deform the wavefront of the laser. This is crucial to quantify undesired deformations of the potential with respect to its ideal shape, which lead to detrimental effects during and after the loading of atoms into the trap. I placed the WFS in different position along the path of the laser beam after the achromatic doublet. The alignment of the sensor is very critical, and the WFS is thus mounted on a support that can be horizontally and vertically tilted to set the surface of the sensor in perpendicular orientation to the direction of propagation of the laser beam. The wavefront analysis can be verified in real-time thanks to WFS software, checking that the spot-field and the beam view are centered into the viewfinder, and that the elliptic beam wavefront has a semi-cylindrical shape[1], as expected. The irregularities in the measured wavefront for a beam passing about 0.6 cm below the optical axis of the achromatic doublet increase with the distance from the doublet itself, as shown in Table 3.1. They are included between $(200 \div 400)$ nm. Examples of wavefront analysis are given in figure 3.4. We have to take into account that the atoms will be placed at about 15 cm from the lens, i.e. the distance over which the lattice beams are focalized and intersect. The vertical size of the beam in the focus is about 60 μm, which is unfortunately too small for allowing a direct reconstruction of the wavefront surface using the WFS. However, the trend of the wavefront errors measured at varying distance from the achromatic doublet suggests that the wavefront

[1] Also the projection in the $x - y$ plane can help the alignment procedure.

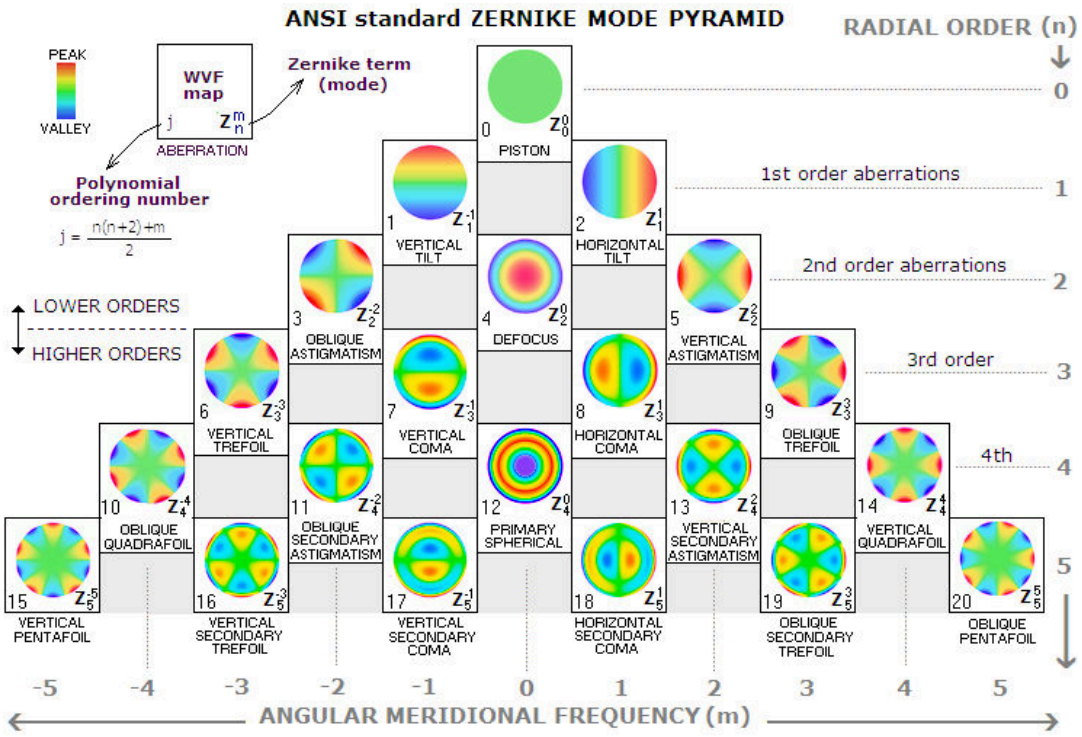

FIGURE 3.3: Pyramidal table of Zernicke polynomial coefficients.

Position [cm]	Peak To Valley [μm]
40	0.201
70	0.209
100	0.277
140	0.397

TABLE 3.1: Peak-to-valley magnitude of the maximum deviation for the observed wavefronts at different positions after the doublet lens.

error in the focus should be well below 200 nm.

We can also look in detail at which type of aberrations dominate the wavefront error, computing the Zernicke coefficients of the wavefront. This was done both for a beam centered on the doublet lens and for a beam that crosses the lens below its center by about 0.6 cm (see Fig. 3.5). The coefficients with significant values are astigmatism $0/90^\circ$ and defocus. Both are expected in our system due to the different curvatures of the beam profile in the two directions and to the fact that we are not probing the beam in the focal plane of the lens doublet. All other Zernicke coefficients are insignifcant, and we conclude therefore that the off-axis performance of the lens is sufficiently good.

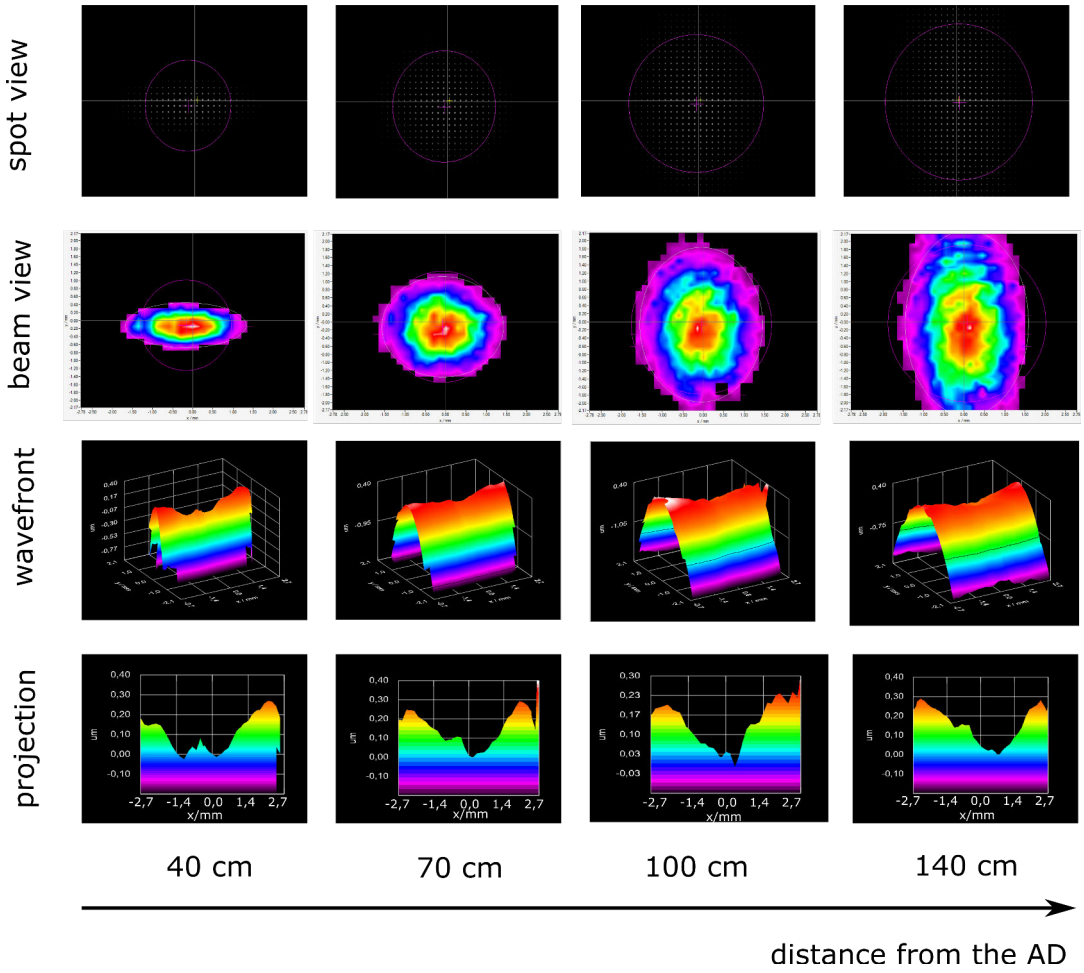

FIGURE 3.4: Images of the single beam off centred of 0.6 mm by the center of the lens taken at different distances from the achromatic doublet. Comparison between the spot view detected by the sensor and the reconstructed beam view and wavefront. The bottom row of images show the projection of the wavefront on the x-z plane (see coordinate definition in figure 3.5, on the right).

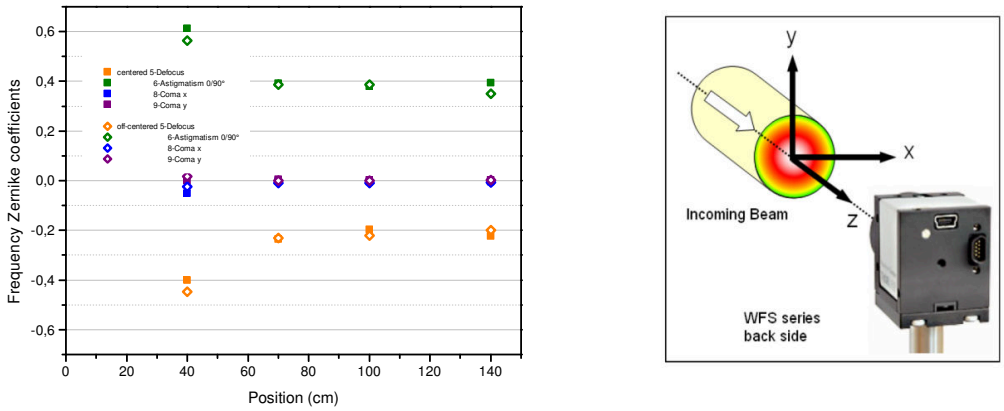

FIGURE 3.5: On the left, the value of some relevant Zernike coefficients are plotted, i.e. defocus, astigmatism and coma, as a function of the distance from the achromatic doublet, for incoming beams centered and off-centered by 0.6 mm from the optical axis of the achromatic doublet. On the right, the image shows the definition of the coordinate system for the wavefront sensor and is taken from [36].

3.2 Characterization of the optical lattice pattern

To evaluate all parameters that are relevant for the confinement of the atoms in the optical lattice trap, the intensity distribution of the lattice beams in the intersection point has been characterized. The lattice pattern created by focusing independent beams through a lens has the advantage that it can be directly detected by imaging it on a sensor, unlike retro-reflected lattices in which a direct detection of the interference fringes is not possible. From the measurement of the intensity distribution in the crossing point, we obtain:

- the waists of each single elliptical beam w_{0x},w_{0y};
- the potential radius $\tilde{w}_x$, given by the envelope size in the intersection of the beams;
- the lattice spacing d of the pattern interference.

The most relevant parameters of the potential that can then be calculated are the trapping frequencies, defined in Eq. 2.26, and the trap depth of the central lattice fringe $T_0 = 4U_0/k_B$, where U_0 is the trap depth associated with the intensity of a single lattice beam.

3.2.1 Imaging method

The lattice intensity distribution in the crossing point is imaged on a CMOS camera (Thorlabs DCC1545M [37]), with a pixel size of 5.2 μm. The camera is placed at a distance from the doublet lens equal to its focal length of about 15 cm. A translational stage with a micrometric actuator allows to explore a range of $\pm$ 1.25 cm with high precision and allows to find the exact position of the beam intersection. This simple setting has been used to measure the waists of the single beams and the Gaussian envelope of the interference pattern in the crossing position. On the other hand, in order to resolve the interference pattern, a $\times 10$ telescope has been placed after the achromatic doublet, composed by two spherical lenses with focal lengths of $f = 50$ mm and $f = 500$ mm. The real coefficient of magnification of this telescope is calibrated using the ratio between the waist of the single beams measured in the real focus and in the magnified one. The calibrated magnification is then used to extract the actual lattice spacing from the interference pattern.

In the focus of the achromatic doublet, I recorded images for different camera positions around the focus, for each single beam and for their interference pattern. After summing over all rows or columns of the image, I performed fits of the intensity distribution to extract the beam and/or interference pattern parameters. For the single elliptic beams the fitting functions in the x- and y-directions are given by

$$I(x) = b_x + a_x\, e^{\frac{-2(x-x_0)^2}{w_{0x}^2}}, I(x) = b_y + a_y\, e^{\frac{-2(y-y_0)^2}{w_{0y}^2}}, \tag{3.1}$$

where b_x (b_y) is the background intensity, x_0 (y_0) is the coordinate of beam center position, and $w_{0\,x}$ ($w_{0\,x}$) is the waist along the x (y) direction. For the interference pattern, which is always integrated along the y-direction before fitting, the following function is instead used:

$$I(x) = b + a_x\, e^{\frac{-2(x-x_0)^2}{\tilde{w}_x^2}} \cos^2\left(\frac{\pi x}{d} + \Phi\right) \tag{3.2}$$

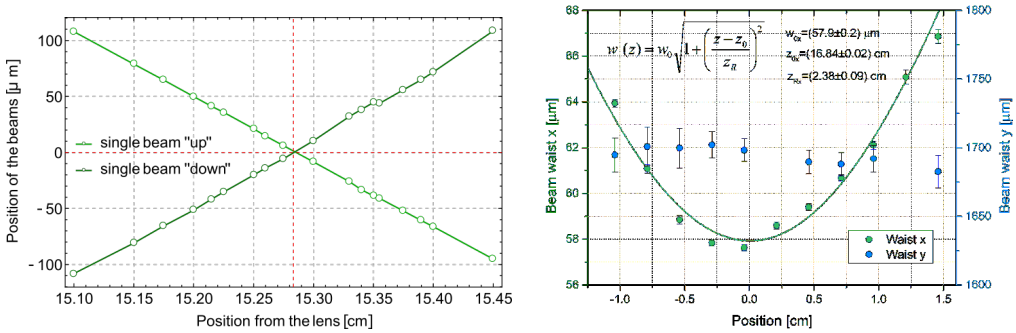

FIGURE 3.6: On the left, position of the beams near the focus after after the achromatic doublet. On the right, measured beam waists along the horizontal y-direction and the vertical x-direction.

where b is the background intensity, x_0 is the center position of the interference Gaussian envelope, $\tilde{w}_x$ is the potential radii, d is the lattice spacing, and Φ is the lattice phase in radiant units[2].

3.2.2 Single-beam analysis

From the analysis of the single elliptic beam intensity, using the fitting function in Eq. (3.1), the position of the beam in the vertical direction x_0 for both beams can be extracted, obtaining the position of their intersection, as shown in figure 3.6. The focalization of each beam in a region around the expected Rayleigh range $z_{R,x}$ is then checked around the crossing point by extracting the beam waists as a function of the position. The waists measured at different positions are shown in Fig. 3.6, and the values extracted from the fitting functions are

$$w_{0x} = (57.9 \pm 0.2)\mu m \quad \text{and} \quad w_{0y} = (1694 \pm 6)\mu m. \tag{3.3}$$

The two beams have therefore the required amount of ellipticity, as explained in the context of the desired lattice properties in order to obtain adequate trapping frequencies in the vertical x-direction (see Section 2.3).

3.2.3 Lattice pattern properties

To detect the lattice pattern, images are recorded at the location of the beam intersection magnified by a $\times 10$ telescope, as mentioned earlier. The intersection position was chosen as the location where the Gaussian envelope amplitude was maximum. In order to optimize the interference fringe contrast, I followed the following strategy. I first optimized the fringe contrast by placing the camera in a location where the beams are not fully overlapped,and balancing the relative intensity between the two beams at the output of the lateral displacement prism. This can be done by acting on the half-waveplate placed just before the lateral displacement prism. The balancing has also been checked by measuring the two beam powers with a power meter at the output of the cleaning PBS after the lateral displacement prism. Moreover, I verified that the the beam polarizations before the achromatic doublet lens were identical. such that interference is maximized. This feature is characterized by a gradual decreasing or increasing the intensity of the lower between the two beams.

[2]The phase of the lattice pattern, and in particular its stability over time, will be discussed in Chapter 4.

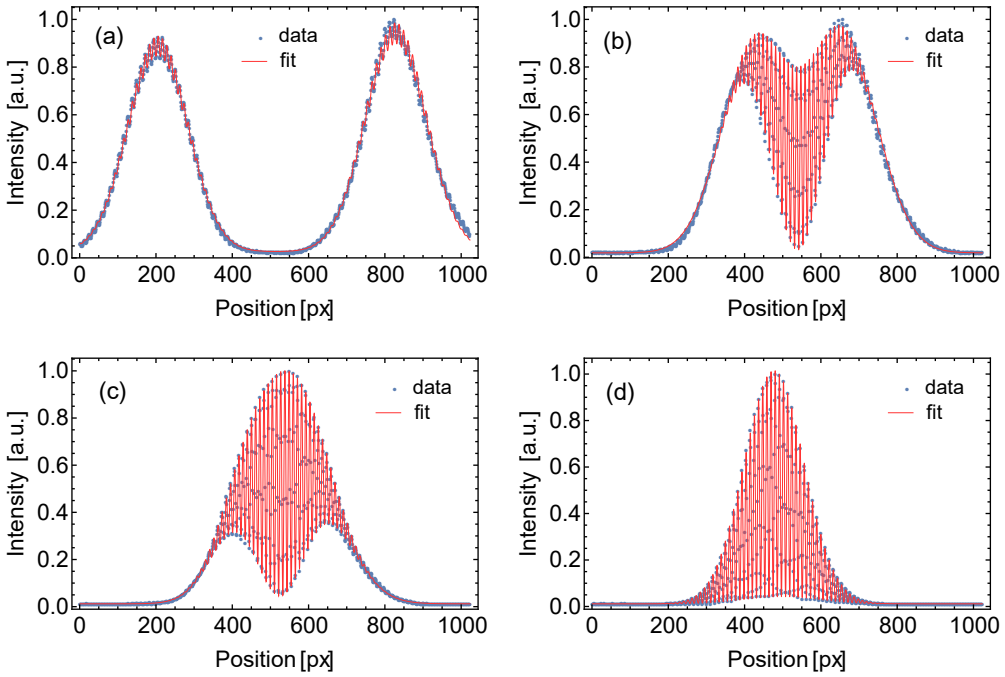

FIGURE 3.7: Sequence of images of the interference pattern moving the camera along the path of the two beams. In this example the superposition between them is maximized.

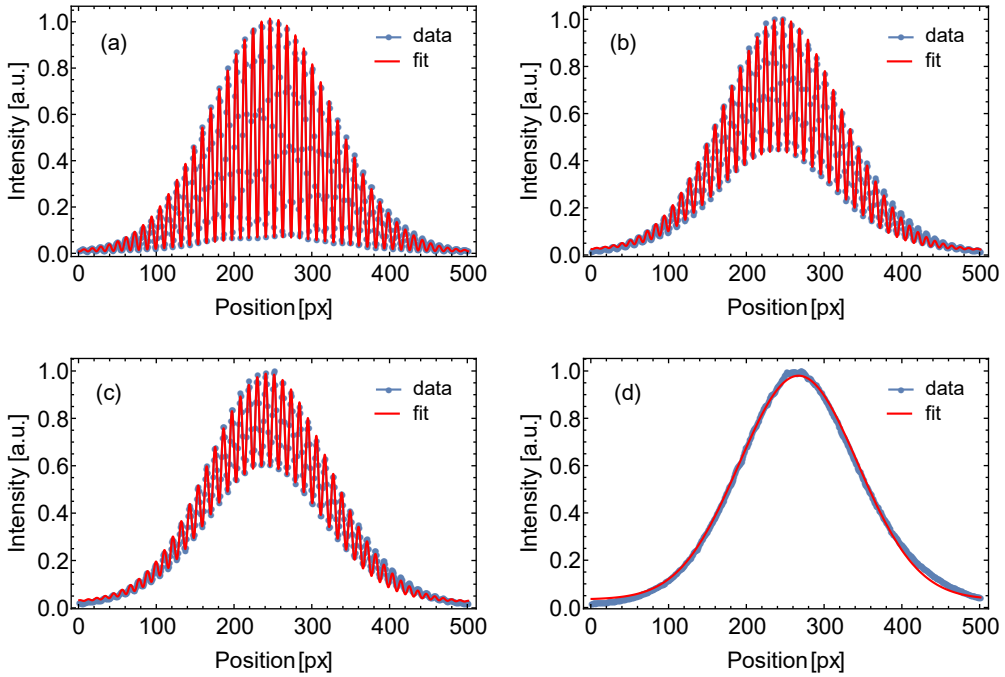

FIGURE 3.8: Sequence of images of the interference pattern obtained by varying the balance between the polarization of the beams, i.e. for different choice of the phase-contrast between the fringes.

ν_x [kHz]	ν_y [i Hz]	ν_z [i Hz]	T [μK]	T_F [nK]	$R_{F,\,x}$ [nm]
7.5 ± 0.2	8.8 ± 0.7	15.5 ± 0.3	1.60 ± 0.01	79 ± 4	314 ± 15

TABLE 3.2: Lattice properties for the measured value of the beam waist $w_{0x} = (1694 \pm 6)\mu$m and $w_{0y} = (57.9 \pm 0.2)\mu$ and $P_0 = 1$ W. For the calculation of T_F and $R_{F,\,x}$, a typical number of atoms $N = 10^4$ is considered.

If the superposition between the beams is maximum, along the path of the beam after the telescope the shape of the two beams along their trajectory is like that shown in Fig. 3.7, i.e. the heigth of the two peaks is the same and in the focus the phase contrast is maximum. Then, in the focus I checked that after these steps, the phase contrast between the fringes was maximum. This corresponds to the the absence of a Gaussian background on the bottom of the interference pattern. Changing the balancing of the relative power between the two beams at the entrance of the lateral displacement prism produces, in the focus, the sequence of images given in figure 3.8.

A typical image at the center of the optical potential is given in figure 3.9 with its relative integration along the vertical direction. Additionally to the horizontal fringes of the interference pattern we can see inhomogeneities along the fringes. In fact, despite we had care to take the measurements with CMOS without the additional glass window, there are some internal reflection between the filters outside the camera. Measuring the single beam waists in the magnified focus for both beams, we get a mean value of $w_{0x}^M = (770 \pm 3)\ \mu$m. Dividing it by the measured waist w_{0x} given above, we get the magnification coefficient

$$M = \frac{w_{0x}^M}{w_{0x}} = 13.3 \pm 0.1. \tag{3.4}$$

With this value, we can obtain the real lattice spacing multiplying the value extracted from the fit with $(pixelsize/M)$. Thus, I get

$$d = (4.26 \pm 0.02)\mu m \tag{3.5}$$

Pleasantly, this value agrees with the theoretical value of 4.44 μm showed in table 2.1. It was that expected from the Abbe sine condition for beams with $\lambda = 532$ nm, crossing a lens of focal length $f = 150$ mm at a mutual distance of 17.96 mm. Figure **??** shows a comparison in the central region of the interference between the theoretically expected pattern, calculated by setting the measured values of the beam waists (see Section 3.2.2), and the measured profile: the two patterns show very good agreement. Using the function of fit in Eq. 3.2, moreover, I get a value of the potential radius

$$\tilde{w}_x = (56.8 \pm 0.3)\mu\text{m}. \tag{3.6}$$

3.2.4 Expected trapping frequency

The measured waists, with a power $P_0 = 1$ W for the beams, lead to the expected trapping frequencies given in Table 3.2.

These frequencies are close to the desired properties for the trapping potential, discussed in the Section 2.3. An axial frequency of 7.5 kHz provides, for the readily

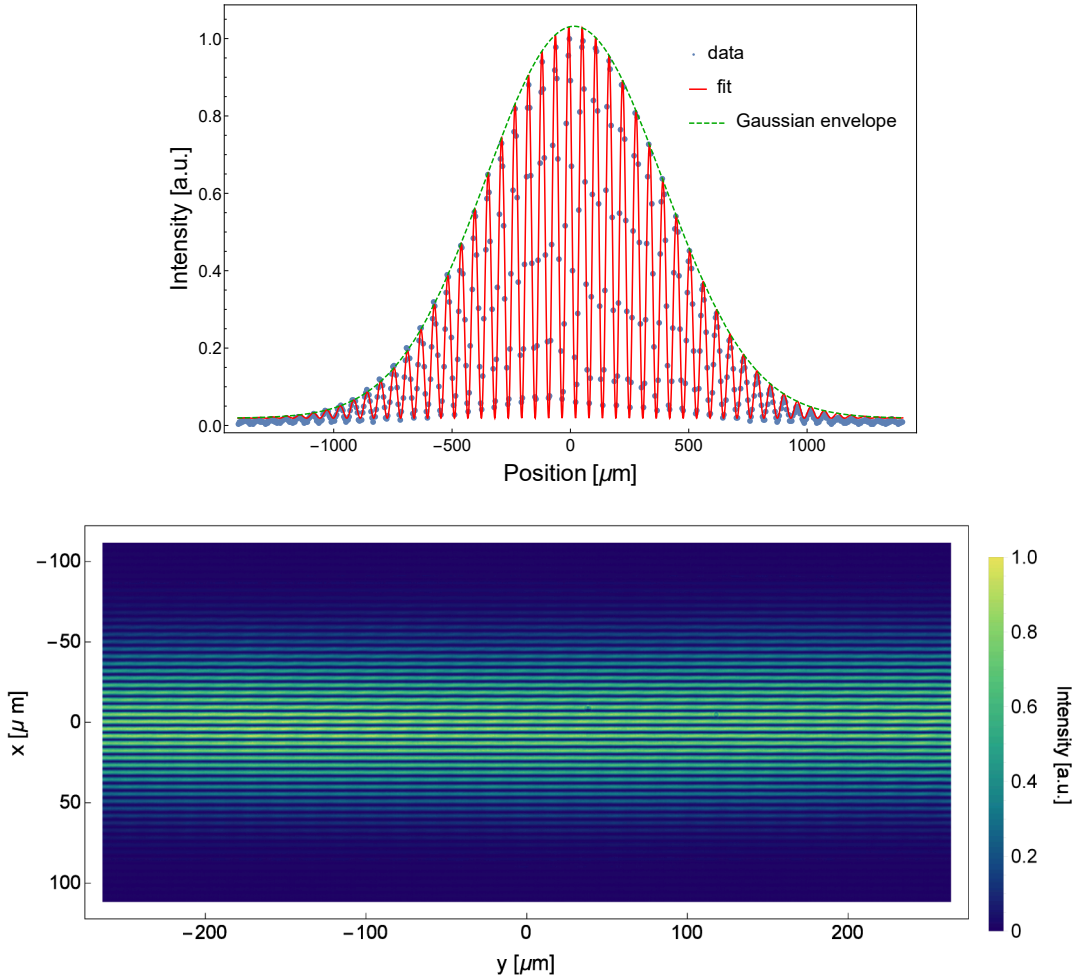

FIGURE 3.9: On the top, an example of the data extracted from the images taken in the magnified focus. In blue, the data, in red, the fit function 3.2, in green, the Gaussian envelope are shown. The interference contrast is maximized and the width of the potential radius is minimum, meaning that the two beams intersect precisely in their respective foci. The potential radius is consistent with the value of the beam waist. On the bottom, an image of the 1D lattice pattern taken at the center of the Gaussian envelope.

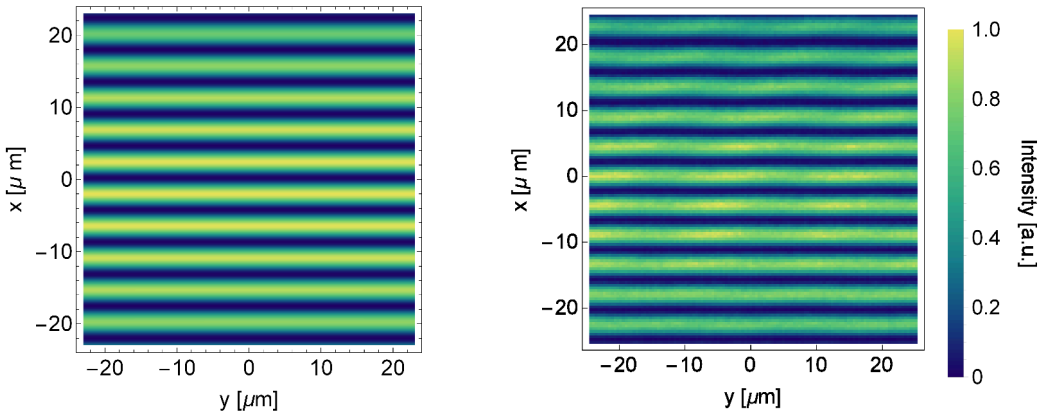

FIGURE 3.10: Comparison between the lattice patterns taken through the center of the Gaussian envelope. (Left) Calculated (once measured the beam waists in Section 3.2.2). (Right) Measured.

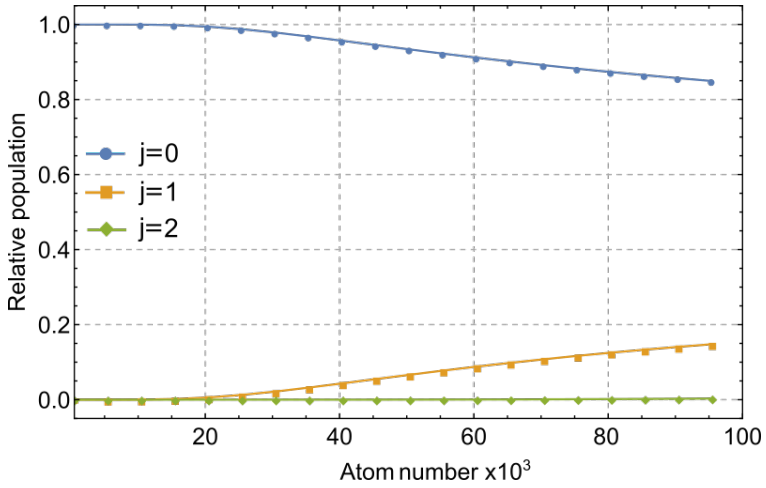

FIGURE 3.11: Relative population of a cloud of $N = 2.5 \cdot 10^4$ ^{6}Li atoms in the first three levels of an harmonic potential of quasi-2D potential with a frequency of $\omega_x = 2\pi \cdot 7.5$ kHz.The adiabatic compression of the cloud, has been computed for an initial T/T_F=0.1 and a dipole trap with frequencies 21 Hz, 245 Hz, 215 Hz.

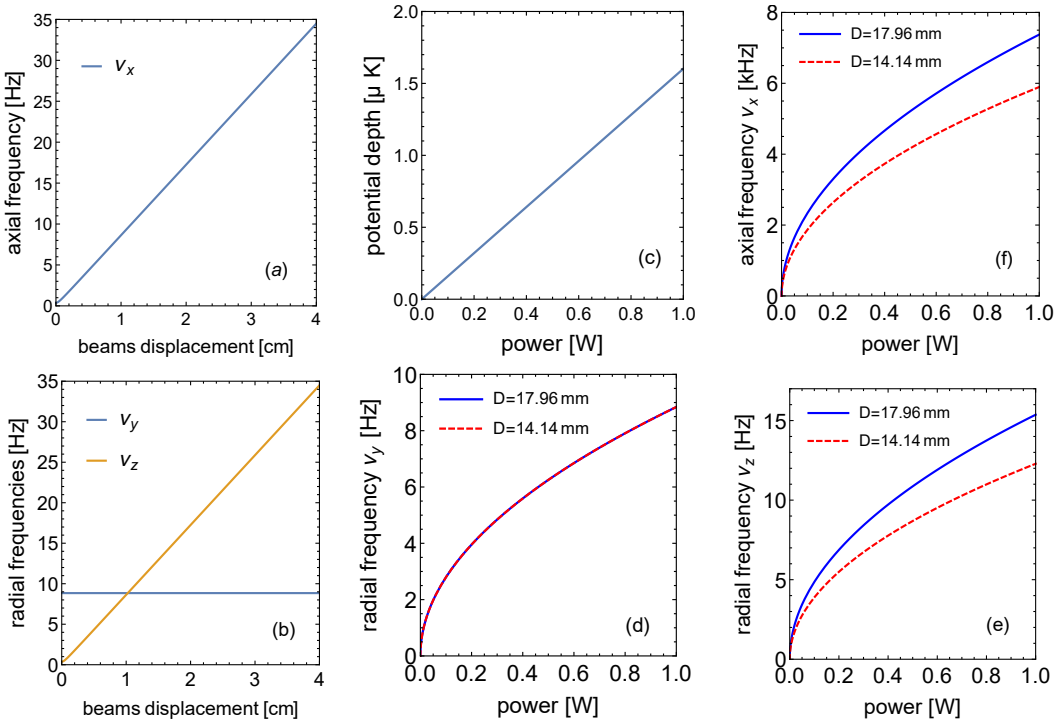

FIGURE 3.12: Summary of the expected trapping frequencies for the measured waists in Section 3.2.2 as a function of the displacement with $P = 1$ W (a)-(b) and power (d)-(f) of the beams. In (c) the resulting potential depth as a function of the power of the laser.

available laser power of 1 W, a total trap depth larger than 1 μK and a Fermi temperature of about 80 nK with $N = 10^4$, that satisfy the condition for the quasi-2D confinement1.18, showing $\epsilon_F < 0.2\hbar\omega_x$. On the other hand, the radial frequencies, despite their asymmetry, are on a scale that can be reasonably compensated with additional laser beam (preferably, slightly elliptic too). More precisely, we can look at the simulations developed in the framework of the adiabatic lattice transfer in Section 1.2.2. We can observe from the plot in Fig. 1.4 (number of occupation of the harmonic oscillator levels as a function of the axial frequency of the trap), that for a frequency of 7.5 kHz the first exited state is empty and so the degree of freedom of the atoms is freezed at the ground states. The atoms cannot access to other energy levels in the x-direction. Moreover, starting from that simulation, we can obtain information on how, for $\omega_x = 2\pi \cdot 7.5$ kHz and an initial temperature $T/T_F = 0.1$, the 2D condition depends on the number of atoms loaded in the trap. The result of this simulation is shown in Fig. 3.11. In particular, fixing the radial frequencies, we observe that the lower the initial number of atoms, the more easily the condition of quasi-2D confinement is achieved. The critical atom number is around $2 \cdot 10^4$.

Finally, in Fig. 3.12 are plotted some relations discussed before in the Section 2.3, calculated for the measured waists reported in Section 3.2.2. In particular they summarize the trapping frequencies fixing the power $P = 1$ W and changing the displacement D between the beams (a)-(b), and vice versa fixing D and changing the beam power (d)-(f). In particular, the graphics (a) and (b) show, for example, the possibility to change the frequency by creating an optical accordion (as suggested in 2.5.2). In (d)-(f) are calculated the frequencies for the two values of displacement allowed by our prisms: for the bigger one, that is mounted in the set-up, (blue curves) and for the smaller one (red dashed-curves). Changing the power by 1 W is possible to adjust the trapping frequencies in the axial direction (e) decreasing their value from a maximum of 7.5 kHz. The frequency range spanned can indicatively allow to study different tunneling rate between the layers (see Fig.2.4). In (c) is shown the potential depth as a function of the power of the laser: changing the power of the laser modifies both potential depth and trap frequencies.

Chapter 4

Experimental characterization of lattice stability

A main technical challenge for the realization of an optical lattice trap regards the stability of the interference pattern. To guarantee reproducibility, one needs to prepare the system under the same conditions. Any change in the relative phase of the lattice beams will lead to a global movement of the potential that may disturb the atoms in the lattice. On long timescales, slow drifts in the phase of the lattice may limit the reproducibility of subsequent experimental runs. On the other hand, on short-timescales phase stability is desired to avoid heating of the atoms in the lattice change as well as to ensure that the shape of the optical potential does not during one single experimental run.

The attainment of long lifetimes of the trapped samples imposes stringent requirements not only on the phase stability of the lattice but also on the intensity and pointing stability of the laser. If the frequency of these fluctuations coincides with the trap frequency, this leads to heating of the trapped sample.To estimate the effect of such noise-induced heating, it is necessary to characterize the noise spectrum of the laser.

This chapter is divided in three sections dedicated respectively to phase measurement stability on different timescales (see Section 4.1), noise spectrum characterization for both intensity and fringes fluctuations (see Section 4.2) and laser-induced heating rates (see Section 4.3). In the Section 4.1, after discussing how to stabilize the laser polarization (see Subsection 4.1.1), I discuss phase measurements (see Subsection 4.1.2) looking at the correlation between phase lattice and beam position (see Subsection 4.1.2). Moreover I take into account temperature influence on long-term time measurements (see Subsection 4.1.4) and mechanical vibrations on short-term (see Subsection 4.1.5). In Section 4.3, I present the noise detection set-up (see Subsection 4.2.1) and the procedure for an intensity stabilization (see Subsection 4.2.2). The characterization of the noise spectra is functional to calculate the typical timescale related to heating rates. This topic is presented in Subsections 4.3.1 and 4.3.2.

4.1 Phase stability

The phase stability of the interference pattern can be affected by temperature changes and air drafts or mechanical vibrations. To study how the interference pattern changes in time I monitored its stability using a CMOS camera (Thorlabs DCC1545M) with a pixel size of 5.2 μm. To observe the interference pattern and its movements with high resolution, I set up a x10 telescope to magnify the fringes on the camera (for details see chapter 3). All the measurements are taken on air-floated table, with the room illumination switched off. The Thorlabs software allows to set a measurement

number of images n	interval Δt [s]	rate	time [s]		time scale
100	1	1 image/1 s	100	1 min 40 s	∼minutes
	10	1 image/10 s	1000	17 min	
	60	1 image/1 minute	6000	1 h 40 min	∼hours
	100	1 image/100 s	10000	2 h 45 min	
120	300	1 image/5 minutes	36000	10 h	∼daytime

TABLE 4.1: Settings chosen to measure the stability of the interference pattern along different time-scale.

by fixing the number of images n and the time delay Δt between one another. The chosen settings are showed in Table 4.1.

The strategy to test the stability of the set-up is to monitor the interference pattern at the beam crossing as a function of time over different timescales, ranging from several seconds to several hours and its reaction to different disturbances. On long timescales, it is possible to characterize the effects of the temperature on the phase stability (see Subsection 4.1.4). Slow drifts can limit the reproducibility of a given potential in subsequent experimental runs. On the other hand, on short-timescale air movements and optical elements vibrations are relevant (see Subsection 4.1.5). Fast fluctuations can modify the shape of the optical potential during one single experimental run and heat the atoms in the traps leading to their loss[1].

The relevant parameters of the lattice are extracted from the images with 1D fits to the intensity distribution which was integrated along one axis over the central region of the image that is chosen with the same size for all the images.The fit function is given by:

$$I(y) = b + a_y \, e^{\frac{-2(y-y_0)^2}{s_{0y}^2}} \cos^2\left(k_L y + \pi\phi\right) \tag{4.1}$$

where b is the background intensity, y_0 is the position of the beam pointing into the frame of the image cut out, s_{0y} is the potential radii, k_L is the the wave vector of the lattice and ϕ is the lattice phase in unit of π. The phase change of one corresponds to a movement by one lattice constant of the interference pattern. The change of the fitted phase over time quantifies the drift of the interference pattern.

4.1.1 Alignment of polarization in the optical fiber

In order to avoid intensity fluctuations of the laser due to temperature variations, the polarization of the light is aligned with one of the birefringent axes of the optical fiber. Refractive indexes of the optical fiber depend on the temperature and, as a consequence, the polarization of the output beam changes. In this way, also little changes in temperature can lead to a substantial variation of the intensity distribution outcoming from the PBS placed after the collimator. An example is shown in Fig. 4.1. For a temperature variation of about 1 °C, if the polarization is well-aligned and stable, the intensity fluctuates on about ±3%, otherwise, it is about ±60%. To stabilize the polarization of the light we have used a Polarization Analyzer (Shaefter-Kirchhoff SK010PA-VIS 450-800 nm) that maps the states of polarization of

[1]This aspect will be studied in the Section 4.2.

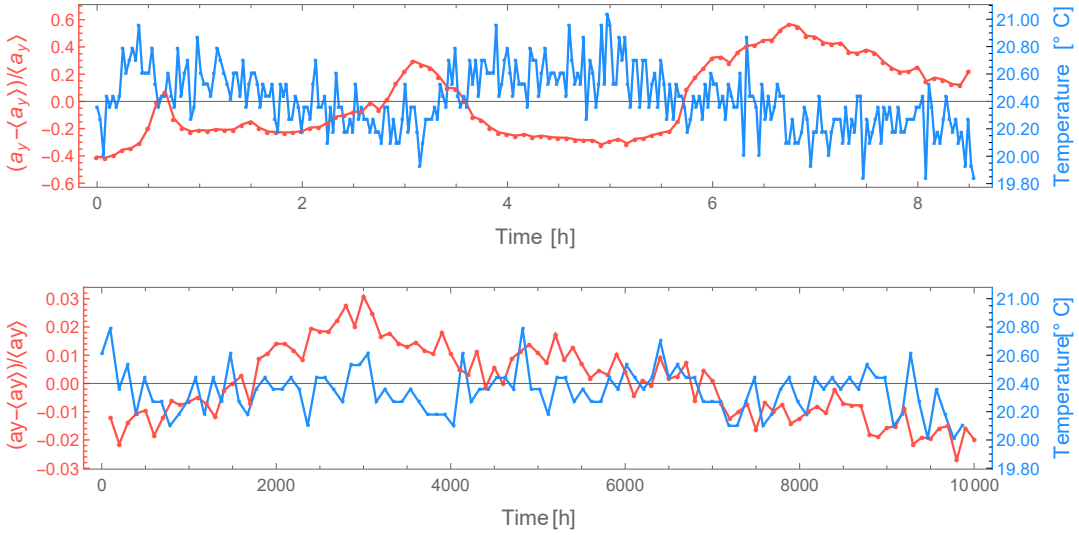

FIGURE 4.1: Relative fluctuations of the laser intensity during long-term measurements and ambient temperature: examples of measurements taken before (up) and after (down) the alignment procedure for the laser polarization into the optical fiber.

Wavelength	λ [nm]	532
Mean Ellipticity	η [°]:	24.007
	$\Delta\eta$ [°]:	0.076
Azimuth	Φ [°]:	-72.579
Mean Extinction	PER [dB]:	7.025
Min. Extinction	PER [dB]:	6.995
Min. Extinction Ratio	V [dB]:	1:5

TABLE 4.2: Properties of the laser polarization, once matched with the fiber, at the output of the collimator in the lattice set-up.

monochromatic light on the Poincarè sphere [38]. This allows to search the condition for which the polarization change due to a given perturbation is minimazed. To obtain this condition we have to optimize the polarization of the beam-input in the fiber. The result of this procedure is shown in in table 4.2 and corresponds to have an elliptic polarization at the output of the collimator in the lattice set-up. Accordingly, in front of the collimator is placed a $\lambda/4$ waveplate, which changes the polarization from elliptical to linear in order to maximize the available power in the realization of the optical lattice.

4.1.2 Measurement of the lattice phase

The phase extracted from the fits using Eq. (4.1) are compared with their mean values and the phase deviation is plotted as a function of the time, as shown in Fig. 4.2. The measurements shown in this figure are taken in the best experimental conditions achieved: illumination and air conditioned switched off, set-up covered with a lid and laser polarization stabilized. The measurements taken without these precautions, show increasing distructive effect of fluctuations in the phase stability of the pattern interference. In these conditions, shot-to-shot fluctuations are taken

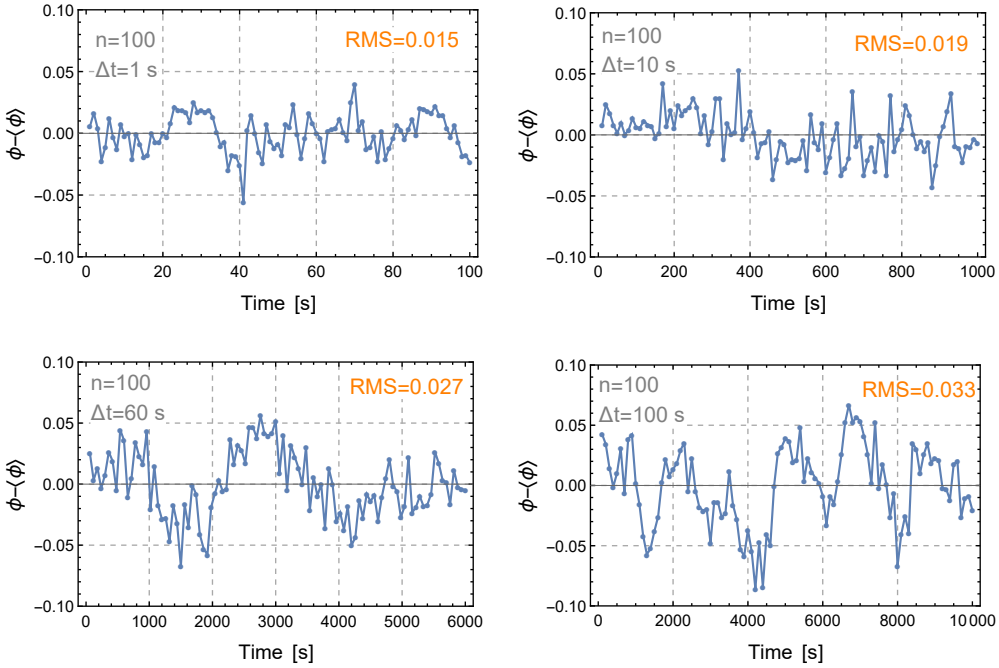

FIGURE 4.2: Short and long-term phase stability measurements in the best achieved experimental condition: laser stabilized in polarization, suspended table, covered set-up, absence of air draft in the room.

with steps of one, ten, sixty and one-hundred seconds, and an average of $(0.01 \div 0.02)\ \pi$ is detected. Shot-to-shot variations increase if the lattice set-up is perturbed mechanically(see for details Subsection 4.1.5) or by the increasing of the time delay, as for example, in the measurement of eight hours long shown in Fig. 4.6, where shot-to-shot fluctuations are taken on five minutes intervals is at most 0.04 π.

On minutes timescale (100 and 1000 seconds), collections of data on entire measurements show fast fluctuations around zero with an RMS value associated of about 0.02 π. This means that, on average, the lattice position fluctuates in a range of about 0.6 μm. The peak to valley value is of 0.096 π. It corresponds to a pattern figure displacement of 0.4 μm, that is about 9% of the fitted lattice spacing $d = \pi/k_L$. From the measurement with repetition rate of 1 s^{-1}, the period over which there are fluctuations is about 5 seconds. On longer time of measure, which is associated with a lower resolution, the oscillations around zero seem to range on larger intervals. The inferior limit can be visualized in the measurement of five seconds where images are taken every 100 μs.

On hours timescale (6000 and 10000 seconds) RMS is around 0.03 π and the peak to valley value is approximately of $\pi/10$. It corresponds to a displacement of the lattice of 0.6 μm and is about 10% of the lattice spacing. Slow drifts over $\pi/10$ are evident on typical time scale of about 2000 s. Over the 6000 s long measurement, this drift follows the trend of the temperature monitored in the room, where there is a variation of 0.35°C in the "room" temperature and of 1.0°C in the "air" temperature (see subsection 4.1.4). In fact, the temperature is monitored by two probes, one sensible at air movements ("air"), and another, closed inside a box and protected by air flows, measures the actual temperature of the lab ("room").

For the measurement with 10000 s duration, variations are always evident on the same timescale of 2000 s even if temperature fluctuations are more contained. Thus, environmental parameters lead to cycles of stabilization of the air conditioning over

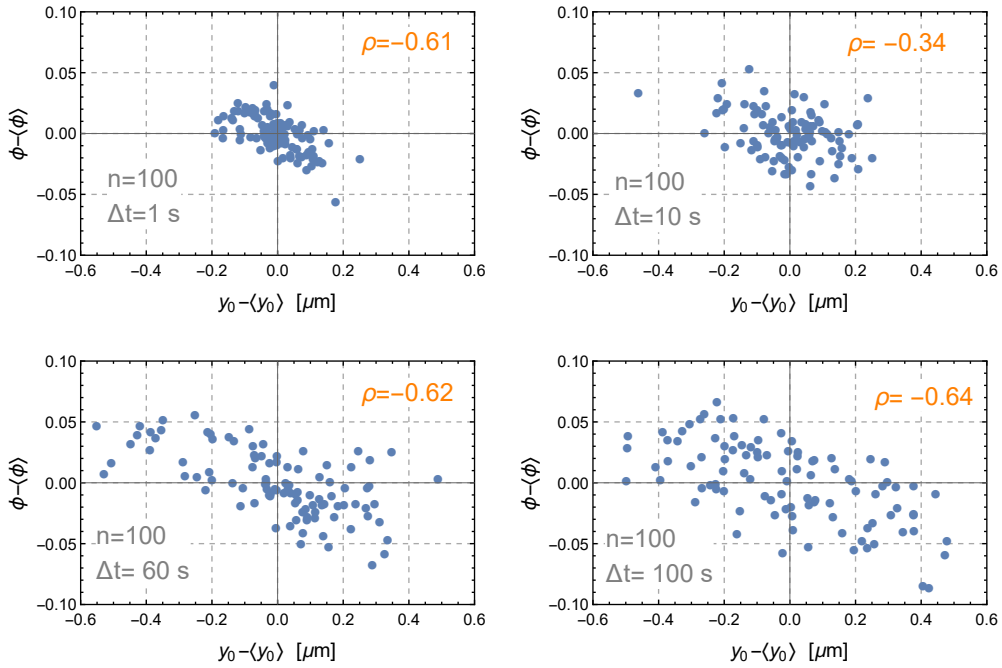

FIGURE 4.3: Correlation between fluctuations of the phase and of the beam pointing position in short and long-term measurement in the best achieved experimental condition. The measurements correspond to those showed in figure 4.2. On the top of each graphic, in orange, is shown the corresponding value of the correlator as defined in (4.2).

a timescale of about half an hour.

To test the stability of the lattice on timescale of a typical daytime, in normal conditions of work (with people inside the laboratory and the experiment running), I set the CCD Camera to take an image each five minutes of the interference pattern for more than eight hours as shown in Fig. 4.6. Data show fluctuations with a RMS of 0.12 π. This corresponds to an RMS in the lattice displacement of 0.5 μm. The peak to valley touches a value of $\pi/2$ that corresponds to a displacement of the pattern of 2.3 μm. It means that at least the lattice pattern can be moved of half lattice constant, but on average its fluctuations keep only to 10% of the lattice displacement in the entire daytime.

The optical table on which the experiment is mounted, is surrounded by a closed box. The temperature inside the box is less influenced by air drafts and by air conditioning cycles, with respect to the table were the lattice set-up has been tested. Thus, we expected that the fluctuations in the phase of the lattice can be reduced of, at least some percents. However, during an experimental run long typically few hours, will be always possible, if necessary, a manual active stabilization of the phase, optimizing the trajectory of both beams with respect to the optical axis.

The reproducibility of our experiment is guaranteed on hours timescale against fluctuations of 10% and for this reason we will able to load the majority of the atoms in the same pancake in every experimental cycle. On the other hand, on longest timescale where not-zero temperature variations, ranging on about 1°C, are present, the fluctuations can lead to a considerable displacement of the lattice of half lattice spacing with a possible consequent partial loss of atoms. From this, we learn constant temperature below is fundamental to prevent phase shifts of the optical lattice.

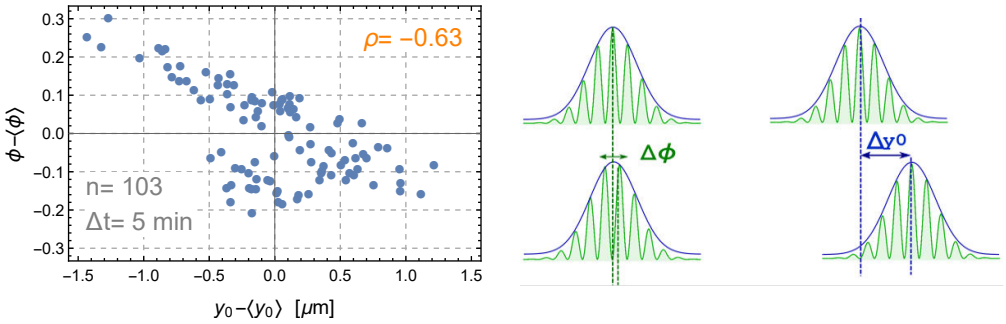

FIGURE 4.4: On the left, spread in plane of the correlation between phase and beam pointing position for longer-term measurement. On the right, sketch of phase and beam pointing position fluctuations.

4.1.3 Correlation between phase lattice and beam position

In the previous section it has been shown how the lattice pattern can displaces spatially in time. A further reason of displacement of the lattice pattern are fluctuations in the beam position, that take into account variations in the pointing of the laser that affect the pattern on the whole. The beam position values are extracted from the center of the Gaussian function that fits the intensity distribution of the lattice pattern.

Fluctuations of the beam pointing position with respect to its mean value over entire runs of measurements over minutes have an RMS value that range in $(0.009 \div 0.120)$ μm and a peak to valley value around $(0.4 \div 0.7)$ μm. Over a timescale of a couple of hours, RMS is of about 0.250 μm touching peaks of 1 μm, and for longer times, in particular in the eight hours measurement this value increases, touching 0.531 μm in the RMS value up to 2.6 μm in the peak to valley value.

A sizable correlation is evident comparing the extracted values for the phase with the respective extracted values of the pointing position of the beam as shown in Fig. 4.3. This means that phase shift of the lattice is higher the more displacement of pointing of the beam displaces itself from its mean value. This correlation between the phase and the beam position quantifies this feature and it is given by

$$\rho = \frac{\sum_{i=1}^{n}(\phi_i - \langle\phi\rangle)(y_{0\,i} - \langle y_0\rangle)}{\sqrt{\sum_{i=1}^{n}(\phi_i - \langle\phi\rangle)}\sqrt{\sum_{i=1}^{n}(y_{0\,i} - \langle y_0\rangle)}} \in [-1, 1]. \tag{4.2}$$

If $\rho = 0$ the two quantities are independent each other, whereas if $\rho = \pm 1$ they are fully correlated. The value of the correlators is around $|\rho| = 0.6$ for all measurements except one (that 1000 s long). Fig.4.3 shows distinctly how the points in the phase-pointing space spread increasing the observation time, including larger couples of values. This effect is at most evident in the eight hours measurement as is shown in Fig. 4.4.

The presence of the strong correlations between this two parameters suggests the existence of a common reason of drift. It can be understood taking into account two parameters, i.e. temperature and mechanical vibrations. On long time measurements, it can be clearly noticed from the measurements, as those shown in the following section 4.1.4 (see figure 4.6), that the phase and the temperature have the same trends. The position of the beam shows the same feature. Thus, the phase lattice and the beam position show correlation because both of them are sensible to changes in temperature. On the other hand, it is also evident that the correlation

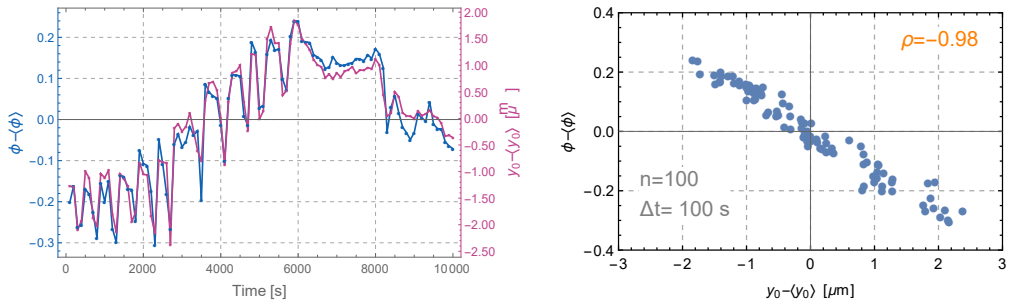

FIGURE 4.5: Consequences of perturbation effects on phase and beam pointing stability in a measurement taken in not optimal environmental condition. Impulses of air conditoning cycle induce fast fluctuations over periods of 500 s that destroy the phase stability (see also figure 4.7).

increases with the size of perturbation that affects the beams. For examples, measurement runs taken without floated table and without cover, exhibit, for the same time intervals, much correlation with respect to those shown here. This can explain also why in short time measurements, where temperature effects are not relevant, the correlation is the same as for long ones.

A significative proof of how perturbation effects can increase the correlation between these two quantities is shown in figure 4.5 where ρ touches a value of even about -1. This graphic shows the results of the fitted parameters for a run measurement taken in not optimal environmental conditions where impulses of air drafts destroy the phase stability of the lattice.

4.1.4 Temperature influence on long-term phase stability

As previous mentioned, long timescale measurements are affected by changes in temperature. To confirm this effect is helpful to compare the trend of values extracted by the fit parameters respect to the variations of temperature during the measurements timescale.

The data of temperature are registered on the on-line database Lens Temperature Advanced Observer (TAO) that collects information about each room of the institute. The sensibility and the resolution of this tool allows only a qualitative correlation between the temperature trend and the extracted parameters during the runs. In particular, the rate of the measurements is about one point over two seconds with a sensibility of about 0.05 °C. For this reason, considering that the changes in temperature are however small, at most on about 1.00°C, this analysis is relevant only for measurements lasting hours.

I have yet mentioned in Subsection 4.1.2 that variations of the lattice phase value along hours timescale can be influenced by temperature changes. However, the most striking prove of the correlation between phase shift and temperature is given by the measurement over an entire typical daytime as shown in Fig. 4.6. In this measurement are observed fluctuations of the phase with an RMS of 0.12 π during a RMS fluctuation in temperature of 0.13 °C, for the room, and 0.22 °C, for the air. At the same time, the RMS value for the beam pointing position is of about 0.53 μm. In spite of this, are evident slow drift in the phase value of some hours that seems to follow the trend of the temperature. This is confirmed by both temperature measurements. Peak to valley variation has a value of $\pi/2$ in correspondence to a maximum deviation of 1.20 °C in the air and in 0.60° in the room temperature.

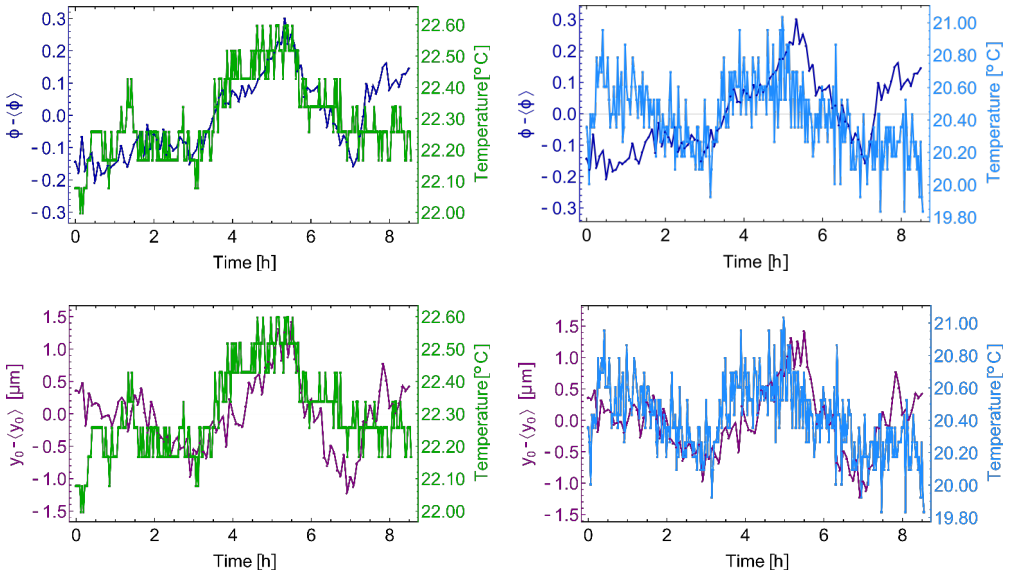

FIGURE 4.6: Comparison between the of the phase (up) and of the pointing beam position (down) with "room" (green) and "air" (light blue) temperature on a measurements of about eight hours long.

Looking now at the fitted values of the beam position, they also follow exactly the temperature trend over a deviation of 2.6 μm. The correlation with temperature for both phase and beam position, can explain the graphic in Fig. 4.4. Indeed, temperature variations could induce elongations and compressions in the mounts of the optical elements leading to a tilt of the beams with respect to the optical axis. This can changes their projection on the focal plane where is placed the CCD, and it can leads to both, phase shift and displacement of beam position. Unlike this, occasionally, the temperature and phase trends depart reciprocally and can be thought that there are other effects that affect the phase on hours measurements.

As explained in the subsection 4.1.1, the intensity of the laser that propagates in the optical fiber is sensible only at changes in temperature. Relative deviations of the laser intensity can be a good indication of the temperature variations. In Fig. 4.7, the relative intensity of the beam is compared to the phase variation of the lattice. During these measurements air flows was present. They show that the phase variations oscillate over a period of about 500 s following exactly the intensity beam variations. From this could be reasonable suppose that these oscillations are due to suddenly changes in air temperature over a period of about 500 s. This effect, is added to a slow drift over about $\pi/2$ in 8000 s, destroys the phase stability of the lattice. Indeed, the peak to valley variation reaches a value of $\pi/2$ that corresponds to a displacement of the pattern of 2.6 μm. It means that at least the lattice pattern can displace itself of half lattice constant; on average its fluctuations keep only to 10% of the lattice displacement. Thus, in order to maximize the temperature stabilization preventing this sudden variations, we have decided to put the entire lattice set-up in closed boxed.

Eventually, Fig. 4.8 shows the relative fluctuations in the lattice spacing and in the potential radius. These quantities can be extracted from the Eq. (4.1) too. The relative fluctuations in the lattice spacing are of the order of one on ten-thousand. Fluctuations in the potential radii are of some percent. This quantity can affect the frequency of the trap. Thus, these fluctuations are not a limitant factor during subsequent runs of measurements.

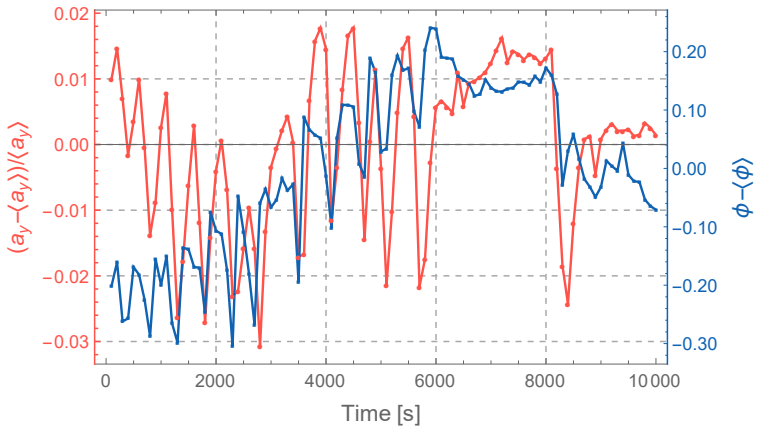

FIGURE 4.7: Measurement taken in not optimal environmental condition. Phase fluctuations follow intensity impulses that are due to bounce in air conditioning.

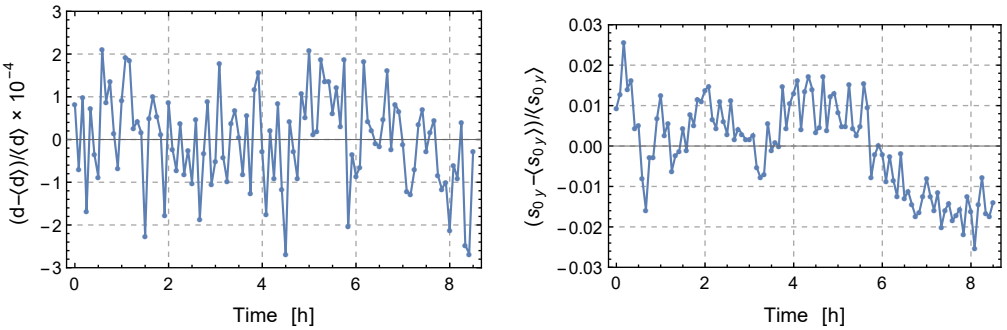

FIGURE 4.8: Relative deviation from the mean of the lattice spacing value (on the left) and relative deviation from the mean of the potential radii value (on the right) along an eight hours measurement.

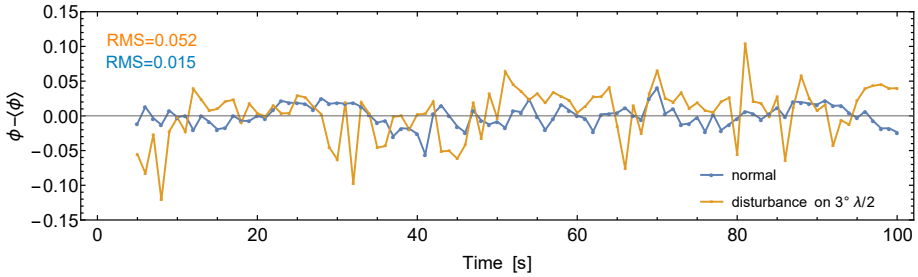

FIGURE 4.9: Example of a measurement of the short-term stability of the lattice phase in presence of disturbance on optical elements.

4.1.5 Mechanical vibrations effects on short-term phase stability

To test the reaction of the interference pattern to different mechanical vibrations I simulated air drafts with a paper, talked aloud, turned on music, knocked against the mounts of each optical element and leaned on the optical table. From these tests, I learned that the interference pattern is generally sensitive to such disturbances.

Because such kind of perturbations are relevant on short timescale, to quantify the influence of these effects on the lattice stability I monitored the interference pattern taking 100 images at one Hz rate. In presences of such disturbances the root mean square of the lattice fluctuations reaches at worst $\pi/2$, but generally the RMS fluctuations are well below $\pi/10$. In Fig. 4.9, is shown an example.

In particular, disturbances that affect the propagation of the beams after the splitting can influence the position of beams intersection and thus change the phase of the lattice. On the contrary, any optical element placed before the splitting of the beam, have a weak influence on the fringes since any disturbance influences both in the same way. These effect are whetever small, because the configuration of this set-up is optimized to minimize effects of relative shift between the path runned by the beams. In fact, in path after the splitting, both beams go through the same optical elements.

I confirmed that the element in transmission after the lateral prism displacement are quite insensitive to perturbation effects. In this framework has been decided to mount where was possible steal pillars instead brass ones, and to use stable mirror mounts. In fact, some optical elements mounts, as the cage system and the Polaris mounts, have been chosen in order to give more stability to the system.

Surely, the most relevant source of disturbance for the phase lattice are air flows. For this reason we have decided to put a cover over the set-up, placing it over pillars fixed on the optical table. In future, we will provide to close the set-up into a box. To overcame to these noise mechanisms we have decided also to use the floated table. Figure 4.10 shows the benefits coming from these choices.

4.2 Noise characterization

To study in detail the fluctuations on short timescales, it is important to characterize the noise spectrum of the lattice potential coming from both the intensity laser noise and from fluctuations of the fringe position[2]. Intensity and fringe position fluctuations of an optical potential are of interest because they both can cause heating

[2]As shown in section 4.1 on short timescale the distinction between phase and beam pointing fluctuations becomes very tiny, and therefore, for acquisition time of 1 s with a resolution of 5 μs, I refer to a mean effect that take in account both and determine fluctuations in the position of the fringes

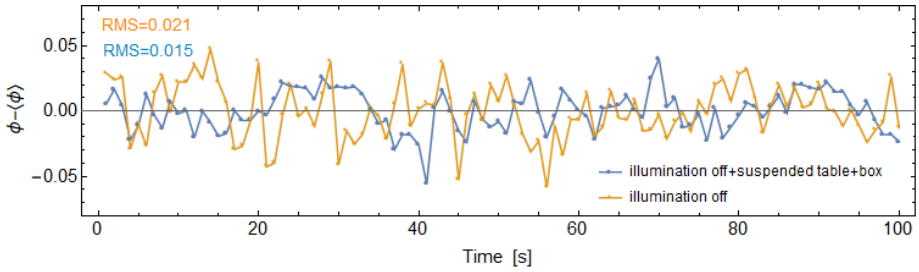

FIGURE 4.10: Comparison of the short-term phase stability with and without both cover over the lattice set-up and suspended table.

of the atoms, which will contribute also to increase the loss rate of the atoms from the trap. In general, the limitations caused by heating for optical lattices are much higher since heating scale strongly with the trap frequency. In order to qualitatively compare our results to possible heating sources, I will determine the heating rate in the optical trap derived from the measurements of the intensity power noise spectra and of the fringes position fluctuations.

Technical noise leads to fluctuations of the laser intensity $I(t)$ around a mean value I_0. The fractional fluctuations $\epsilon(t)$ is given by

$$\epsilon(t) = \frac{I(t) - I_0}{I_0}. \tag{4.3}$$

Since the fluctuations are stochastic by definition the mean value of $\epsilon(t)$ is zero. The quantity that gives information about the mean of the fractional fluctuations is the root mean square (RMS)

$$\Delta\epsilon = \lim_{T\to\infty} \sqrt{\frac{1}{T}\int_0^T \epsilon(t)^2 dt} \tag{4.4}$$

Using the Weiner-Khinchin theorem, the correlation function of the fractional fluctuations in the time domain, defined as

$$\langle \epsilon(t)\epsilon(t+\tau)\rangle = \lim_{T\to\infty} \frac{1}{T}\int_0^T \epsilon(t)\epsilon(t+\tau)dt \tag{4.5}$$

can be related to their power density spectrum

$$S_\epsilon(\nu) = \lim_{T\to\infty} \frac{|FT\{\epsilon(t)\}|^2}{T} \tag{4.6}$$

by the relation

$$FT\{\langle \epsilon(t)\epsilon(t+\tau)\rangle\} = \frac{S_\epsilon(\nu)}{2}. \tag{4.7}$$

From this relation and taking the spectrum for real-valued functions[3], the one-sided power spectrum of the fractional intensity noise is given as

$$S_\epsilon(\nu) = 4\int_0^\infty \cos(2\pi\nu\tau)\,\langle \epsilon(t)\epsilon(t+\tau)\rangle\, d\tau. \tag{4.8}$$

[3]The measurements cannot distinguish between positive and negative frequencies

From the one-side spectrum one can directly infer the so called relative-intensity noise (RIN) of the laser that is simple given by

$$RIN_\nu = 10 \cdot \log_{10} S_\epsilon(\nu) \tag{4.9}$$

measured in units [dB/Hz] that is a well used characterization of the laser noise provided in data sheets. The definition of one-sided power is also defined so that

$$\int_0^\infty S_\epsilon(\nu) d\nu = \langle \epsilon(t)^2 \rangle = \Delta\epsilon^2 \tag{4.10}$$

where $\Delta\epsilon$ is the RMS_I fractional intensity fluctuations. To specify the intensity noise of the laser in a specific range of frequencies from ν_1 to ν_2, can be calculated an RMS_I value from the power spectrum as

$$\Delta\epsilon|_{\nu_1,\nu_2} = \sqrt{\int_{\nu 1}^{\nu 2} S_\epsilon(\nu) d\nu}. \tag{4.11}$$

Such RMS_I value corresponds to the RMS_I fluctuations which one would measure with a detector with a bandwidth in a specific range, and can be used in order to compare the measured power spectrum with the specification of the laser. It is useful also to give the RMS_I of the fluctuations in a region of interest, as for example for the range around the predicted trapping frequency.

The same formalism can be developed for the fractional fluctuations of the center position of a single lattice fringe $x_0(t)$ around a value x_0, defined as

$$\epsilon_x(t) = x_0(t) - x_0 \tag{4.12}$$

where now $\epsilon_x(t)$ it is the fluctuation in the location of a fringe in [μm]. Here, one-sided power spectrum of the fringe position fluctuations $S_x(\nu)$ in units of [μm^2/Hz] is given by

$$S_x(\nu) = 4 \int_0^\infty \cos(2\pi\nu\tau) \langle \epsilon_x(t)\epsilon_x(t+\tau) \rangle d\tau \tag{4.13}$$

and the mean-square variation in the fringe center position is given by

$$\int_0^\infty S_x(\nu) d\nu = \langle \epsilon_x(t)^2 \rangle = \Delta\epsilon_x^2. \tag{4.14}$$

The fluctuations in a specific range of frequencies from ν_1 to ν_2, can be specified by an RMS_x value calculated from the noise spectrum 4.14 as

$$\Delta\epsilon_x|_{\nu_1,\nu_2} = \sqrt{\int_{\nu 1}^{\nu 2} S_x(\nu) d\nu} \tag{4.15}$$

and is useful also to give the RMS of the fringes position fluctuations in a region of interest, i.e. around the predicted trapping frequency.

4.2.1 Noise detection set-up

Experimentally, RMS fluctuations from both intensity and fringes position fluctuations are taken imprinting the laser light on a fast Si-photodiode (Thorlabs PDA 100A-EC) with switchable gain up to a bandwidth of 2.4 MHz (see the manual [39]),

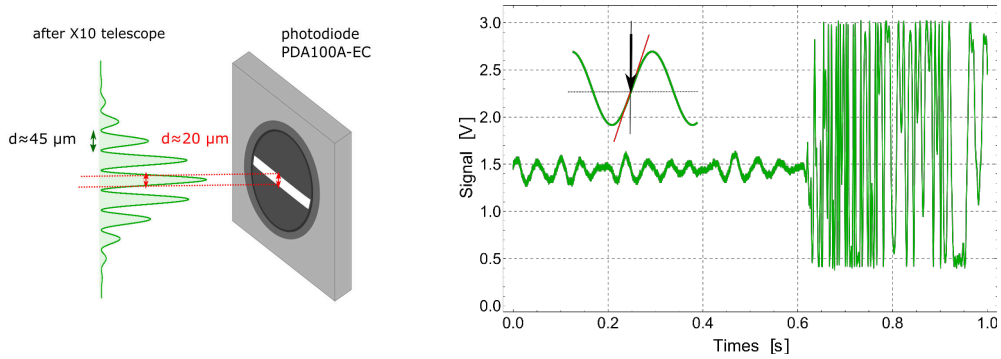

FIGURE 4.11: Set-up for the detection of the fringe position fluctuations. In order to have sufficient power on the photodiode, the laser noise signal is detected after the telescope that magnifies the interference pattern. To detect the signal from a single fringe is sufficient put a slit on the photodiode aperture of high smaller lattice spacing. On the right, the signal at the output of the photodiode aligned to detect the signal from the half of the central fringe is shown. Knocking on the table with a screwdriver allows to sample the full amplitude of the most intense fringe of the lattice.

placed after the X10 telescope that magnifies the spacing of the lattice. The photodiode used in our set-up has an active area of 100 mm^2 and a photo sensitivity of about 0.62 A/W at the peak wavelength of 960 nm. The signal is then read out using Rohde&Shwarz RTE 1104-Oscilloscope with a sample rate of up to 1 GHz (5 GSa/s). Thus, I performed two different kind of measurements, one to detect the intensity noise spectrum, and then another to register the noise arising from the fringe position fluctuations.

Intensity noise To record the intensity noise spectrum, I blocked one of the two beams and monitored the power of the laser with all the surface of the sensor. The intensity I of the laser, i.e. its power in unit of surface, is proportional to induced current i_l given by the responsivity of the photodiode operating in linear regime $\eta_1(\lambda)$ measured in [A/W]. The gain of the photodiode determine the bandwidth and the efficiency $\eta_2(BW)$, measured in [V/A] through which converting current in voltage V_l. The detected power on the resistor R of the oscilloscope is then $P = i_l^2 R = V_l^2/R$.Therefore the fractional laser intensity is translated in the measured fractional voltage fluctuation recorded by an oscilloscope. In order to obtain the one-side power spectrum, the y-t signals are recorded in AC and DC coupling with a sampling rate of $f_s = 200$ kSa/s and an acquisition time of $t_{max} = 1$ s. Using AC coupling it increased the dynamic range to observe fluctuations. The AC coupling signal corresponds to the fluctuations $\Delta I(t) = I(t) - I_0$, whereas the mean of the DC coupled signal corresponds to I_0 obtaining the fractional fluctuation $\epsilon(t)$ given in (4.3). Because we deal with a discrete time-sampling, one has to use the discrete Fourier transformation (DFFT). The step size of the DFFT is $\Delta f = t_{max}^{-1}$. To obtain the correct power spectrum I calculated it as:

$$S_\epsilon(\nu) = \frac{DFFT(V_{AC}) \cdot DFFT^*(V_{AC})}{t_{max} V_0^2} \tag{4.16}$$

where V_0 is the mean signal taken in DC coupling, and V_{AC}, the AC one. To get any meaningful results, one has to be sure to be not limited by other noise sources,such as dark currents in the photodiode and photon shot-noise. The minimum variation of light that can be detected is the energy of a single photon. Because the photon flux

varies with a poissonian distribution around a mean value and the detected power also fluctuates which leads to the so-called shot-noise and limits the detectable RIN to

$$RIN_{SNL} = 10 \cdot \log_{10}\left(\frac{h\nu\eta_1\eta_2}{t_{max}V_0}\right) \tag{4.17}$$

where ν is the laser frequency for $\lambda = 532$ nm, $\eta_1 = 0.35$ A/W is the responsivity of the photodiode at 532 nm, $\eta_2 = 4.75 \cdot 10^4$ V/A [39] is the gain of the photodiode at high impedance, $t_{max} = 1$ s.

Fringe position noise To take the noise spectrum given by fringe position fluctuations on the photodiode aperture, we used a slit of 20 μm, that is about half of the lattice spacing. In this way, was possible to detect the light coming from a small portion of the laser beam, i.e. a single fringe. This allows to register the fluctuations of the interference pattern as variations in the laser power, as shown in figure 4.11. . If the interference pattern fluctuates in the vertical direction during the measurement, the power detected by the photodiode fluctuates too. The fluctuations of the power of the laser can be related at the fringes position fluctuations in the following way. We aligned the photodiode with respect the direction of propagation of the beam in order to register the AC signal from the half maximum of the central fringe of the pattern (see figure 4.11). This allows a linear response in the detection of the signal. At this point, we define an adimensional stochastic variable for the voltage detected

$$\epsilon_v(t) = \frac{V(t) - V_0}{\Delta V}, \tag{4.18}$$

similar to that defined for intensity fluctuations in (4.3), but where $V(t) - V_0$ is the voltage read by the photodiode in AC coupling, whereas ΔV is the peak to valley of the signal coming from a single fringe taken in DC coupling. The power spectrum associated with this voltage fluctuations is given by

$$S_v(\nu) = 4\int_0^\infty \cos(2\pi\nu\tau)\,\langle\epsilon_v(t)\epsilon_v(t+\tau)\rangle\,d\tau. \tag{4.19}$$

that is related to the RMS fractional voltage fluctuations $\Delta\epsilon_v$ as

$$\int_0^\infty S_v(\nu)d\nu = \langle\epsilon_v(t)^2\rangle = \Delta\epsilon_v^2 \tag{4.20}$$

Thus the RMS position fluctuations can be related to the RMS fractional voltage fluctuations, i.e. to spectrum taken by the photodiode, by

$$\Delta\epsilon_x = \frac{d}{2}\sqrt{\int_0^\infty S_v(\nu)d\nu} \tag{4.21}$$

where d is the lattice spacing. In this way, we express the RMS_x in μm of the fringe position fluctuations proportional to the RMS_I of the intensity noise fluctuations, i.e. calculable from the power spectrum of the fractional fluctuations $S_v(\nu)$. Moreover, dividing $\Delta\epsilon_x$ by π is possible to translate position into phase fluctuations in π units. Given a sampling rate of $f_s = 200$ kSa/s and a acquisition time of $t_{max} = 1$ s, the step size of the DFFT is given by $\Delta f = t_{max}^{-1} = 1$ Hz. To obtain the correct power

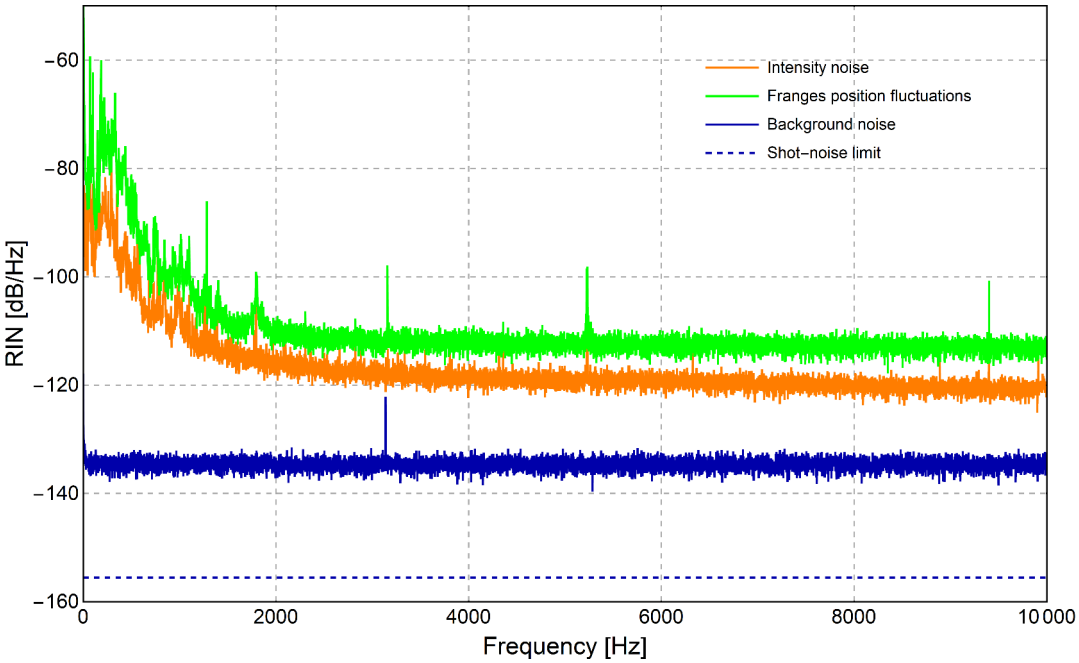

FIGURE 4.12: Comparison between relative noise intensity (RIN) measurements of the Verdi-V8 laser intensity noise (orange) and fringes position fluctuations (light green). The blue-dotted line shows the shot-noise limited RIN measurements and the blue data are the background noise from the photodiode (PDA100A-EC). Sampling rate is 200 kSa/s and the acquisition time is 1 s.

spectrum I calculated it as:

$$S_v(\nu) = \frac{DFFT(V_{hf\ AC}) \cdot DFFT^*(V_{hf\ AC})}{t_{max}\Delta V^2} \tag{4.22}$$

where ΔV is the mean signal taken in DC coupling, and $V_{hf\ AC}$, the AC one at the half high of the fringe.

Figure 4.12 shows the trend of intensity and of fringe position fluctuations, with respect the background noise of the photodiode and the shot-noise limit. Shot-noise limit calculated by (4.17) corresponds to a shot noise of -156 dB/Hz and a photodiode background noise on the same order which is sufficiently low to measure the expected laser noise. From this comparison seems that the fringes position noise at low frequencies is given by intensity noise. At high frequency peaks at 16.0 kHz, 18.4 kHz , 32.0 kHz, 36.7 kHz, 56.0 kHz, 89.0 kHz are present in both spectra, and most likely they are due to technical intensity laser noise. The RMS_I of $\Delta\epsilon = 9 \cdot 10^{-4}$ over a range of 10 kHz and however within the manufacturer's specification that estimates an $\text{RMS}_I < 0.02$. On the other hand RMS_x is of $\Delta\epsilon_x = 7.3 \cdot 10^{-3}$ μm. To lower the intensity noise at low frequencies, and in particular below 10 kHz, in order to avoid heating effects at trapping frequencies, we have stabilized the signal with a PID controller.

4.2.2 Stabilization of the laser intensity

Laser stabilization means actively controlling the emitted intensity. In order to stabilize the laser intensity, the actual value of the intensity has to be measured and from this an error signal is obtained, corresponding to the difference between the actual

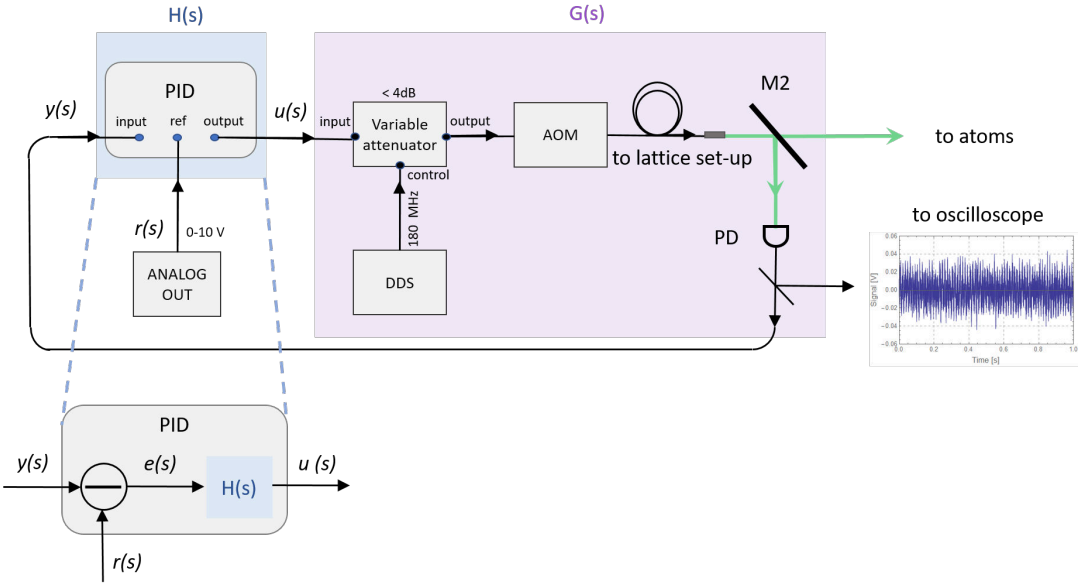

FIGURE 4.13: Feedback loop implemented to stabilize laser intensity noise in the lattice set-up.

and desired value. If the error signal is zero the measured value coincides with the desired one.The larger the slope of this change, the smaller are the deviations can be detected. To stabilize it, the so-called servo control loop is used, whose mathematical modeling is based on the idea of the feedback. It means that the output of a system is influenced by the monitored output of the system itself. The electronic devices that implement this mechanism are called PID controller and consist of a proportional part (P), an integral part (I) and a differential part (D). Stabilization using feedback leads to corrections that are stable and durable so that temperature drifts, hysteresis and non linear effects do not effect the output of the system.

The set-up for the stabilization of the laser intensity in the lattice set-up is shown in figure 4.13. The signal from the lattice set-up is collected by the losses of the mirror M2 and detected by a photodiode PDA 36A-EC [40] with switchable gain set on 40 dB corresponding to a bandwidth of 150 kHz. This is the portion of the signal taken to stabilize the laser. A portion of signal goes to the Rodhe&Swarhz oscilloscope and another part, $y(s)$ goes to the input of the PID controller. With the oscilloscope, set in DC mode at 1 MΩ (high impedence), we registered the values obtained, setting different values in the input of the AOM. From this collection of couple of voltages I get the calibration curve between the value that I have to set in the PID controller and the value read on oscilloscope and taken by the photodiode.

The reference signal $r(s)$ is given by the analog output that ranges in 10 V, and the error signal $e(s) = r(s) - y(s)$ elaborated by the PID controller produces at the output a signal $u(s) = H(s)e(s)$, where $H(s)$ is the transfer function of the controller. It goes to a variable attenuator that reduce the amplification below 4 dB and receive in input a frequency of about 180 MHz from the digital generator of frequency (DDS) in order to produce an RF signal in input for the AOM. The system on the whole between the output and the input of the PID control have a transfer function $G(s)$, that response with a new signal $y(s) = G(s)u(s)$. To monitor the signal $u(s)$ produced by the PID control a part of the output signal goes to the spectrum analyzer.The limit in lowering of the noise is imposed by the so called "servo bump" that is found at the frequency at which the noise of the stabilized signal is increased. It comes from

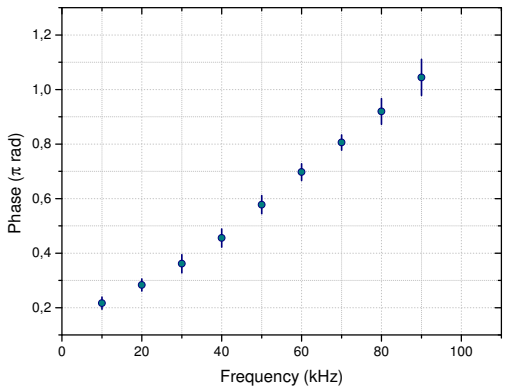

FIGURE 4.14: Phase of the loop implemented to stabilize laser intensity noise in the lattice set-up.

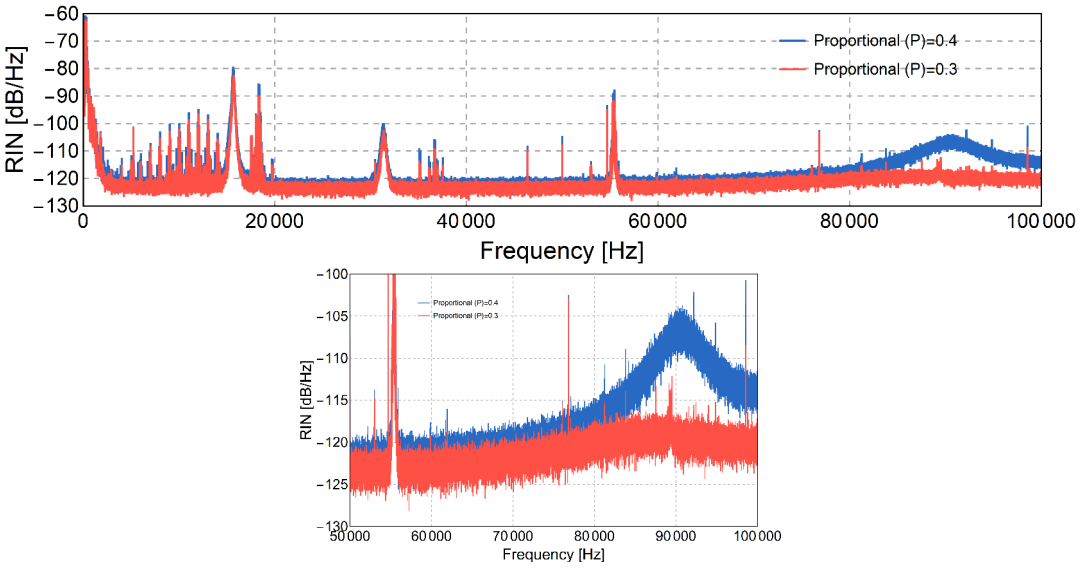

FIGURE 4.15: Noise spectrum with the power stabilization switched on. The blue and red spectra show fringes position fluctuations noise for to different chosen gain of the P value on the PID control.

the fact that disturbances at frequencies close to the bandwidth of the system need longer time until they are damped causing the noise spectrum to be increased in the range where the phase is close to 180° (see figure 4.14) and the gain is the larger one. On the other hand, on a oscilloscope, it can be seen as the frequency at which the system starts to oscillate if the gain is increased. Fig. 4.15 shows that the servo loop reduces the noise below 60 kHz. Our procedure has been developed to reduce intensity noise at very low frequencies, especially below 10 kHz in order to avoid heating effects at trapping frequencies. In order to do this, we had to increase the proportional (P) during the optimization of the controller increasing the noise of the signal after the servo bump and reducing at the same time the noise at low frequencies. Fig. 4.15 show fringes position fluctuations for different chosen gain of the P value on the PID control.

In figure 4.17 is shown the comparison between the intensity noise of Verdi-V8

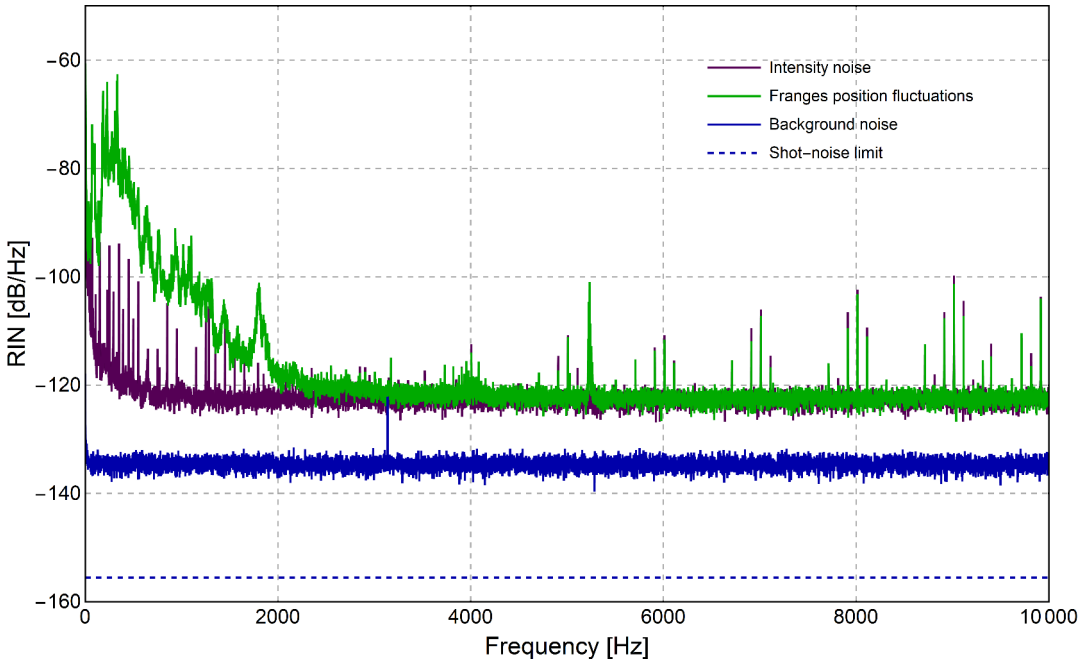

FIGURE 4.16: Comparison after the power stabilization between relative noise intensity (RIN) measurements of the Verdi-V8 laser intensity noise (purple)(PDA36A-EC) and fringes position fluctuations (dark green)(PDA100A-EC). The blue-dotted line shows the shot-noise limited RIN measurements and the blue data are the background noise from the photodiode (PDA100A-EC). Sampling rate is 200 kSa/s and the acquisition time is 1 s.

	free running		**power stabilized**	
frequency range:	$(0 \div 10)$ kHz	$(0 \div 100)$ kHz	$(0 \div 10)$ kHz	$(0 \div 100)$ kHz
$\Delta\epsilon$	$7 \cdot 10^{-4}$	$9 \cdot 10^{-4}$	$2 \cdot 10^{-4}$	$6 \cdot 10^{-4}$
$\Delta\epsilon_x$ [μm]	$7.3 \cdot 10^{-3}$	$7.7 \cdot 10^{-3}$	$7.2 \cdot 10^{-3}$	$7.4 \cdot 10^{-3}$

TABLE 4.3: Summary of RMS fluctuations.

laser with and without stabilization. The gain of the PID controller has been optimized in order to reduce the noise at low and acoustic frequencies below 10 kHz. Below 2 kHz the noise is reduced at most of about 35 dB/Hz. Instead of this, spikes are present due to internal resonances of the measurement circuit. The half width of maximum of these peaks is less than 10 Hz. The stabilization does not affect in a relevant way the noise spectrum of fringes position fluctuations The noise reduction is only few dB/Hz as shown in figure 4.18. Figure 4.16 shows the comparison between signals after the intensity stabilization of the laser. It is interesting to notice how below 2 kHz the phase noise is still about 35 dB/Hz above the level of the intensity noise, whereas for higher frequencies the two spectra coincide. This is a proof that fringes noise below 2 kHz is not a consequence of the laser intensity noise, as seemed before the stabilization (see figure 4.12) but rather that the cause of fluctuations is the same. The integrated power spectrum for the intensity noise yields an RMS of $\Delta\epsilon = 6 \cdot 10^{-4}$ over a range of 10 kHz. For fluctuations in the fringes position the RMS is of $\Delta\epsilon_x = 7.2 \cdot 10^{-3}$ μm. In table 4.3 are summarized the RMS fluctuations for both spectra before and after the stabilization.

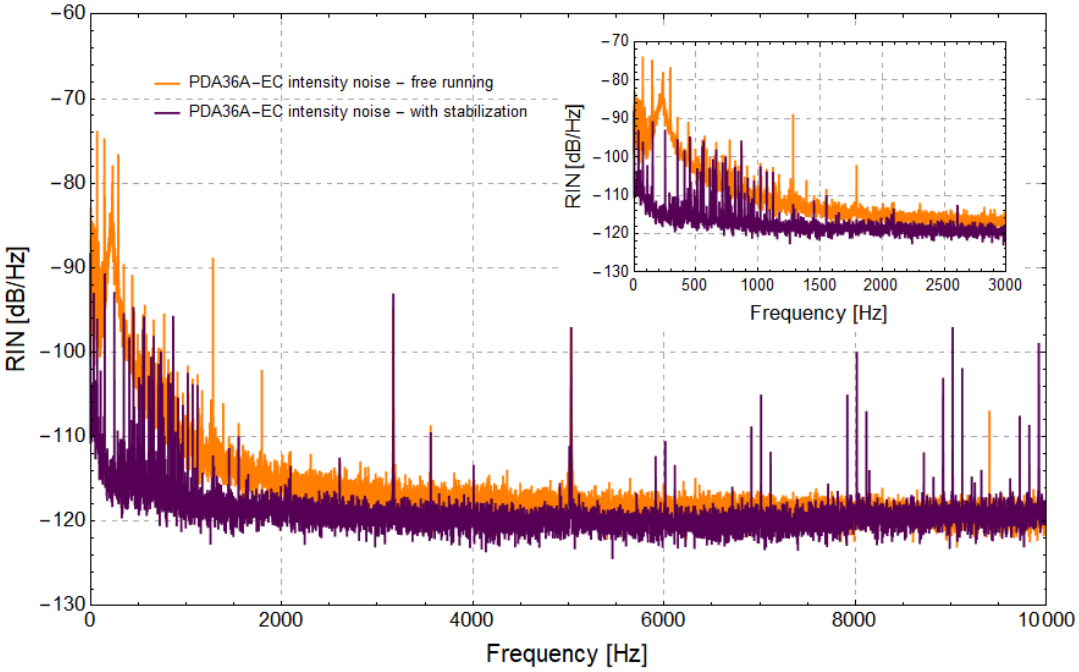

FIGURE 4.17: Relative noise intensity (RIN) measurements of the Verdi-V8 laser intensity noise with power stabilization turned on (purple)/off (orange). Sampling rate is 200 kSa/s and the acquisition time is 1 s.

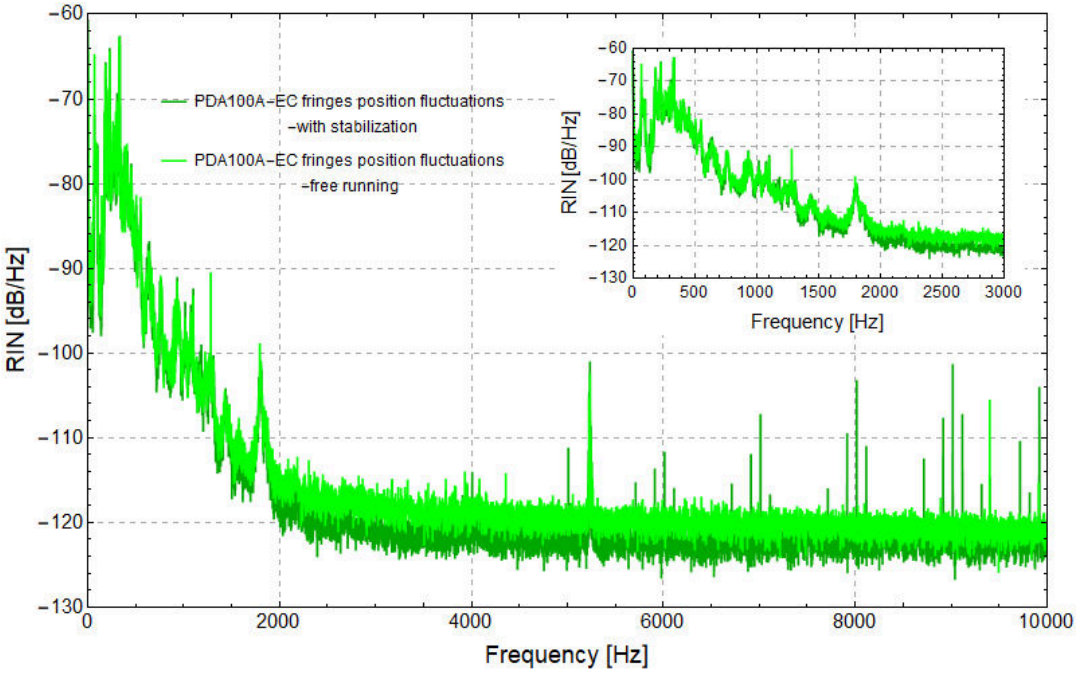

FIGURE 4.18: Relative noise intensity (RIN) measurements of fringes position fluctuations with power stabilization turned on (dark green)/off (light green). Frequency rate is of 1 Hz and record length is of 200000 samples.

4.3 Laser-noise-induced heating

Laser intensity fluctuations and fringes position fluctuations may play an important role in determining the minimum heating rates that can be obtained in both red and blue detuned optical traps. In the framework of a simple one dimensional harmonic-oscillator model it's possible to give an explicit expressions for the expected heating rates. I will follow the theory derived in the articles by *Savard et al.* [41] and [42].

4.3.1 Heating rate caused by intensity noise

To determine the heating rate due to laser intensity fluctuations, we take the model Hamiltonian for a trapped atom of mass M to be

$$H = \frac{p^2}{2M} + \frac{1}{2}M\omega_{tr}^2[1+\epsilon(t)]x^2 \tag{4.23}$$

where $\omega_{tr}^2 = k_0/M$ is the mean-square trap oscillation frequency, k_0 is proportional to the time averaged laser intensity I_0 and $\epsilon(t)$ are fractional fluctuations of the laser intensity as defined in 4.3 and are exhibited in the spring constant of the oscillator. Here we consider the harmonic oscillator modelizes the trapping frequencies given by the single focalized gaussian beam. The heating rate is determined using first order time-dependent perturbation theory to calculate the average transition rates between quantum states of the trap. The time-dependent perturbation is given by

$$H'(t) = \frac{1}{2}\epsilon(t)M\omega_x^2 x^2 \tag{4.24}$$

and because the perturbation is quadratic in its spatial coordinate, the perturbation does not change the parity of the states and thus in a harmonic oscillator this transition can only occur in steps of $\pm 2\omega_x$. We assume that the averaging time T is quite small compared to the timescale over which the atom population varies, but large with respect to the correlation time of the fluctuations[41]. The transition rate $R_{n\pm 2\leftarrow n}$ can then be calculated as [41]

$$R_{n\pm 2\leftarrow n} = \frac{\pi\omega_x^2}{16}S_\epsilon(2\omega_x)(n+1\pm 1)(n\pm 1) \tag{4.25}$$

with $S_\epsilon(\omega) = S_\epsilon(\nu)/(2\pi)$ where $S_\epsilon(\nu)$ is the one-sided power spectrum defined in Eq. (4.19) and $\omega = 2\pi\nu$ is the angular frequency. Since the overlap of adjacent states with same parity increases for larger trap levels n, the transition rates are not symmetric and the average energy increases over time. This leads to the fact that the heating depends on temperature. In fact, for larger T higher trap levels are occupied and hence the transition rates increases with a consequent heating of the sample. Then, from the transition rate in Eq. (4.25) it is easy to calculate the time derivative of the mean energy $\langle E\rangle = \langle E(t)\rangle = \sum_n P(n,t)(n+1/2)\hbar\omega_{tr}$, assuming that initially the trapped atoms occupy the state $|n\rangle$ with probability $P(n,t)$ at time t [41] that is just

$$\langle \dot{E}\rangle = \Gamma_\epsilon \langle E\rangle \tag{4.26}$$

where the rate constant is given by

$$\Gamma_e = \frac{1}{T_e} = \pi^2\nu_{tr}^2 S_e(2\nu_{tr}) \tag{4.27}$$

where ν_{tr} is the trap frequency in Hertz and T_e is the energy e-folding time in seconds (time to increase $\langle E \rangle$ by a factor e). Eq. (4.26) shows that the average energy increases exponentially.

Figure 4.19 shows how the energy e-folding time T_e calculated from the (4.27) varies with the choice of the trap frequency for a laser with the power shown in figure 4.17. The trap frequencies around 8.0 kHz and near 9.1 kHz show a a deep resonance, and, therefore, they should be avoid These points correspond to prominent peaks in the power spectrum at the double of their frequency. At higher frequencies, also near 18 kHz, 28 kHz and 44 kHz, time T_e goes abruptly to zero. Just below 8 kHz, $T_e \approx 1000s$ and it increases exponentially for lower frequencies until reaching 20000 s for 2 kHz. In the vertical direction of the optical lattice we will have typical trap frequency of about $(5 \div 10)$ kHz. In the plane we will have trapping frequencies on the order of 10 Hz. However, putting these numbers[4] into the energy e-folding time T_e

$$T_e = \frac{1}{\pi^2 \nu_{tr}^2 S_e(2\nu_{tr})} \tag{4.28}$$

derived from equation (4.27), we obtain $T_{e\ lattice} \approx 1000$ s and a $T_{e\ plane} \approx 10^4$ s. Thus, for these frequency, laser noise will not limit one in conducting experiments in the optical lattice: heating times are much longer with respect to the typical timescale of a single experimental run. Moreover, should be sufficent tuning the power of the laser in order to decrease a little the frequencies trap to avoid the resonance at 8 kHz. On the other hand, the spikes, are likely due to spurious noise sources entering in the measurement circuit that will be changed and shortened when the set-up will be put on the experiment. Eventually, the heating coming from the e-folding time energy, leads to quite long atoms storage times in the quasi 2D harmonic-trap respect to the typical experimental timescale.

4.3.2 Heating rate caused by fringe position fluctuations

In a optical lattice, fringe position fluctuations must be stringently controlled. In this case, the effective Hamiltonian is given by

$$H = \frac{p^2}{2M} + \frac{1}{2} M \omega_{tr}^2 [x - \epsilon_x(t)]^2 \tag{4.29}$$

where this harmonic oscillator modelizes the trapping frequencies given by the potential corresponding to a single fringe of the interference pattern and $\epsilon_x(t)$ is the fluctuation in the position of the trap center.Analogous to the methods used to obtain (4.27), calculations based on (4.29), yield to an energy-doubling time T_x that can be defined as the time needed to increase the energy by the average energy at $t = 0$, $\langle \dot{E} \rangle / \langle E(0) \rangle = 1/T_x$. Then using $\langle E(0) \rangle = M\omega_{tr}^2 \langle x^2 \rangle$ where $\langle x^2 \rangle$ is the mean-square position of an atom in a trap at t=0[5], one obtains:

$$\langle \dot{E} \rangle / \langle E(0) \rangle = \frac{1}{T_x} = \pi^2 \nu_{tr}^2 \frac{S_x(\nu_{tr})}{\langle x^2 \rangle} \tag{4.30}$$

where here $S_x(\nu)$ is the one-sided power spectrum of the position fluctuations of the trap center as defined in (4.13) and measured as explained in section 4.2.1. The mean

[4] As typical lattice trap frequency we choose 7 kHz.

[5] To notice that $\langle x^2 \rangle$ defined here and $\langle \epsilon_x(t)^2 \rangle$ defined in (4.14) are to different quantities. The first refers to the spread of the atomic wave function in the harmonic potential, whereas the second one to the fluctuations of the trap.

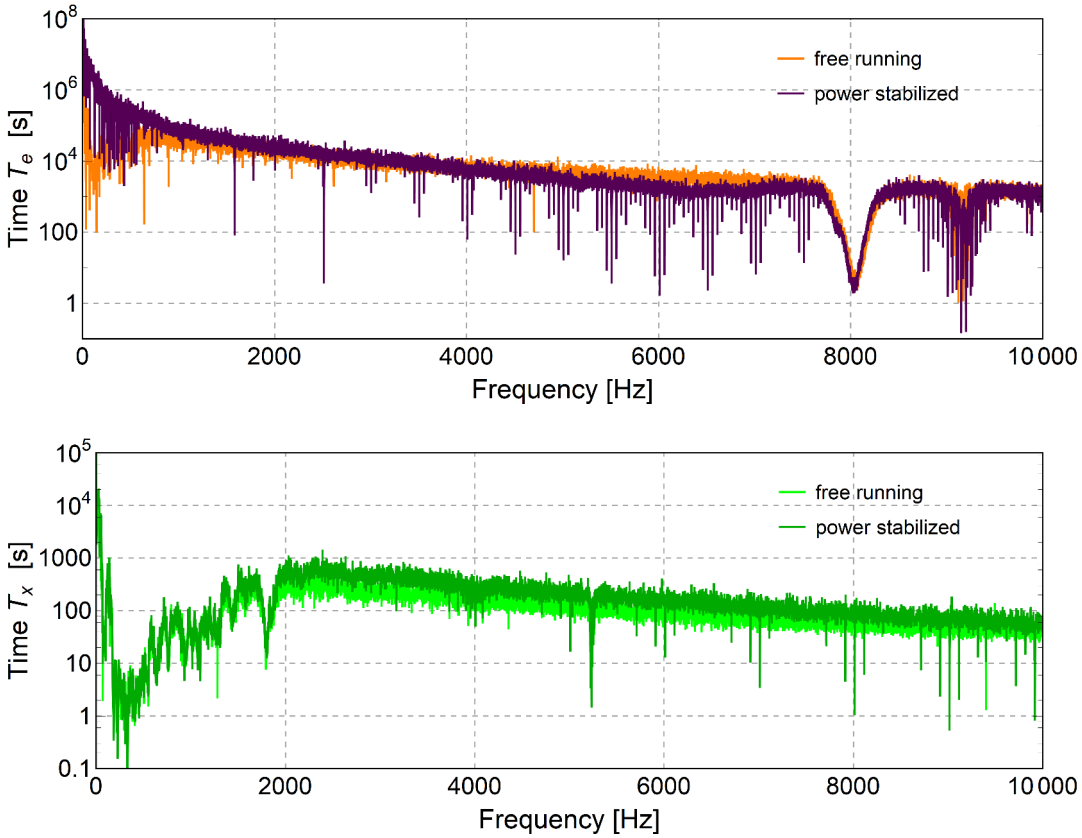

FIGURE 4.19: Up: the calculated energy e-folding time T_e plotted as a function of the trap frequency $\nu_{tr} = \omega_{tr}/2\pi$ with (purple) and without (orange) power stabilization; down: the calculated mean energy doubling time T_x plotted versus trap frequency ν_{tr}, with (dark green) and without (light green) power stabilization. For both set of measurements Verdi-V8 was running at 1 W.

energy e-folding time T_e:	(1300 ± 300) s
energy doubling time T_x:	(125 ± 40) s

TABLE 4.4: Summary of the typical heating-time for a frequency of 7.5 kHz after power stabilization.

square position $\langle x^2 \rangle$ is the harmonic oscillator ground-state length $l = \sqrt{\hbar/(m\omega_{tr})}$ in a harmonic potential of frequency ω_{tr}. The energy-doubling time T_x is thus calculated as

$$T_x = \frac{\hbar}{2M\pi^2\nu_{tr}^3 S_x(\nu_{tr})}. \tag{4.31}$$

Figure 4.19 shows that the energy doubling time, between frequencies of 6 kHz and 10 kHz, ranges from about 300 s to 50 s. These timescale are eventually longer with respect to the timescale of a single experimental run, i.e. about 10 ms. In particular, for the trapping frequency expected, the heating rate corresponds to region in the noise spectrum quite flat and T_x is about 100 s. Thus, in the end, our lattice potential will provides a confinement with reasonably low heating rate at the trapping frequency of 7.5 kHz. In table 4.4 I summarize the typical heating time after the stabilization caused by intensity noise and fringes position fluctuations for the predicted trapping frequency.

Conclusions

My thesis work has been focused on the realization of a one-dimensional large-spacing optical lattice for confining ^{6}Li atoms in single or multilayer quasi-2D geometries. I have designed and built the optical set-up for creating the lattice potential, choosing the optical elements and the parameters for trapping the atoms. At the same time, I have carried out numerical simulations to characterize the loading of cold fermionic 3D samples into the quasi-2D geometry at finite temperatures, assuming an adiabatic procedure. From these simulations, I have obtained the temperature of the cloud in the quasi-2D potential after the adiabatic loading. I have also extracted the required confining frequency and atom number to achieve the quasi-2D condition with a Fermi gas at finite temperature.

Guided by the results of these simulations, I have chosen the desired lattice trapping parameters. I have subsequently modelled the optical lattice potential in order to calculate the beam parameters required to obtain the desired trapping frequencies and depth of the lattice. At this point, I could design an optical system to produce the calculated values of the beam waists and the required crossing angle between the two interfering beams. Besides determining the suitable lenses for shaping the beam intensity profiles, the most important aspect of the optical setup has been the choice of the scheme to produce two interfering beams with optimal relative phase stability. For this goal, a lateral displacement prism has been implemented to separate the two lattice beams, while keeping their optical path as identical as possible.

The realized optical lattice has a spacing of $d \simeq 4.3$ μm. The measured beam waists lead to an axial trapping frequency of $\omega_x = 2\pi\,(7.5 \pm 0.2)$ kHz and radial ones of $\omega_y = i2\pi\,(8.8 \pm 0.7)$ Hz and $\omega_z = i2\pi\,(15.5 \pm 0.3)$ Hz at a beam power of 1 W. Such axial frequency satisfies the quasi-2D confinement condition for ^{6}Li atoms, numerically calculated for typical experimental parameters. The maximum number of atoms is close to $2.5 \cdot 10^5$, for an initial temperature of $T/T_F = 0.1$ before the loading. The lattice spacing is very close to the design value. Tuning the intensity of the beams to lower power, this lattice will allow to explore different tunnelling regimes, with tunneling rates varying from 10 Hz to 10^{-3} Hz. This feature will permit to study the coupling between different atomic layers. Moreover, if desired, such spacing is suitable for the direct loading of the atoms in a single minimum of the optical lattice.

I have also investigated the dynamical stability of the lattice interference pattern, revealing a RMS phase fluctuation of 0.015π and 0.12π over 100 seconds and 8 hours of continuous measurement in a typical laboratory environment, respectively. These correspond to 1.5% and 12% of the lattice spacing, respectively. On the other hand, the characterization of the lattice noise spectrum has allowed to evaluate the typical laser noise-induced heating rates. For the expected trapping frequency of 7.5 kHz, we estimate an intensity-induced energy e-folding time $T_e = (1300 \pm 300)$ s and a fringe position-induced energy doubling time $T_x = (125 \pm 40)$ s. These values are much larger than typical experimental time scales, and are therefore satisfactory.

In the near future, we plan to integrate this lattice set-up into the main experimental apparatus. This will allow to address the study of the intriguing phenomenology of strongly-correlated atomic Fermi gases in two dimensions.

Bibliography

[1] Nobelprize.org, *"The Nobel Prize in Physics 2016 - Scientific background: Topological phase transitions and topological phases of matter"*, 2016. [Online]. Available: http://www.nobelprize.org/nobel_prizes/physics/laureates/2016/advanced.html.

[2] P. Anderson, *Intralayer tunneling mechanism for high–tc superconductivity: Comparison with c-axis infrared experiments included in: Pw anderson, the theory of superconductivity in the high–tc cuprates*, 1997.

[3] D. L. Goodstein, *States of Matter*. Courier Corporation, 1985.

[4] C. J. Pethick and H. Smith, *Bose-Einstein condensation in dilute gases*. Cambridge university press, 2002.

[5] M. Köhl, "Thermometry of fermionic atoms in an optical lattice", *Physical Review A*, vol. 73, no. 3, p. 031 601, 2006.

[6] K. Huang, "Statistical mechanics, 2nd", *Edition (New York: John Wiley & Sons)*, 1987.

[7] P Dyke, E. Kuhnle, S Whitlock, H Hu, M Mark, S Hoinka, M Lingham, P Hannaford, and C. Vale, "Crossover from 2d to 3d in a weakly interacting fermi gas", *Physical review letters*, vol. 106, no. 10, p. 105 304, 2011.

[8] D. S. Petrov, C Salomon, G. Shlyapnikov, and L. Cugliandolo, "The few-atom problem", *Proceedings of the Les Houches Summer Schools, Session*, vol. 94, p. 109, 2010.

[9] W. Ketterle and M. W. Zwierlein, "Making, probing and understanding ultracold fermi gases", *arXiv preprint arXiv:0801.2500*, 2008.

[10] S. K. Adhikari, "Quantum scattering in two dimensions", *American Journal of Physics*, vol. 54, no. 4, pp. 362–367, 1986.

[11] P. Bloom, "Two-dimensional fermi gas", *Physical Review B*, vol. 12, no. 1, p. 125, 1975.

[12] M. Randeria, "Ultracold fermi gases: Pre-pairing for condensation", *Nature Physics*, vol. 6, pp. 561–562, 2010.

[13] D. Guéry-Odelin and C. Cohen-Tannoudji, *Advances in Atomic Physics*. World Scientific, 2011.

[14] J. Bardeen, L. N. Cooper, and J. R. Schrieffer, "Microscopic theory of superconductivity", *Physical Review*, vol. 106, no. 1, p. 162, 1957.

[15] S. Giorgini, L. P. Pitaevskii, and S. Stringari, "Theory of ultracold atomic fermi gases", *Reviews of Modern Physics*, vol. 80, no. 4, p. 1215, 2008.

[16] A Burchianti, G Valtolina, J. Seman, E Pace, M De Pas, M Inguscio, M Zaccanti, and G Roati, "Efficient all-optical production of large li 6 quantum gases using d 1 gray-molasses cooling", *Physical Review A*, vol. 90, no. 4, p. 043 408, 2014.

[17] G. Valtolina, "Development of an experimental apparatus for the production and study of ultracold atomic gases of fermionic lithium", Tesi di laurea magistrale, Università di Milano - Bicocca, 2012.

[18] A. Morales, "High resolution imaging and production of thin barriers for ultracold 6li fermi gases", Tesi di laurea magistrale, Università di Roma "La Sapienza", 2013.

[19] A. Amico, "Measurement of the equation of state of superfluid fermi gases of 6li atoms", Tesi di laurea magistrale, Università degli Studi di Firenze, 2015.

[20] G. Valtolina, "Superfluid and spin dynamics of strongly interacting atomic fermi ga", Tesi di dottorato, Scuola Normale Superiore di Pisa, 2016.

[21] R. Grimm, M. Weidemüller, and Y. B. Ovchinnikov, "Optical dipole traps for neutral atoms", *Advances in atomic, molecular, and optical physics*, vol. 42, pp. 95–170, 2000.

[22] J Dalibard and C. Cohen-Tannoudji, "Dressed-atom approach to atomic motion in laser light: The dipole force revisited", *JOSA B*, vol. 2, no. 11, pp. 1707–1720, 1985.

[23] C. Cohen-Tannoudji and D. Guéry-Odelin, *Advances in atomic physics: an overview*. World Scientific, 2011.

[24] H. Kogelnik and T. Li, "Laser beams and resonators", *Proceedings of the IEEE*, vol. 54, no. 10, pp. 1312–1329, 1966.

[25] B. E. Saleh and M. C. Teich, *Fundamentals of photonics*. Wiley, 2007.

[26] M.Neidig, "A realization of a two-dimensional fermi gas in a standing wave trap", Master thesis, University of Heidelberg, 2013.

[27] M.G.Ries, "A two-dimensional Fermi gas in the BEC-BCS Crossover", PhD thesis, University of Heidelberg, 2015.

[28] I. Bloch, J. Dalibard, and W. Zwerger, "Many-body physics with ultracold gases", *Reviews of modern physics*, vol. 80, no. 3, p. 885, 2008.

[29] M. Born and E. Wolf, *Principles of optics: electromagnetic theory of propagation, interference and diffraction of light*. Elsevier, 2013.

[30] T. Li, H Kelkar, D Medellin, and M. Raizen, "Real-time control of the periodicity of a standing wave: An optical accordion", *Optics express*, vol. 16, no. 8, pp. 5465–5470, 2008.

[31] M. Lohse, "Large-spacing optical lattices for many body physics with degenerate quantum gases", Diploma thesis, Max-Plank-Institute for Optics, Munich, 2012.

[32] J. Ville, T. Bienaimé, R Saint-Jalm, L. Corman, M. Aidelsburger, L. Chomaz, K. Kleinlein, D Perconte, S. Nascimbène, J. Dalibard, *et al.*, "Loading and compression of a single two-dimensional bose gas in an optical accordion", *Physical Review A*, vol. 95, no. 1, p. 013 632, 2017.

[33] J.E.Bohn, "Towards an ultracold three component Fermi gas in a two-dimensional optical lattice", Diploma thesis, University of Heidelberg, 2012.

[34] D. Mitra, P. Brown, P. Schauss, S. Kondov, and W. Bakr, "Phase-separation and pair condensation in a spin-imbalanced 2d fermi gas", *Phys. Rev. Lett.*, vol. 117, p. 093 601, 2016.

[35] J. C. Wyant and K. Creath, "Basic wavefront aberration theory for optical metrology", *Applied optics and optical engineering*, vol. 11, no. part 2, pp. 28–39, 1992.

[36] Thorlabs, Ed., *WFS series-Operation manual*, 2012.

[37] Thorlabs, Ed., *CCD and CMOS cameras-DCx Camera Functional Description and SDK Manual*, 2016.

[38] R. M. Azzam and N. M. Bashara, *Ellipsometry and polarized light*. North-Holland. sole distributors for the USA and Canada, Elsevier Science Publishing Co., Inc., 1987.

[39] Thorlabs, Ed., *PDA100A(-EC) Si Amplifier Fixed Detector - User Guide*, 2016.

[40] Thorlabs, Ed., *PDA36A(-EC) Si Amplifier Fixed Detector - User Guide*, 2016.

[41] T. Savard, K. O'hara, and J. Thomas, "Laser-noise-induced heating in far-off resonance optical traps", *Physical Review A*, vol. 56, no. 2, R1095, 1997.

[42] M. Gehm, K. O'hara, T. Savard, and J. Thomas, "Dynamics of noise-induced heating in atom traps", *Physical Review A*, vol. 58, no. 5, p. 3914, 1998.

Ringraziamenti

L'ultima pagina è rivolta a tutti coloro che, con entusiasmo ed impegno, mi hanno permesso di svolgere e completare questo lavoro di tesi.

Vorrei iniziare ringraziando sinceramente il mio relatore Dr. Francesco Scazza, per avermi guidata in questo percorso con dedizione e creatività. Lo ringrazio per gli interessanti spunti di riflessione che sempre mi ha proposto nello sviluppo del lavoro di tesi, per la fiducia ed il sostegno che non mi ha mai fatto mancare. E' stato bello approcciarmi alla fisica sperimentale avendo l'opportunità di sviluppare lente dopo specchio e giorno dopo giorno, un intero set-up, con il suo costante supporto. E' stata una ricca esperienza di crescita sia come fisico che come persona.

Ringrazio il Dr. Giacomo Roati, per avermi offerto e seguito in questo stimolante lavoro di tesi, nonchè per avermi calorosamente accolta nel suo team. La sua esuberanza e il suo ottimismo sono stati motivo di incoraggiamento in questi mesi di intenso lavoro. Lo ringrazio per avermi offerto la preziosa opportunità di seguire corsi e conferenze che mi hanno permesso, sia di allargare le mie prospettive, che di avere il privilegio di incontrare importanti fisici e scienziati, nonchè premi Nobel.

Devo un ringraziamento particolare al Dr. Pedro Tavares e alla precisione dei suoi metodi, per essermi stato di supporto nella parte più tecnica del lavoro e per avermi pazientemente atteso in tarda serata, durante l'estate, affichè potessi concludere le mie misure.

Un grazie di cuore, va anche al Dr. Matteo Zaccanti per la sua gentilezza ed allegria, nonché alla sua profondità di scienziato, per avermi introdotta al suo progetto di ricerca.

Vorrei ringraziare, inoltre, il Prof. Giovanni Modugno per il sostegno e i consigli che mi ha dato in questi anni.

Ringrazio Andrea per la spensierata compagnia dentro e fuori il laboratorio, sessioni fotografiche incluse. Una menzione speciale va inoltre a Giulia, spalla e compagna di avventure e disavventure in questi pazzi mesi di consegne e scadenze.

Guardando al di fuori dal mondo accademico, devo però riconoscere che non sarei probabilmente arrivata fin qui se non fosse stato per la mia meravigliosa famiglia. Vi ringrazio per il sostegno incondizionato e la costante fiducia in me riposta in ogni piccola e grande sfida della vita. Grazie in particolare per avermi fatta crescere in un incredibile ricchezza di stimoli e di idee che mi hanno resa una persona libera di scegliere e con una testa piena di sogni. Questo lavoro è dedicato a voi.

In questi anni di studio e formazione mi è stato compagno Lorenzo, con cui ho condiviso successi e sconfitte. Insieme ci siamo divertiti ad elaborare le più strane teorie chimico-fisiche ed a prendere un pò dell'uno dall'altra. Grazie per essermi stato vicino sempre e per tutto il resto che già sai.

Infine un ringraziamento speciale lo voglio rivolgere a tutte quelle persone che in maniera spesso inaspettata sono state fonte di preziosi consigli, frutto il più delle volte del disimpegno, ed hanno così fatto da cornice ai ricordi che ho collezionato in questi mesi.